UNIVERSITY OF CALIFORNIA SAN DIEGO

Advancing Focused Ion Beam Characterization for Next Generation Lithium-Ion Batteries

A dissertation submitted in partial satisfaction of the requirements for the degree Doctor of Philosophy

in

NanoEngineering

by

Jungwoo Zema Lee

Committee in charge:

Professor Ying Shirley Meng, Chair
Professor David P. Fenning
Professor Eric E. Fullerton
Professor Olivia A. Graeve
Professor Ping Liu

2018

The Dissertation of Jungwoo Zema Lee is approved, and it is acceptable in quality and form for publication on microfilm and electronically:

Chair

University of California San Diego

2018

DEDICATION

To my given and chosen family

TABLE OF CONTENTS

LIST OF ABBREVIATIONS

ABF	annular bright field
CE	coulombic efficiency
CV	cyclic voltammetry
DFT	density functional theory
DEC	diethyl carbonate
DMC	dimethyl carbonate
DME	dimethoxyethane
EC	ethylene carbonate
EDS	energy dispersive spectroscopy
EELS	electron energy loss spectroscopy
EIS	electrochemical impedance spectroscopy
FIB	focused ion beam
GIXRD	grazing angle X-ray diffraction
HAADF	high angle annular dark field
LCO	lithium cobalt oxide
LiB	lithium-ion battery
LiFSI	lithium bis(fluorosulfonyl)imide
LiTFSI	lithium bis(trifluoromethane)sulfonimide
LiPON	lithium phosphorous oxynitride
LLTO	lithium lanthanum titanate
LLZO	lithium lanthanum zirconate
LNMO	lithium nickel manganese oxide
PLD	pulsed laser deposition
PVDF	polyvinylidene fluoride

SAED	selected area electron diffraction
SEI	solid electrolyte interphase
SEM	scanning electron microscopy
SSE	solid-state electrolyte
STEM	scanning transmission electron microscopy
TEM	transmission electron microscopy
UHV	ultra high vacuum
XRD	X-ray diffraction
XPS	X-ray photoelectron spectroscopy

LIST OF FIGURES

LIST OF TABLES

ACKNOWLEDGEMENTS

This work would not have been possible without the generous support of countless individuals. I would like to thank my advisor Professor Y. Shirley Meng who gave me the opportunity and freedom to pursue many academic interests. As her advisee I was challenged to expand the breadth and depth of my scientific knowledge and scientific rigor. I would also like to express my gratitude to my committee members: Professor Ping Liu, Professor David P. Fenning, Professor Eric E. Fullerton, and Professor Olivia Graeve for their time and guidance.

I am eternally grateful to my thin film partner, Thomas A. Wynn, who has stood by me through countless late night experiments and scientific discussions to help me grow as a researcher. I also would like to thank my collaborators and co-authors, Ziying Wang, Huolin Xin, Dhamodaran Santhanagopalan, Shilpa N. Raja, Frank P. McGrogan, Tushar Swamy, Yet-Min Chiang, Krystyn J. Van Vliet, Judith Alvarado, Xuefeng Wang, Marshall A. Shroeder, and Kang Xu for their contributions and expertise throughout these projects. I would also like to acknowledge the entire Laboratory for Energy Storage and Conversion group for providing a work environment filled with collaboration, communication, and insight.

I would like to thank my family, Sol J. Lee, Ho S. Lee, and Jung H. Lee for their support and inspiration to live a life filled with intention, gratitude, and authenticity. They instilled in me a love of learning and curiosity that motivates me every day.

I acknowledge financial support from the Eugene Cota-Robles Fellowship Program of the University of California San Diego. This work was supported by the U.S. Department of Energy, Office of Basic Energy Sciences, under Award Number DE-SC0002357. This work was performed in part at the San Diego Nanotechnology Infrastructure (SDNI) of UCSD, a member

of the National Nanotechnology Coordinated Infrastructure, which is supported by the National Science Foundation (Grant ECCS-1542148). This work was performed in part at the UC Irvine Materials Research Institute (IMRI) using instrumentation funded in part by the National Science Foundation Major Research Instrumentation Program under grant no. CHE-1338173.

Chapter 4, in full, is a reprint of the material "Amorphous Lithium Lanthanum Titanate For Solid-State Microbatteries" as it appears in the Journal of the Electrochemical Society, J.Z. Lee, Z. Wang, H.L. Xin, T.A. Wynn, and Y.S Meng, 2017, 164, A6268. The dissertation author was the primary investigator and first author of this paper. All the experiments and writing were done by the author expect for the X-ray diffraction and STEM-EELS data collection.

Chapter 5, in full, is currently being prepared for submission for publication "LiPON Solid Electrolyte Stiffens Upon Exposure to Ambient Humidity," S.N Raja, J.Z. Lee, T.A. Wynn, F.P. McGrogan, T. Swamy, Y.M. Chiang, Y.S. Meng, and K. Van Vliet. The dissertation author was the co-primary investigator and co-first author of this paper. All of the experimental parts were performed, analyzed, and written by the author except for the film growth and mechanical testing.

Chapter 6, in full, is a reprint of the material, "Focused Ion Beam Fabrication of LiPON-based Solid-state Lithium-ion Nanobatteries for *In Situ* Testing" as it appears in the Journal of Visualized Experiments, J.Z. Lee, T.A. Wynn, Y.S. Meng, and D. Santhanagopalan, 2018, 133, e56259. The dissertation author was the co-primary investigator and co-first author of this paper. All of the experimental parts were developed and performed by the author. Thomas A. Wynn and the author analyzed and wrote the results.

Chapter 7, in full, is currently being prepared for submission for publication "Cryogenic Focused Ion Beam Characterization of Lithium Metal Anodes for Li-Ion Batteries," J.Z. Lee,

T.A. Wynn, J. M.A. Schroeder, J. Alvarado, X. Wang, K. Xu, and Y.S. Meng. The dissertation author was the primary investigator and first author of this paper. All the experiments and writing were done by the author expect for the electrochemical sample preparation and transmission electron microscopy data collection.

VITA

2010 Bachelor of Arts, Physics and American Studies, Wellesley College

2016 Master of Science, NanoEngineering, University of California San Diego

2018 Doctor of Philosophy, NanoEngineering, University of California San Diego

PUBLICATIONS

(* authors contributed equally to the work)

1. **J.Z. Lee**, T.A. Wynn, M.A. Schroeder, J. Alvarado, X. Wang, K. Xu, and Y.S. Meng, "Cryogenic focused ion beam for characterization of alkaline metal anodes," (in preparation).

2. J. Alvarado, M.A Schroeder, T.P Pollard, X. Wang, **J.Z. Lee**, M. Zhang, T.A. Wynn, M. Ding, O. Borodin, Y.S. Meng, and K. Xu, "High concentrated electrolytes for Li metal anodes," (in preparation).

3. S.N Raja*, **J.Z. Lee***, T.A. Wynn, F.P. McGrogan, T. Swamy, Y.M. Chiang, Y.S. Meng, and K. Van Vliet, "Compliant mechanical behavior of LiPON solid electrolyte using airfree nanoindentation," (in preparation).

4. T.A. Wynn, **J.Z. Lee**, A. Banerjee, and Y.S. Meng, "*In situ* and operando probing of solid-solid interfaces in electrochemical devices," *MRS Bulletin* (under review).

5. T.A. Wynn, C. Fang, M. Zhang, H.D. Liu, D.M. Davies, X. Wang, D. Lau, **J.Z. Lee**, K-Z. Fung, and Y.S.Meng, "Mitigating oxygen release in anionic-redox-active cathode materials by cationic substitution through rational design" *Journal of Materials Chemistry A* (under review).

6. E. Wu, C.S. Kompella, Z. Zhu, A. Banerjee, **J.Z. Lee**, S.C. Lee, I.H. Chu, H. Nguyen, S.P Ong, and Y.S. Meng, "New Insights into the interphase between the Na metal anode and sulfide solid-state electrolytes: a joint experimental and computational study" *ACS Applied Materials and Interfaces* **10**, 12 (2018).

7. **J.Z. Lee***, T.A. Wynn*, Y.S. Meng, and D. Santhanagopalan, "Focused ion beam fabrication of LiPON-based solid-state lithium-ion nanobatteries for in situ testing" *Journal of Visualized Experiments* (133), e56259, doi:10.3791/56259 (2018).

8. **J.Z. Lee**, Z. Wang, H.L. Xin, T.A. Wynn, and Y.S Meng, "Amorphous Lithium Lanthanum Titanate For Solid-State Microbatteries,"*Journal of the Electrochemical* Society **164**, 1 (2017).

9. J.W. Shin, J.M. You, **J.Z. Lee**, R. Kumar, Y.S. Meng, and J. Wang, "Catalytic deposition of ZnO on Bi2O3 towards prolonged Zn-based aqueous battery," *Physical Chemistry Chemical Physics* **18** (2016).

10. Z. Wang, **J.Z. Lee**, H. Xin, L. Han, D. Guy-Bouyssou, E. Bouyssou, N. Grillon, M. Proust, Y.S. Meng, "Effects of interfacial phenomena on long term cycling of all-solid-state batteries," *Journal of Power Sources* **324** (2016).

11. C.D. Bailie, M. Greyson Christoforo, J.P. Mailoa, A.R. Bowring, E.L. Unger, W.H. Nguyen, J. Burschka, N. Pellet, **J.Z. Lee**, M. Woodhouse, R. Noufi, M. Grätzel, T. Buonassisi, A. Salleo, M.D. McGehee, "Semi-transparent perovskite solar cells for tandems with silicon and CIGS," *Energy and Environmental Science* **8** (2015).

12. C.R. Cox, **J.Z. Lee**, D.G. Nocera, and T. Buonassisi, "10% solar-to-fuel conversion with non-precious materials," *Proceedings of the National Academy of Sciences* **111**, 39 (2014).

13. **J.Z. Lee**, L. Michaelson, K. Munoz, T. Tyson, A. Gallegos, J.T. Jullivan, and T. Buonassisi, "In-Situ photoluminescence imaging for passivation-layer etching process control for photovoltaics," *Applied Physics Letters* **105**, 043901 (2014).

ABSTRACT OF THE DISSERTATION

Advancing Focused Ion Beam Characterization for
Next Generation Lithium-Ion Batteries

by

Jungwoo Zema Lee

Doctor of Philosophy in NanoEngineering

University of California San Diego, 2018

Professor Ying Shirley Meng, Chair

Next generation lithium-ion batteries will take on a wide variety of roles to meet the increased requirements from growth in consumer electronics, electric vehicles, and utility storage for integrating intermittent renewable (solar and wind) power sources. The cost per watt-hour of commercial batteries have shown incremental improvement due to improved manufacturing design, though drastic increases in energy and power density are needed to satisfy projected demand. Solid-state electrolytes (SSE) are explored due to their potential to improve energy and power density through enabling alkali metal anodes, while mitigating safety and temperature

stability concerns associated with conventional liquid electrolyte lithium-ion batteries. However, there are still significant scientific and engineering hurdles before the full potential of SSEs can be realized: primarily performance degradation from chemical and mechanical interfacial instability.

We enable the use of solid-state thin film battery materials and devices as a model system for fundamental studies of bulk and interface properties because of their well-defined geometry and controlled chemical composition, eliminating any effects from polymeric binder or conductive agents. In this thesis, we explore the structural, mechanical, and electrochemical properties of thin film electrolytes amorphous lithium lanthanum titanate (a-LLTO) and lithium phosphorous oxynitride (LiPON) along with the fabrication of thin film batteries with various electrode chemistries. Using these devices we develop focused ion beam (FIB) as a technique to fabricate electrochemically active nanobatteries that enables *in situ* analysis in a FIB or transmission electron microscope (TEM) to couple local structural, morphological, and chemical phenomena. Further, one key advantage of SSEs is the potential to use a lithium metal anode. However, characterization of Li and Li/electrolyte interfaces is limited due to its intrinsic high chemical reactivity, low thermal stability, and low atomic number, making it prone to contamination and melting. Therefore, we demonstrate the ability of cryogenic focused ion beam (cryo-FIB) to process and characterize electrochemically deposited Li and Li metal based solid-state thin film devices.

Chapter 1. Introduction

1.1 Motivation

There is increased demand for advances in energy storage technologies as there is increased need for both high energy and high power energy storage for a wide range of both established and emerging market applications. Lithium-ion batteries, since their first commercialization by Sony Corporation in 1991, have established themselves as the dominant mobile energy storage technology with the highest year over year growth (**Fig. 1.1.a**). In the Unites States, sales of lithium-ion batteries were $902 million in 2017 with the majority of sales in consumer electronics (**Fig. 1.1.b**).[1] Worldwide demand of lithium-ion batteries is expected to grow by 10.8% annually to 2022,[2] driven mostly by increased demand in electrified transportation vehicles, and stationary utility storage for integrating intermittent renewable (solar and wind) power sources.

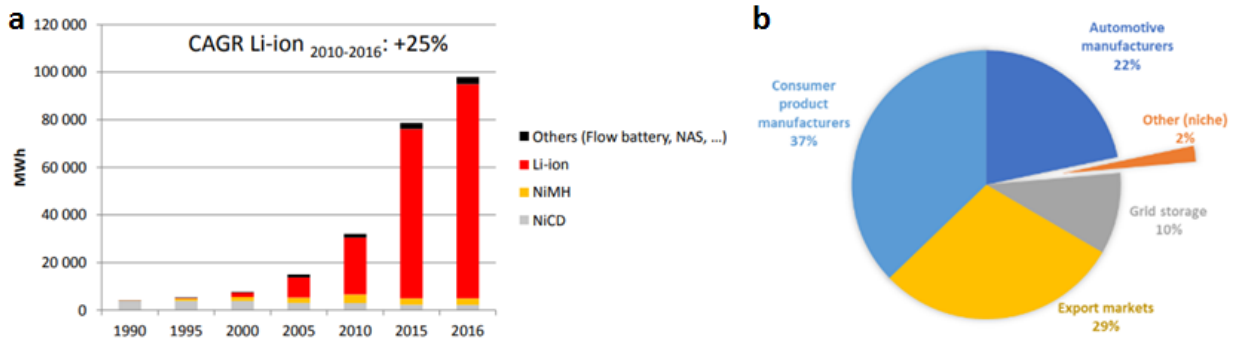

Figure 1.1. (a) Growth in battery market segments over time.[3] (b) Lithium-ion battery market in United States of America in 2017.[1]

Although the lithium-ion battery market is mature, there are still significant research and development efforts to develop batteries with longer run time, higher voltage, reduced cost,

faster recharge time, increased number of recharges, and increased safety. While the future of commercial devices will likely depend on a synergistic effort between new materials development along with engineering optimization at the electrode, cell, and pack level, there are still key fundamental scientific questions as to the structural, chemical, mechanical, and electrochemical phenomena that govern battery performance. Research thrusts have invested in improving current materials and designs, developing next generation chemistries, analyzing degradation mechanisms, and developing new characterization tools to elucidate the complex and dynamic changes during battery operation.

Lithium-ion battery materials and architectures are inherently complex, therefore we enable the use of solid-state thin film battery materials and devices as a model system for fundamental studies of bulk and interface properties because of their well-defined geometry and controlled chemical composition, eliminating any effects from polymeric binder or conductive agents. In this thesis, we explore the synthesis of new solid-state electrolyte (SSE) thin-film materials such as amorphous lithium lanthanum titanate (a-LLTO), and fabricate thin film batteries with various electrode chemistries. Using these devices we develop a technique to fabricate electrochemically active nanobatteries with a focused ion beam (FIB) to enable *in situ* analysis in a FIB or transmission electron microscope (TEM). Further, one key advantage of a solid-state battery architecture is the ability to use a lithium metal anode. However, characterization of Li is limited because of its intrinsic high chemical reactivity, low thermal stability, and low atomic number making it prone to contamination and melting. Therefore, we demonstrate the ability of cryogenic focused ion beam (cryo-FIB) to process and characterize electrochemically deposited Li and Li metal based solid-state thin film devices.

1.2 Lithium-Ion Batteries

Batteries are systems for electrochemical energy storage and conversion, where electrical energy is generated from stored chemical energy through oxidation-reduction (redox) reactions at the electrodes. If these reactions are reversible, where electrical energy can be converted to chemical energy, then the battery system is rechargeable. Various battery chemistries have been developed including lead-acid, Zn-Ag, Ni-Cd, and Ni-metal hydride, but lithium-ion batteries have emerged as a dominant technology due to its high gravimetric and volumetric energy density. This is because to lithium is the lightest metallic element (6.94 g/mol) and has one of the lowest reduction potentials (- 3.04V vs standard hydrogen electrode).

The active components of current commercial state of the art lithium-ion batteries consist of a layered metal oxide cathode (positive electrode), layered graphite anode (negative electrode), and ethylene carbonate electrolyte with $LiPF_6$ as salt (**Fig. 1.2**). During charging, externally applied electrical energy drives Li ions from a lower chemical energy state in the cathode to the anode. Then during battery discharge, or operation, the anode is oxidized and positively charged Li ions are transferred to the cathode resulting in electron release to the external circuit in order to maintain charge balance. Ideally, this reaction does not result in any deleterious structural or chemical changes. Additional important components to ensure battery operation are a polyolefin resins separator to prevent physical and electrical contact between the anode and cathode, metallic current collectors to supply charge from each electrode to the external circuit, and proper mechanical casings to contain the closed cell and facilitate integration into larger packs and devices to connect to an external circuit during use. If flow of either electrons of ions is impeded in any way the battery will no longer function.

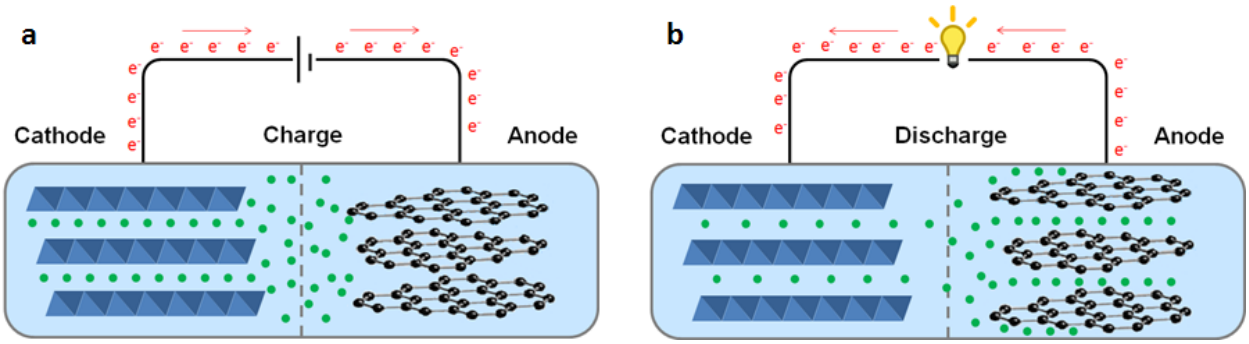

Figure 1.2. Schematic of lithium-ion battery during (a) charging and (b) discharging.

The battery operating voltage and specific capacity is determined by the resulting electrochemical reaction between the cathode and anode. The cell voltage arises from the difference in chemical potential and electrical potential between the two electrodes, expressed by the Gibbs free energy

$$\Delta G_r = -z_i F V + \mu_i \tag{1.1}$$

where ΔG_r is the Gibbs free energy change per mol of reaction (J/mol), z_i is the charge number of the ionic species, F is the Faraday constant (96,500 C/mol), V is the electric potential between the electrodes, and μ_i is the chemical potential. Under equilibrium conditions (i.e. open circuit) the voltage of the electrochemical cell is determined by the Nernst equation

$$V_{eq} = -\frac{\mu_{Li}^{cathode} - \mu_{Li}^{anode}}{z_{Li} F} \tag{1.2}$$

where the chemical potential of the electrode is determined by the specific reaction mechanism (e.g intercalation, alloy, etc.). The Gibbs free energy of an individual electrode is a function of the Li concentration n_{Li}^x and net charge $q^x = n_{Li}^x - n_e^x$, so for a given cathode the chemical potential is

$$\mu_{Li}^{cathode} = \left(\frac{\partial G}{\partial n_{Li}^{cathode}}\right)_{T,P,N} = \eta_{Li}^{cathode} - \eta_{e}^{cathode} \tag{1.3}$$

where n_i^x is the electrochemical potential of species i in phase x. Thus it follows that during charge and discharge, the voltage

$$V_{eq} = -\frac{\left(\mu_{Li}^{cathode} - \mu_{Li}^{anode}\right) - \eta_{Li}^{cathode} - \eta_{e}^{anode}}{z_{Li}F} \tag{1.4}$$

deviates from the thermodynamic theoretical values depending on state of charge. The lower Li chemical potential in the cathode relative to the anode creates the driving force that moves Li from the anode to cathode during discharge. The resulting shape of the voltage curve is further influenced by the free energy curve due to phase stability and transitions (**Fig. 1.3.a**). Sloping portions of the voltage curve correspond to single-phase solid solutions, while plateaus indicate two-phase regions.

Further, the dissipation of free energy by kinetics directly controls key parameters of battery performance such as polarization, rate capability, and most importantly useable capacity. The maximum theoretical capacity of the electrochemical cell is equal to the amount of charge generated, which assumes all Li ions involved in the electrochemical reaction are converted to electrons. This is calculated by Faraday's law

$$q_{max} = \frac{nF}{3600M} \tag{1.5}$$

where n is the number of Li ions and M is the molecular weight of the active material in the electrode. In reality the practical specific capacity is lower due to material and device constraints such as lithium/electron transport, interfacial ion transport, and phase transformations (**Fig. 1.3.b**). Bulk Li transport properties can be described Fick's first law

$$J_{Li} = -D\nabla c_i \tag{1.6}$$

where J_{Li} is the flux of Li atoms, D is the chemical diffusion coefficient, and c_i is the Li concentration. The diffusion coefficient often fluctuates with concentration due to effects from short range ordering, vacancy clusters, host structure stability, and specific site hoping mechanisms (**Figure 1.3.c**). In addition, there can be Li mobility transport affects from microstructure interfaces between grains/particles and phases. If there is local depletion (e.g. surface vs. bulk) of Li the resulting concentration gradient will cause polarization shifting the average voltage and capacity loss. These effects will be exacerbated at higher cycling rates as this concentration gradient increases.

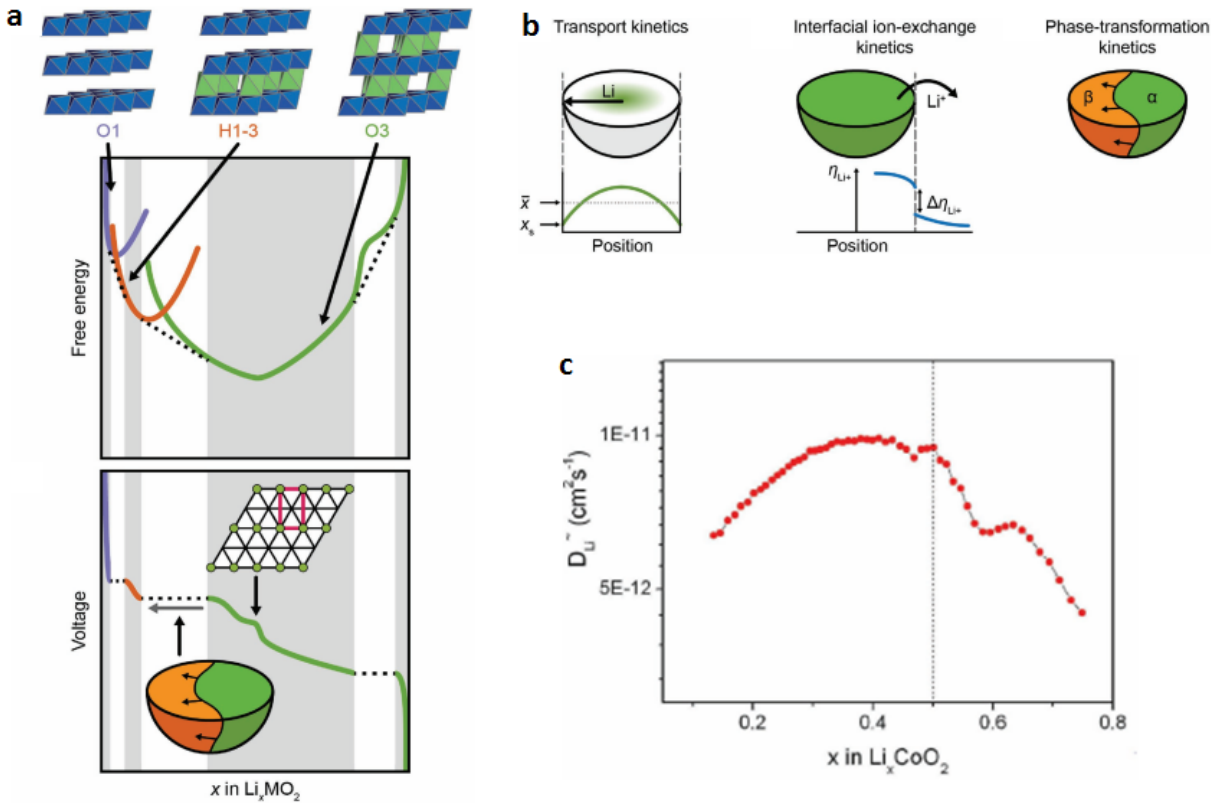

Figure 1.3. (a) Relationship between Gibbs free energy and voltage for a hypothetical electrode material.[4] (b) Transport and kinetic limitations in Li-ion cathode materials.[4] (c) Experimentally measured variation of chemical diffusion coefficient with state of charge in Li_xCoO_2.[4]

Understanding and minimizing these degradation mechanisms is necessary because the total energy contained in an electrochemical cell is given by the operating voltage and charge capacity

$$U = \int V dq \tag{1.7}$$

where V is the output voltage and q is the amount of charge supplied to the external circuit. This in turn determines the gravimetric energy density (Wh/kg) or volumetric energy density (Wh/L).

Finally, it is important to realize that the battery voltage is determined by the electrochemical potentials of the electrodes when they are placed in contact with an electrolyte, which serves as a medium to transport electroactive Li ions between electrodes, while blocking electrons. The electrochemical potentials in the electrodes in an actual cell differ from the individual isolated materials due to the electric double layers at the electrode/electrolyte interfaces, which shifts the electrostatic potential of the bulk electrode. This voltage must also be considered, because the practical battery operating voltage will be determined by the electrochemical stability window of the electrolyte. This gap between the highest occupied molecular orbital (HOMO) and lowest unoccupied molecular orbital (LUMO) determines the operating voltage range which minimizes deleterious side reactions in the chemical environments at the positive (oxidation) and negative (reduction) electrode.

Developing electrolyte materials is far from trivial as there is a delicate balance electrochemical stability, ionic conductivity, temperature, and safety. The relative stability of various liquid materials classes are shown in **Figure 1.4**. Current batteries use organic solvent mixtures such as ethylene carbonate (EC) and dimethylcarbonate (DMC), which have demonstrated to form stable inorganic phases and organic radicals, resulting in a stable

passivation layer or solid electrolyte interface (SEI). This enables use of a wider voltage window that the electrolyte stability window as the SEI decomposition products are electronically insulating to stop the adverse oxidation and/or reduction reactions and ionically conductive allowing Li ions to pass through. Proper engineering of this interface is crucial for improving capacity loss, cycle life, rate capacity, and safety.

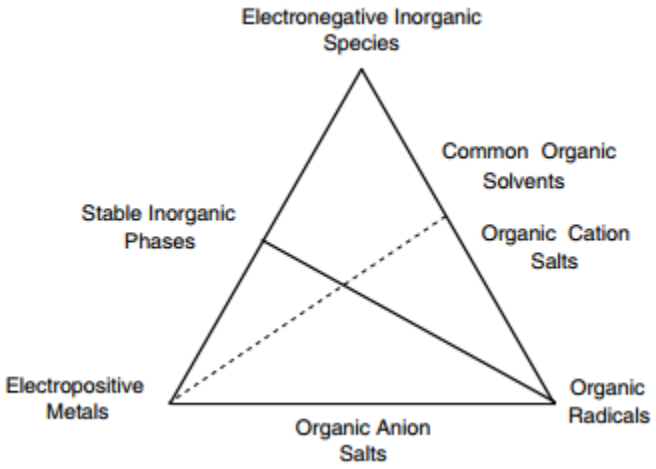

Figure 1.4. Generalized pseuodo-ternary stability diagram.[5]

However, as seen in **Figure 1.4** these liquid organic solvent electrolytes are not stable against electropositive metals such as Li. With the increased push to develop lithium-ion batteries with ever increasing energy, there is significant renewed interest in enabling a Li metal anode, due to its low electrode potential (-3.04 V vs. standard hydrogen electrode) and high theoretical specific capacity (3860 $mAhg^{-1}$). In early lithium metal batteries, due to this electrolyte instability, there were significant performance and safety hazards because of dendrite formation. A variety of approaches have been explored including: 1) host structures for Li[6-8]; 2) flexible coatings[8]; 3) liquid electrolyte chemistry engineering with additives[9, 10]; and 4) physical barriers to prevent dendrite formation such as polymer[4] and solid state electrolytes.[11-15]

1.3 Solid-State Batteries

Solid-state batteries are explored and developed due to their potential to enable storage devices with high specific energy density and high power density while mitigating safety and temperature stability concerns associated with conventional liquid lithium-ion batteries. Further, transitioning to an all solid-state battery could reduce packaging costs and weight, improve electrochemical stability, and improve mechanical stability. There is significant research effort to develop solid state electrolytes (SSEs), with much focus on discovering very high ionic conductivity solid electrolytes, with a now often stated benchmark goal of at least 1 mS/cm at room temperature.[16] $Li_{10}GeP_2S_{12}$, has a reported room temperature conductivity of 12 mS/cm, which even exceeds that of commonly used liquid electrolytes (**Fig. 1.5**).

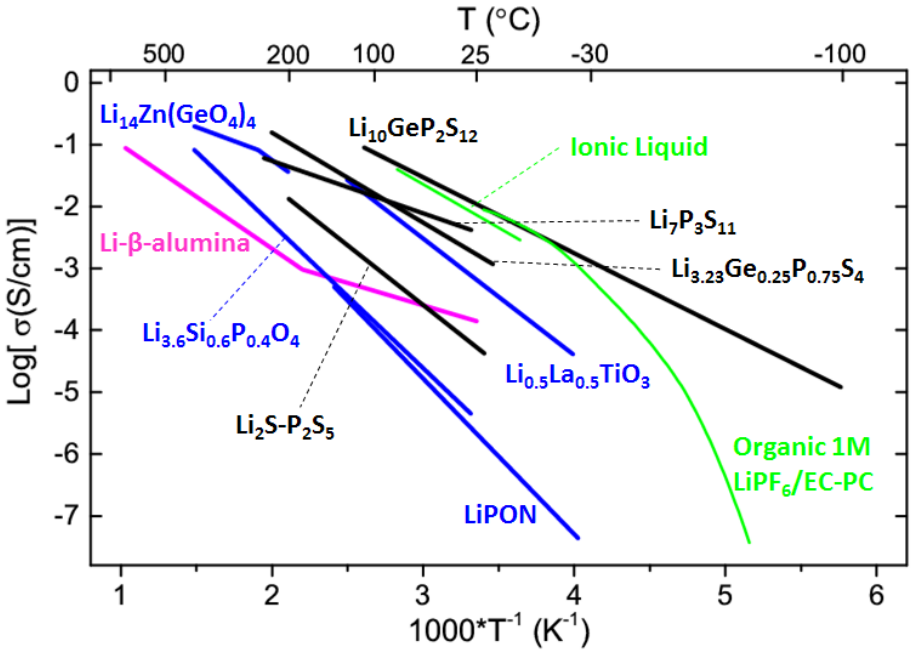

Figure 1.5. Ionic conductivity of several solid state and liquid electrolytes.[17]

However, the practical introduction of SSEs into full cell batteries is accompanied by other constraints, both intrinsic and extrinsic.[18] Intrinsically, though many SSEs exhibit high bulk ionic conductivity, grain boundaries may ultimately reduce the effective ionic conductivity to unusable levels, as in the case of solid oxide perovskite lithium lanthanum titanate (LLTO),[19] and may serve as regions of mechanical susceptibility, aiding lithium dendrite nucleation and penetration.[20] Extrinsically, questions of electrolyte/electrode interfacial impedance, resulting from space charge[21] and chemical and electrochemical compatibility[22, 23] of solid–solid interfaces, come into play. Despite the importance of these interfaces in the functionality of next-generation solid-state devices, there are surprisingly few studies focused on characterization of their interfaces.

While there are still significant scientific and engineering hurdles before the full potential of SSEs can be realized, there is significant optimism and promise due to the development and commercialization of solid-state thin film batteries. While they are limited to niche low energy applications, thin film batteries have demonstrated remarkable lifetime performance and stability. Furthermore, solid-state thin film battery materials and devices are a model system to enable fundamental studies ex-situ, *in* situ, and *operando*, to elucidate dynamic bulk and solid-solid interface properties

.

Chapter 2. Previous Work on Solid-State Thin Film Batteries

2.1 Solid-State Thin Film Batteries

All solid-state thin film batteries harness the inherent safety and performance benefits of solid-state batteries, but are very thin on the order of microns, which allow for easy integration into small footprint applications such as implantable medical devices, radio frequency identification (RFID) cards, microelectromechanical systems (MEMS), and micro-chip power. With increased miniaturization of chips and devices and development of ultra-low power electronics, especially in emerging areas such as personalized sensors and targeted healthcare, there will be increased need for small, conformal, and energy dense power sources.

Thin film batteries have been a focus of study since the 1980's, with researchers developing a wide range of materials with various techniques and architectures.[24, 25] The full promise of this technology was realized with the development of lithium phosphorous oxynitride (LiPON) by Bates et al. in 1992.[26, 27] LiPON not only had reasonable bulk electrolyte properties but also demonstrated outstanding electrochemical stability with a lithium metal anode and a lithium cobalt oxide ($LiCoO_2$) cathode, along with a relatively simple preparation process enabling ease of device fabrication and commercial scale up.

2.2 Thin Film Deposition Techniques

Although thin film batteries can deliver outstanding performance, the components are deposited onto a substrate bottom-up (**Fig. 2.1**), which significantly increases the materials, processing, and packaging costs. There are a variety of well-established deposition techniques optimized for various materials including: thermal evaporation, sputtering, pulsed laser deposition (PLD), sol-gel deposition, electrochemical deposition, and chemical vapor deposition

(CVD). Due to the complex chemical structure of many battery materials it is generally favorable to use high vacuum physical vapor deposition techniques.

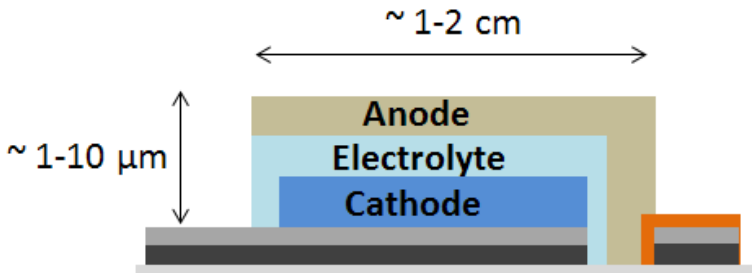

Figure 2.1. Schematic of solid-state thin film battery.

2.2.1 Thermal Evaporation

During thermal evaporation, a solid starting material inside a high vacuum chamber (~1x10^{-6} Torr) is heated to its evaporation temperature through absorption of thermal energy via Joule heating or electron beam (e-beam) heating (**Fig. 2.2.a-b**).[28] The vaporized particles then travel from the source material and condense into a thin film on the substrate. The high vacuum environment is crucial to minimize evaporated material collisions enabling anisotropic deposition with high purity.

The key to thermal evaporation is to heat the source material to a sufficient temperature to generate appreciable vapor pressure to sustain a reasonable evaporation rate. Empirically it has been demonstrated that the mass evaporation rate for a given material and pressure is

$$\Gamma_e = 5.84 \times 10^{-2} \left(\frac{M}{T}\right)^{1/2} P_e \qquad \frac{\text{g}}{\text{cm}^2\text{s}} \tag{2.1}$$

where P_e is the chamber pressure in torr, M is the molecular weight, and T is the absolute temperature. The key variable is the source temperature since it affects the equilibrium vapor pressure.

Given the Clausius-Clapyeron equation

$$\frac{dP}{dT} = \frac{\Delta H(T)}{T\Delta V} \tag{2.2}$$

where T is the transformation temperature, ΔV is the specific volume change, and $\Delta H(T)$ is the change in enthalpy of the phase transition. Assuming the vapor volume is significantly greater than the solid volume, equation (2.2) can be rewritten as

$$\frac{dP}{dT} = \frac{P\Delta H(T)}{RT^2} \tag{2.3}$$

We can approximate $\Delta H(T)$ as the constant molar heat of evaporation (H_e) and integrate to yield

$$lnP \cong -\frac{\Delta H_e}{RT} + I \tag{2.4}$$

where I is the constant of integration, which can be determined using the boiling point and latent heat of vaporization. Empirically the vapor-pressure data of many materials have been obtained, plotted, and extrapolated in **Figure 2.2.c**.

Thermal evaporation is primarily used for metals, because it can be very difficult to maintain complex stoichiometry transfer during the solid-vapor transition. Regardless there has been significant effort to enable growth of complex oxides, semiconductor materials, and alloys. During evaporation, compounds can decompose or disassociate, but losses can be minimized with proper process engineering such as co-evaporation of multiple compounds and manipulating the chamber pressure and gas chemistry, summarized in **Table 2.1**.

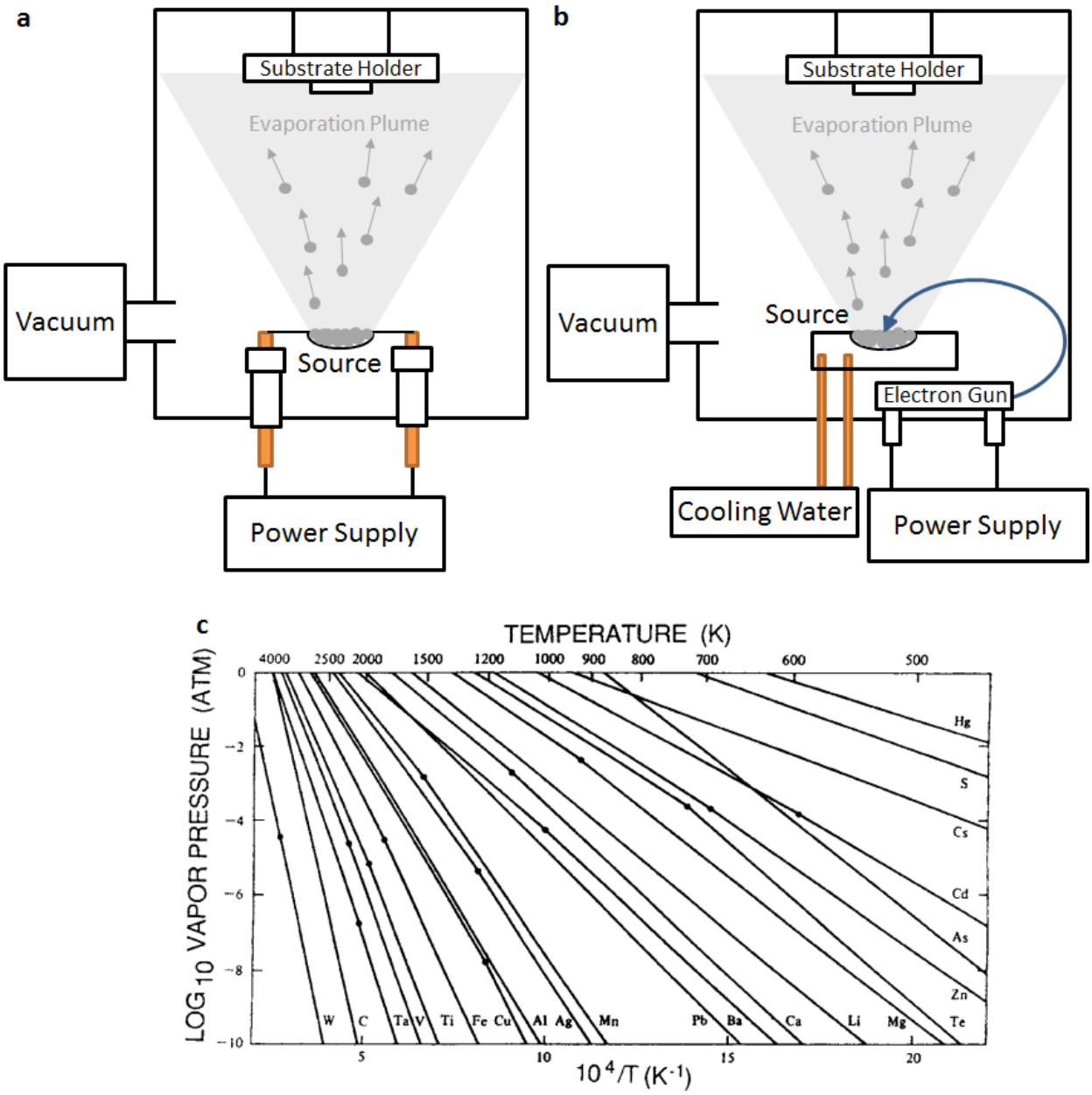

Figure 2.2. Schematic of (a) thermal evaporation system and (b) electron beam evaporation system. (c) Vapor pressures of various elements.[29]

Table 2.1. Summary of phenomena during evaporation of compounds.[28, 30]

Reaction Type	Chemical Reaction*	Examples	Comment
Evaporation without dissociation	$MX(s \text{ or } l) \rightarrow MX(g)$	SiO, B_2O_3, GeO, SnO, AlN, CaF_2, MgF_2	Compound stoichiometry maintained
Decomposition	$MX(s) \rightarrow M(s) + \frac{1}{2}X_2(g)$ $MX(s) \rightarrow M(l) + \frac{1}{n}Xn(g)$	Ag_2S, Ag_2Si GaAs	Separate sources required
Evaporation with disassociation			
Chalcogenides	$MX(s) \rightarrow M(s) + \frac{1}{2}X_2(g)$ X = S, Se, Te	CdS, CdSe, CdTe	Separate sources required
Oxides	$MO_2(s) \rightarrow MO(s) + \frac{1}{2}O_2(g)$	SiO_2, GeO_2, TiO_2, SnO_2, ZrO_2	Deposited in O_2 partial pressure

*M = metal, X = nonmetal

2.2.2 Radio Frequency (RF) Sputtering

Beyond thermal heating, thin films can also be deposited by sputtering a source target material by bombarding the surface with energetic ions. Again at high vacuum, the ejected particles then travel from the source material and condense into a thin film on the substrate. Inside of a sputtering chamber there is a pair of parallel plate electrodes hooked up to a power supply (**Fig. 2.3**). During radio frequency (RF) sputtering, a working gas (typically Ar, O_2, or N_2) is introduced to the evacuated chamber to serve as the medium for electrical discharge, which generates plasma. The positive gas ions bombard the target material, transferring kinetic energy, and sputter off atoms. There are numerous other energy exchanges inside the plasma, as secondary particles and negative ions are also emitted from the target along with radiation and local heating. The alternating applied electric field prevents buildup of charges species towards the substrate or target, allowing the deposition of insulating and nonmetal materials.

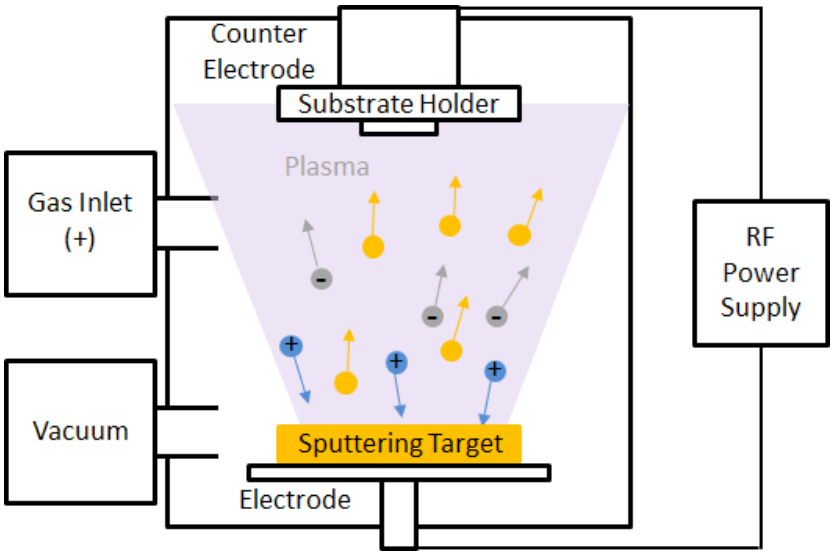

Figure 2.3. Schematic of RF sputtering system.

During the accelerated ion-solid bombardment, there are several surface and sub-surface interactions which affect the growth and material properties of the resulting film (**Figure 2.4**). Particle bombardment effects include: energy transfer resulting in sputtering, implantation, or defect formation; modifying the substrate surface via cleaning or defect formation; heat generation at the surface; and formation of secondary electrons that can affect plasma chemical. These in turn affect film properties such as adhesion, residual film stress, film morphology, density, grain size and orientation, surface coverage, pinhole density, and surface area. Tuning the ion beam energy is crucial for minimizing deleterious side reactions and maximizing sputtering yield (S). Sufficient energy must be transferred to the target atoms to overcome the threshold energy (E_{th}), which is most heavily influenced by the surface binding energy (U_s). Experimentally measured E_{th} for a variety of materials are compiled in **Table 2.2**.

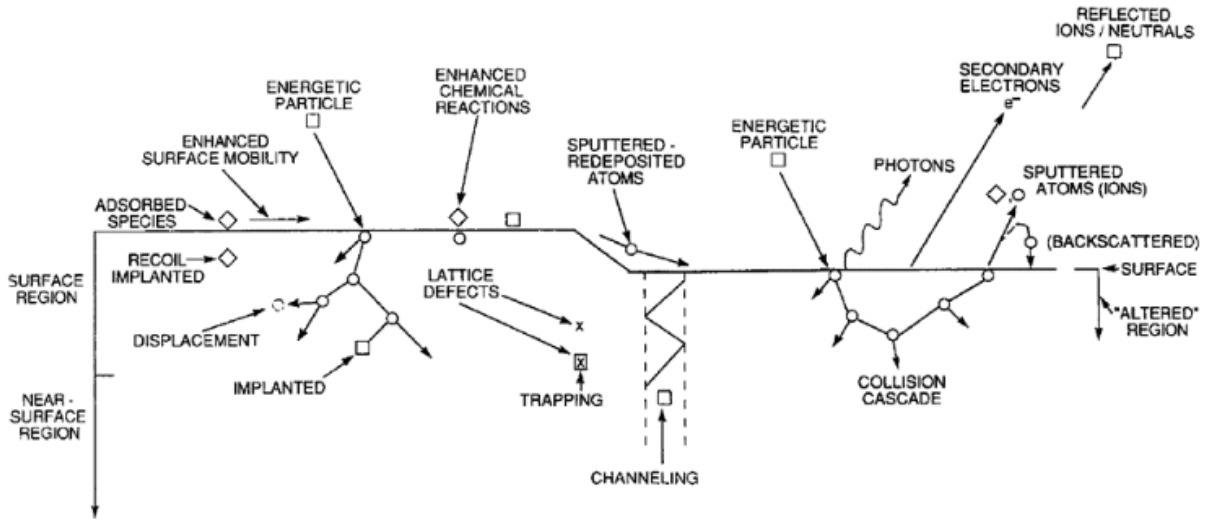

Figure 2.4. Schematic of possible interactions during ion-solid bombardment.[31]

Table 2.2. Summary of sputtering yields.[28]

Target	Ar (0.5 keV)	Ar (1.0 keV)	E_{th} (eV)
Ag	3.12	3.80	15
Al	1.05	1.00	13
Au	2.40	3.60	20
C	0.12		
Co	1.22		25
Cu	2.35	2.85	17
Fe	1.10	1.30	20
Ge	1.1		25
Mo	0.80	1.13	24
Ni	1.45	2.20	21
Pt	1.40		25
Si	0.50	0.60	
Ta	0.57		26
Ti	0.51		20
W	0.57		33
GaAs	0.83	1.52	20-25
InP	1.00	1.40	25

Unlike evaporation, sputtering enables deposition of composite films without stoichiometric loss. Although there is still a different vapor pressure and sputtering yield for each component, there is a lower discrepancy during sputtering conditions and since the target remains solid during deposition there is minimal diffusion and chemical reactions. This ensures a steady-state transfer of atoms to the plasma during deposition and maintains stoichiometry.

2.2.3 Pulsed Laser Deposition (PLD)

One further step towards enabling thin film growth of complex materials is to use pulsed laser deposition (PLD), where a high power laser (~2 J/pulse) is focused on to ablate the target source material, which then condenses onto the substrate (**Fig. 2.5**). This process can either be done at high vacuum or with a background gas to promote surface reactions and reduce kinetics; commonly O_2 or Ar. Most nonmetallic materials exhibit strong absorption in the ultraviolet (UV) range (200-400 nm) so gas excimer lasers are widely used including ArF (193 nm), KrF (248 nm), and XeCl (308 nm). The beam energy is absorbed by the target causing electron excitation and ablation forming a high directional plasma plume consisting of ions, electrons, atoms, molecules, and atom clusters. Considering possible thermal effects to the solid such as electron-lattice energy coupling, thermal conduction, and phase transition, during a femtosecond pulsed, there is insufficient time for energy transfer to the lattice so this can be considered a direct solid-vapor transition making thermal damage is minimal.[32] At longer pulse time lengths ablation can occur through melt expulsion driven by the vapor pressure and recoil pressure. But during the short pulses often used the energy is limited to a small depth and the absorbed energy heats the target very quickly past the melt to vapor phase. Due to the extremely fast and localized heating of the target, the stoichiometry of the target can be maintained for compounds that are difficult to process through other techniques, such as mixed oxides.

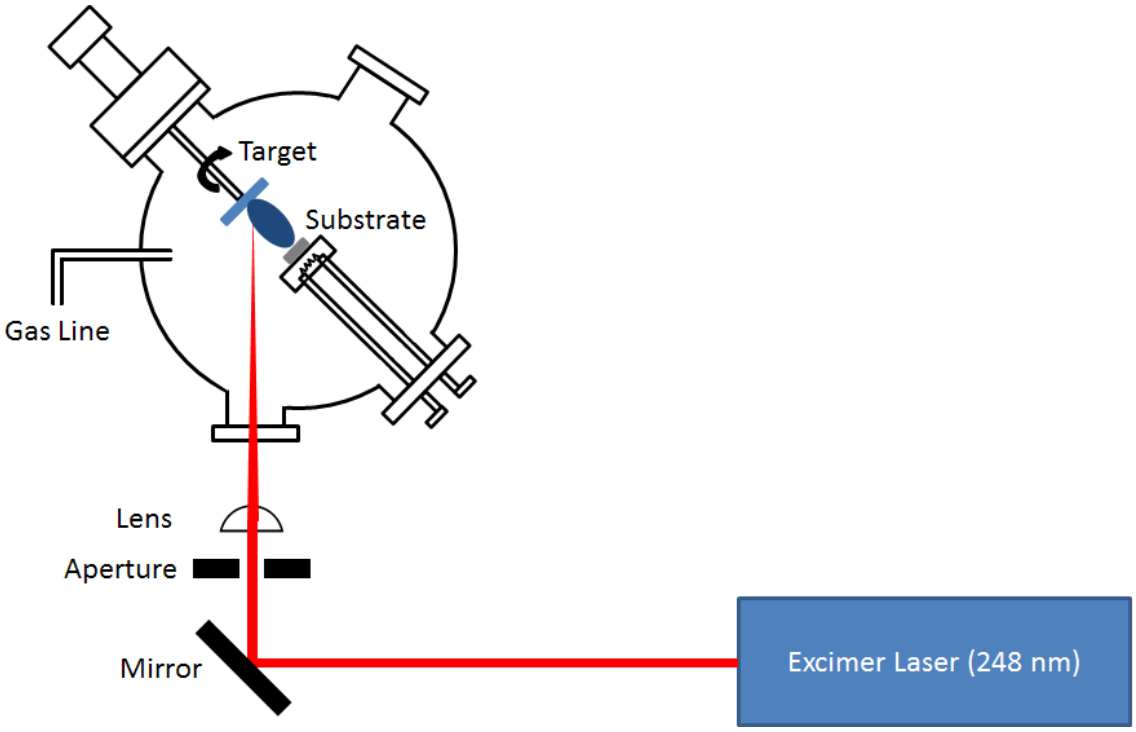

Figure 2.5. Schematic of pulsed laser deposition system.

Due to the nonequilibrium and high energy nature of the PLD ablation process, it is possible to induce stress during film growth through defect formation from impinging energetic species. High energy plume components can damage the underlying atoms in the growing film, implant into the film, or preferentially sputter the surface.[33] Further, while there is stoichiometric transfer of the target that does not guarantee that the film grown will maintain that stoichiometry. At high temperature, components with high vapor pressure will diffuse off such as Li, Na, Tl, Pb, Cd, and Zn.[34, 35] So when using such compounds excess material should be added to the target. Regardless, there has been significant success in depositing many ceramic complex oxides by PLD.

2.3 Components of Thin Film Batteries

2.3.1 Thin Film Cathodes

The current generation of lithium-ion batteries primarily use cathode materials that as classical lithium intercalation metal oxide layered structures ($LiMO_2$, M = Co, Ni, Mn) (**Fig. 2.6**). This structure is based on a close-packed network of oxygen atoms with the Li^+ and M^{3+} ions ordering on alternating (111) planes of the cubic rocksalt structure. The ordering of positive ions causes a distortion of the cubic lattice to a hexagonal symmetry (*R-3m*) with ABCABC stacking of the oxygen planes.[36] This material class has demonstrated low lithium diffusion barrier in the two dimensional plane perpendicular to the layered stacking, high electronic conductivity, low lithium chemical potential, and high capacity. Lithium cobalt oxide ($LiCoO_2$) is one of the first established and frequently used cathode materials, since Mizushima et al. demonstrated a 4.0 V voltage window in 1980.[37] The theoretical capacity of $LiCoO_2$ (LCO) is 272 mAh/g, but only half of the lithium can be extracted from the structure before major phase transformations leading to a significant capacity loss and in the extreme case oxygen loss.[38-40] Thus, during operation the cell is limited to 140 mAh/g capacity and 4.2 V operating potential.

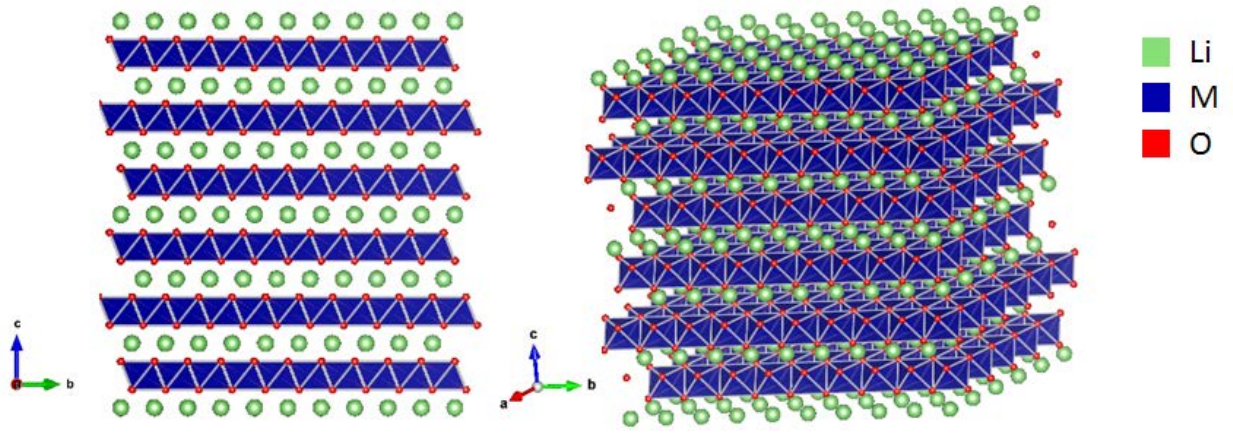

Figure 2.6. Crystal structure of layered $LiMO_2$.

$LiCoO_2$ thin films have been deposited by PLD[41, 42], CVD[43, 44], ALD[45], sol-gel deposition[46, 47], and the most common sputtering.[48-50] Films are usually deposited at room temperature with control over the working pressure, Ar/O_2 gas mixture, sputter power, and bias voltage. Afterwards the as-deposited films are annealed at high temperature (500-700°C) to crystalize the sample into a layered structure oriented normal to the surface necessary to enable facile Li ion extraction and intercalation. Higher annealing temperature results in a fully ordered layered structure improving electrochemical performance, but this heat treatment may cause strain and cracking which can lead to shorting in a solid-state thin film battery (**Fig. 2.7**). Proper optimization of the deposition and annealing parameters is necessary to balance the structural, mechanical, and electrochemical properties of the thin film cathode.

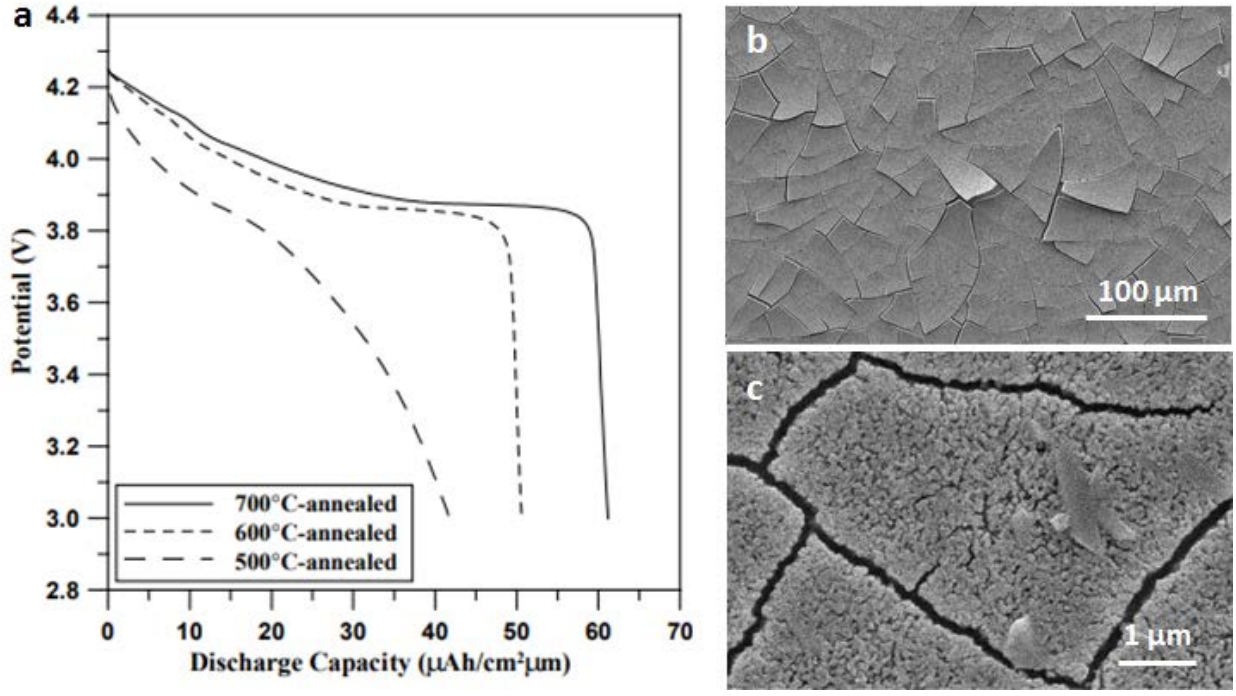

Figure 2.7. (a) Discharge curves for Li|$LiCoO_2$ cell with $LiCoO_2$ films annealed in O_2 atmosphere at 500, 600 and 700°C for 2 h.[50] (b-c) SEM images of post-annealing $LiCoO_2$ films showing significant cracking.

Another explored cathode crystal structure is LiM_2O_4 spinel which belongs to cubic *Fd-3m* space group with a cubic lattice constant of 0.825 nm (**Fig. 2.8**). In the spinel structure the transition metal occupies the octahedral sites (16d) and oxygen occupies the face centered cubic position (32e) creating a network of edge-sharing MO_6 octahedra, while Li occupies the tetrahedral interstices (8a). The three-dimensional host structure and vacancies enable three dimensional Li diffusion pathways.

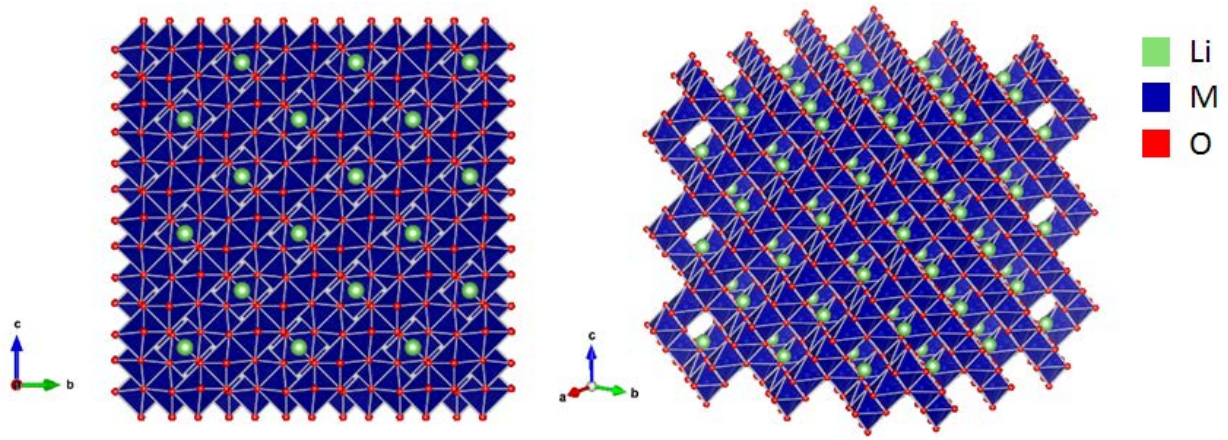

Figure 2.8. Crystal structure of spinel LiM_2O_4.

Interest in spinel cathodes was spearheaded by the discovery of lithium manganese oxide ($LiMn_2O_4$) by Thackeray et al. in 1983 as a stable host structure for Li ion insertion and extraction.[51] Its working voltage is around 4 V and the theoretical capacity is 148 mAh/g, but practical capacity is limited to ~110 mAh/g due to structural stability concerns (80% Li extraction). $LiMn_2O_4$ thin films have been deposited via PLD[52], sputtering[53, 54], CVD[55], and sol-gel deposition.[56] Surprisingly, while conventional $LiMn_2O_4$ is known to suffer from severe capacity fading due to (1) Jahn-teller effects during deep charge and discharge causing lattice structure distortion (the ratio of lattice constant c/a increases by 16%) and volume expansion

resulting in collapse of the spinel structure[57] and (2) dissolution of Mn^{2+} into the electrolyte from adverse reactions with trace amounts of water in the electrolyte,[58, 59] thin film $LiMn_2O_4$ maintains excellent cycling performance (**Fig. 2.9**). This is because the solid-state thin film device mitigates the strain generated during the Jahn-Teller distortion volume expansion and contraction and transition metal dissolution.

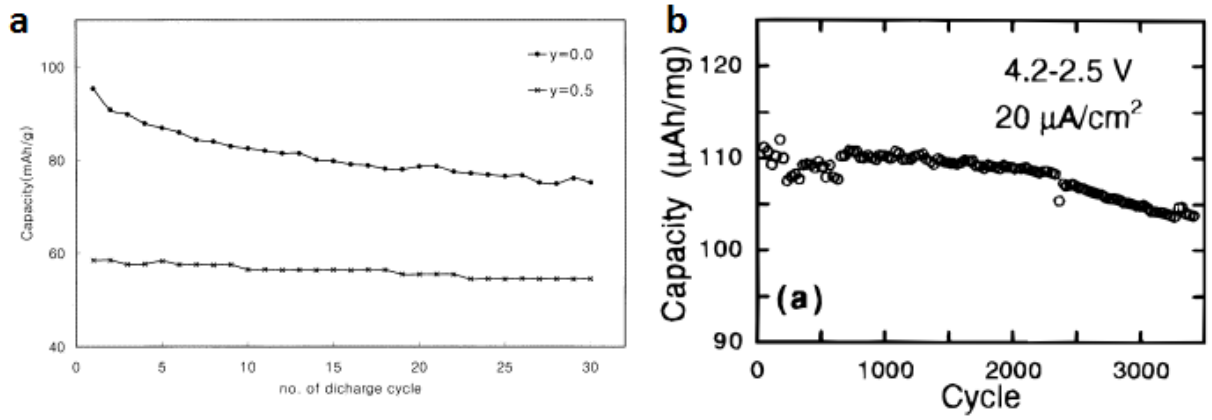

Figure 2.9. Discharge capacity of (a) $LiFe_yMn_{2-y}O_4$ (**y**=0.0 and 0.5) cycled between 3.5 and 4.3V in a conventional liquid electrolyte cell[60] and (b) $LiMn_2O_4$ thin film deposited by RF magnetron sputtering cycled between 2.5 and 4.2V in a solid-state thin film battery.[53]

The voltage and capacity limit of the cathode can be manipulated by chemical substitution of various transition metals in the structure. Substituting Ni into $LiNi0_{.5}Mn_{1.5}O_4$ (LNMO) creates a cathode that maintains a high theoretical capacity of 147 mAh/g, while increasing the operating voltage up to 5.0 V due to the double Ni^{2+}/N^{4+} redox couple. However, implementation of this promising cathode is limited due to incompatibility with current liquid electrolytes, which are not stable above ~4.5 V. The decomposition reactions create a detrimental SEI leading to capacity fade and poor cycle life.[61, 62] Further, just like with $LiMn_2O_4$ trace amounts of water in the liquid electrolyte react with the $LiPF_6$ salt to produce hydrofluoric

acid causing Mn^{2+} dissolution.[59] Attempts to mitigate this primarily focus on new liquid electrolyte development such as high concentration salt[63-65] and protective metal oxide[66, 67] or polymer coatings.[68] Such adverse decomposition reactions would be avoided in a solid-state device, and LNMO thin films have be fabricated by PLD[19, 69, 70], sputtering,[71, 72] and sol-gel deposition[73] with excellent performance.

2.3.2 Lithium-ion Thin Film Anodes

Silicon (Si) is a highly promising anode material because of its high theoretical capacity (4200 mAh g^{-1} vs. graphite 372 mAh g^{-1}), low discharging potential (0.2 V with respect to Li/Li^+), low cost, and well-developed industrial infrastructure.[74, 75] However, the implementation of Si anodes has been hindered by its rapid capacity fade during electrochemical cycling and poor coulombic efficiency. This is because Si exhibits a high volume expansion during lithiathion and delithiation (~300%) resulting in mechanical degradation of the electrode structure.[76] Additionally, as the electrode surface fractures the new surface is exposed to the electrolyte causing a constant thickening of the solid-electrolyte interphase (SEI) leading to irreversible charge loss.

Studies have shown that various nanostructures can mitigate mechanical fracture improving cycling performance.[74, 77, 78] With this motivation, extensive work has been done to understand intersection of nanostructures, stress evolution, volume changes, and mechanical failure.[79-81] We can now create nanostructures specifically engineered to minimize volume expansion, such as core-shell nanotubes and yolk-shell assemblies.[82, 83] This effort has revealed a wealth of fundamental information such as the effect of crystallinity on volume expansion and

models of stress evolution. However there are real challenges to the industrial scalability and development of nanostructured silicon anodes.

Si anode thin films have been deposited by thermal evaporation,[84] sputtering,[85] and PLD.[86, 87] When Takamura et al. deposited 50 nm silicon thin films by thermal evaporation the sample demonstrated stable high specific capacities of 3600 mAh/g at 2C rate for 200 cycles corresponding to the maximum lithiation of $Li_{15}Si_4$ phase.[84] However, thicker films of 300-440 nm decreased to ~2000 mAh/g at 1C rate with poor capacity retention. Silicon films have a critical thickness of 100 nm before mechanical strain during cycling will cause cracking and irreversible capacity loss (**Fig. 2.10**).[85]

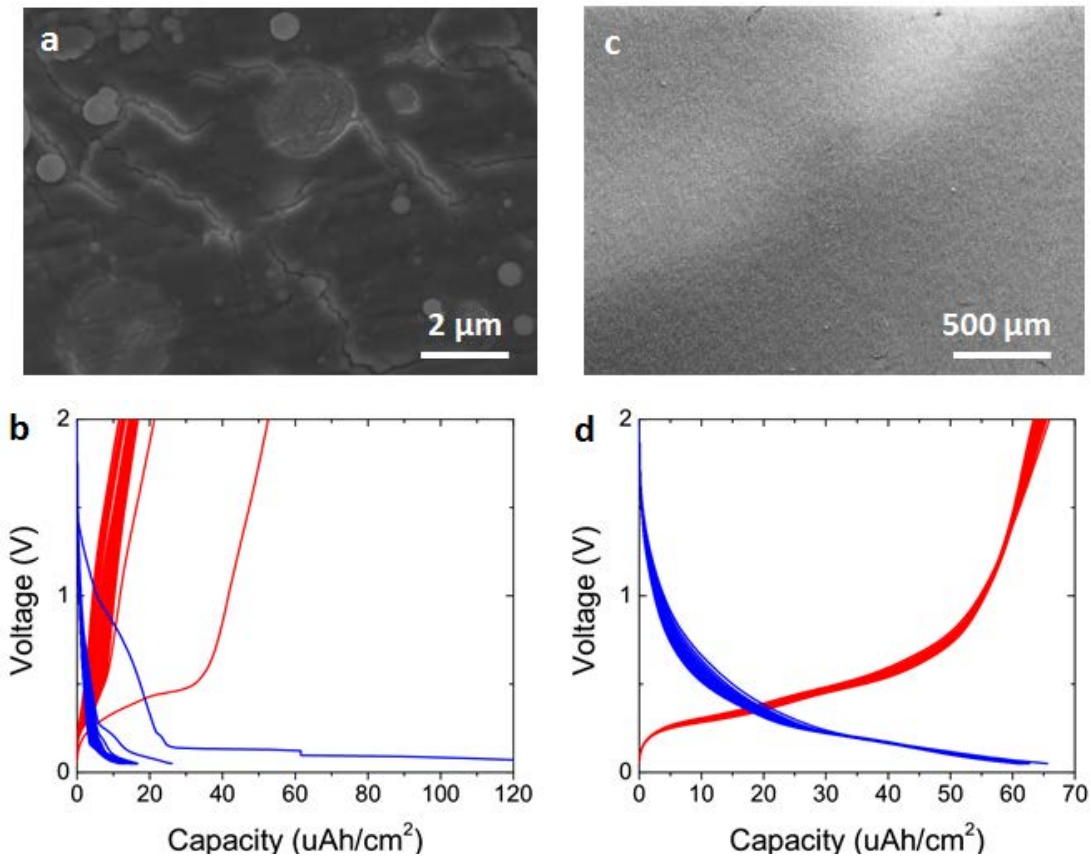

Figure 2.10. SEM image along with charge and discharge curves cycled between 0.05 and 2 V of Si thin films (a-b) 200 nm thick and (c-d) 80 nm thick.

However, most thin film batteries use lithium metal as the anode, due to its superior electrochemical properties. Li thin films are deposited by thermal evaporation, but system design and maintenance is crucial because Li is very oxygen and moisture sensitive. It is recommended to use a thermal evaporator installed inside of a glovebox for sample preparation. In addition, a high quality encapsulant is needed to prevent any adverse reactions once the sample is removed from the glovebox for any tests or analysis.

2.3.3 Lithium-ion Thin Film Electrolytes

Thin film electrolytes are required to have high ionic conductivity (>10^{-6} S/cm), low electronic conductivity, good adhesion and conformal, mechanically robust, and both chemically and electrochemically stable when in contact with the electrodes. Current commercial thin film batteries are based on amorphous lithium phosphorous oxynitride (LiPON), which have demonstrated an ionic conductivity of 2 x 10^{-6} S/cm, stability against lithium metal anodes, and a wide stability window up to 5.5 V.[26, 27]. Amorphous and glassy compounds have the added advantage where most thin film techniques preferentially deposit the amorphous phase of a material. Later annealing steps are needed to crystalize such films, adding processing complexity and increased energy costs. LiPON films have been fabricated by PLD[88], ALD[89], and most commonly by RF sputtering a Li_3PO_4 target in a chamber with N_2 partial pressure to incorporate nitrogen into the oxide network.[90, 91] This increases cross-linking between the chains of PO_4 tetrahedron due to the substitution of non-bridging oxygen ions in the glass network by doubly (P-N=P) and triply (P-N<P) coordinated nitrogen (**Fig. 2.11**).

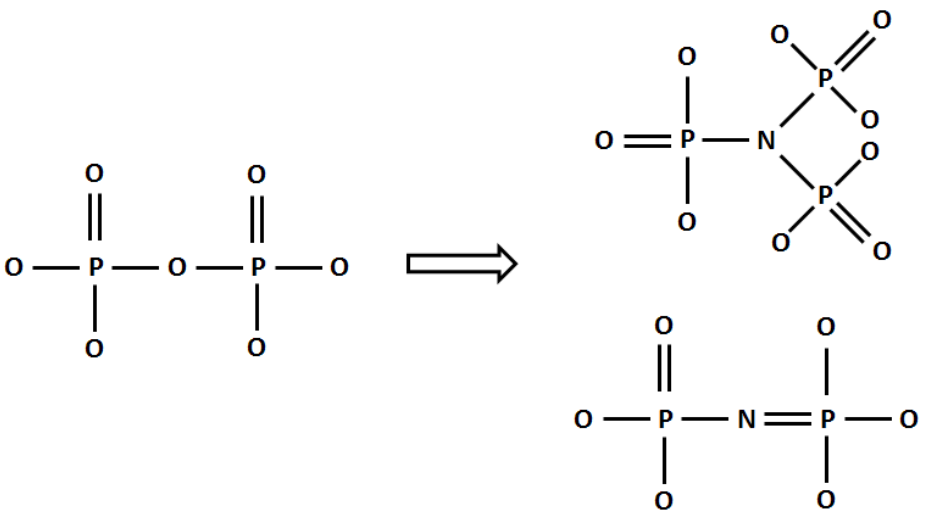

Figure 2.11. Schematic of how nitrogen is incorporated during the formation of LiPON.

This nitrogen coordinated cross-linked structure increases the film ionic conductivity and stabilizes the film against lithium metal through the formation of a Li_3N passivation layer. In addition, the resulting film is dense, pinhole free, and free from any columnar microstructures allowing easy integration with textured electrodes (**Fig. 2.12.a-b**). The composition ($Li_xPO_yN_z$) and ionic conductivity can be optimized by varying the sputter power, nitrogen pressure, and substrate temperature (**Fig. 2.12.c**). The ternary diagram also indicates that the LiPON composition is well outside of the normal glass forming region. This metastable state cannot be formed by traditional bulk synthesis techniques, and so far synthesis of this material has been limited to thin film processing techniques with an energetic nitrogen source (e.g. plasma).

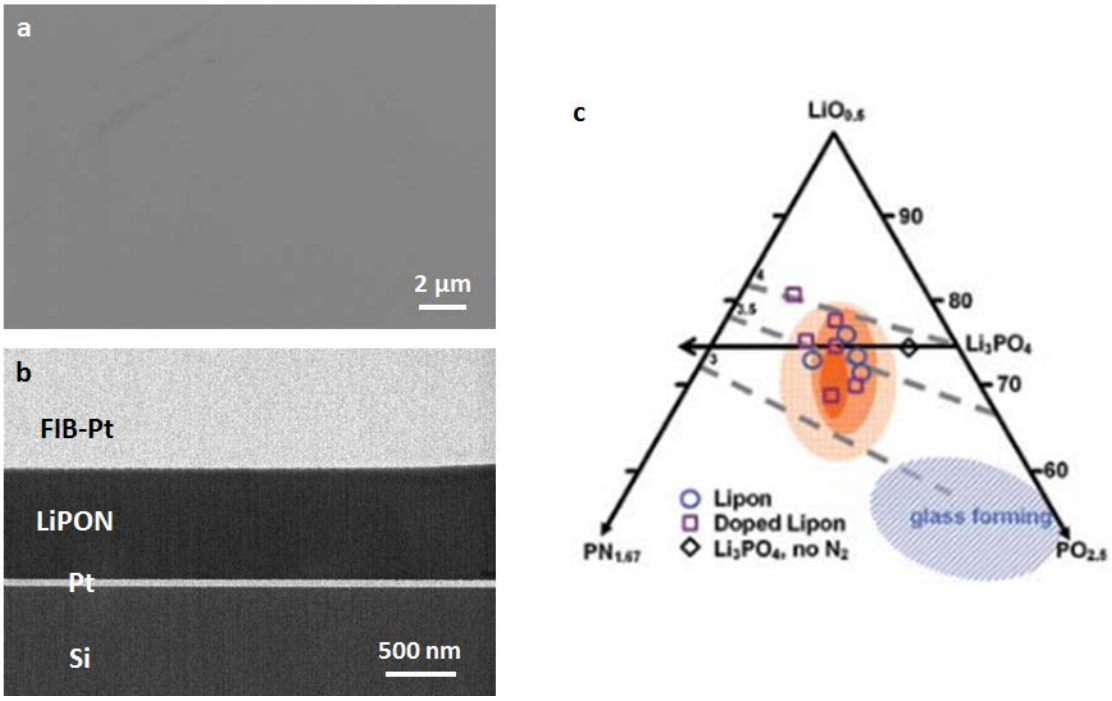

Figure 2.12. (a) SEM and (b) TEM image of LiPON. (c) LiPON composition range with orange shaded areas with ionic conductivities exceeding 0.5, 1.0, and 2.0 µS/cm. Dashed lines indicate constant ratios of (N+O)/P. The blue shading indicates the approximate compositions for glasses formed from a melt.[92]

There have been efforts to enable other thin film electrolytes following the progress in the development of bulk SSEs perovskite lithium lanthanum titanate (LLTO), garnet lithium lanthanum zirconate (LLZO), and sulfide electrolytes with varying degrees of success. While these films may show improvement in ionic conductivity, there has been difficulty in capturing all the material requirements to enable successful integration into a full device. Often there are stability issues when in contact with electrodes increasing cell impedance, decreasing cell performance and safety.

2.4 Lithium-ion Thin Film Devices

To date all successful thin film batteries use an amorphous electrolyte, which may minimize both detrimental intra-film inhomogeneity and electrode/electrolytes interfacial issues. Various cathodes combined with LiPON electrolyte and Li metal anode have been explored demonstrating hundreds thousands of deep cycles with little capacity loss (**Fig. 2.13.a**). This is attributed to: the stability of LiPON, the ability of the thin film materials to accommodate the volume changes associated with the charge-discharge reactions, and the uniformity of the current and charge distribution in the thin film structure. The batteries gradually become more resistive with cycling at rates dependent on the particular electrode chemistry, film thickness, voltage range, and operating temperature.

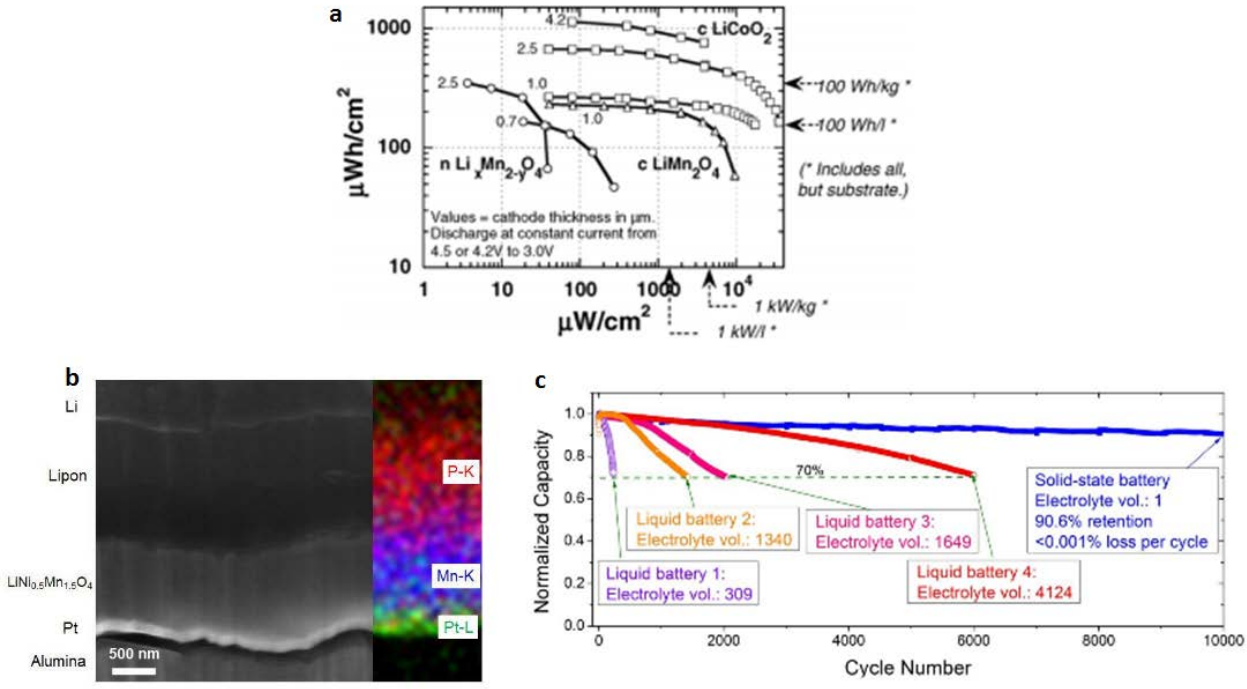

Figure 2.13. (a) Power and energy density of thin film batteries of various cathodes.[93] (b) SEM image, EDX elemental mapping, and (c) capacity retention of LNMO thin film battery cycled between 3.5 and 5.1 V.[72]

Recently a thin film LNMO/LiPON/Li thin film battery demonstrated remarkable long term stability when cycled up to 5.1 V, with 90% capacity retention after 10,000 cycles far outperforming its liquid counterpart (**Fig. 2.13.c**). This is due to the wide LiPON electrochemical window preventing decomposition reactions at these high voltages. Further, SEM imaging and EDX mapping indicate good adhesion, smooth contact, and chemical stability at the LiPON/electrode interfaces and a device free from any mechanic defects (**Fig. 2.13.b**). Often the electrode/electrolyte interface directly determines the performance of solid-state batteries, but there are surprisingly few studies focused on characterization of their interfaces, likely due to dearth of effective characterization techniques for probing these buried interfaces.

2.5 Solid Electrode-Solid Electrolyte Interface

Until recently, electrochemical techniques, primarily cyclic voltammetry (CV) and electrochemical impedance spectroscopy (EIS), were the main methods of characterizing buried interface resistances. These studies are prevalent in characterization of all-solid-state thin film batteries, such as $LiCoO_2$ (LCO)/lithium phosphorus oxynitride (LiPON)/Li[94] and LCO/$Li_{1.5}Al_{0.5}Ti_{1.5}(PO_4)_3$ (LATP) chemistries.[95] Electrochemical testing of such cells suggested growing interfacial impedance, vaguely attributed to modified chemical bonding impacting charge-transfer characteristics. Thermal annealing studies showed reduced interfacial resistances and improved cyclability of the LCO/LiPON/Li cells, though physical interpretation was speculative, lacking further experimental evidence and simply attributing the change to modified bonding at the LCO/LiPON interface.[96] The LCO/LATP cell utilized *in situ* formation of the anode, showing low charge-transfer resistance, though the nature of the anode was unknown at the time of the electrochemical testing.[95]

Similar studies further evaluated the stability of an interface or interlayer, such as the insertion of a Nb interlayer between LCO and lithium lanthanum zirconium oxide (LLZO) electrolyte, observing reduced interfacial impedance without explicit mechanistic descriptions.[97] That is not to say that electrochemical methods are insufficient methods of probing such interfaces. In scenarios where constituents are expected to be kinetically stable, careful experimental design promotes isolation of such effects, as in the case of idealized solid-state interfaces such as some silver conductors.[98] Control of materials selection can allow electrochemical methodologies to effectively isolate sources of charge-transfer resistance to the impact of lattice mismatch, defect chemistry, and equilibrium potentials.[99]

Until recently, the nature of stability of solid-state interfaces in applied lithium-ion battery materials was largely unknown, and questions of compatibility at interfaces was ascribed generally to issues of charge transfer across interfaces. Density functional theory (DFT) calculations were successfully employed to predict engineered interphases to counteract the effects of space charge, uncovering lithium niobite ($LiNbO_3$) as a candidate to stabilize the cathode/sulfide–electrolyte interface.[100] The insertion of a $LiNbO_3$ interlayer at the LCO/LiPON interface was shown via X-ray photoelectron spectroscopy (XPS) to modify lithium concentration, attributed to non-faradaic Li migration.[101] A following body of computational research opened the question as to the thermodynamic stability of these interfaces—a fundamentally important step in interpreting the nature of these buried interfaces, providing potential explanations for the presence of interfacial resistances at solid-solid interfaces.[23, 102] This work suggests that stable solid-state interphases effectively bridge the electrochemical window in much the same way the solid eelectrolyte interface (SEI) does in their liquid electrolyte counterpart.

Thermodynamically driven decomposition is most clearly shown after applying high-temperature processing methods. Combining results of electrochemical testing with ex situ evaluation has proven to be an effective technique for a more comprehensive understanding of the stability of solid-–solid interfaces, and has yielded many results consistent with computational predictions. For the case of LCO/LiPON, LCO was predicted to decompose into a variety of constituents, dependent on the local bonding environment and lithiation state.[102] Experimentally, it was observed that cycling LCO/LiPON/Li thin-film batteries at elevated temperatures resulted in increasing interfacial impedance values (**Fig. 2.14**). When extracted by a focused ion beam (FIB) system and observed by scanning transmission electron microscopy coupled with electron energy loss spectroscopy (STEM/EELS), the increased interfacial impedance was correlated with the growth of a structurally decomposed LCO interlayer, exhibiting chemical signals consistent with Li_2O and disordered rock salt Co_3O_4.[103]

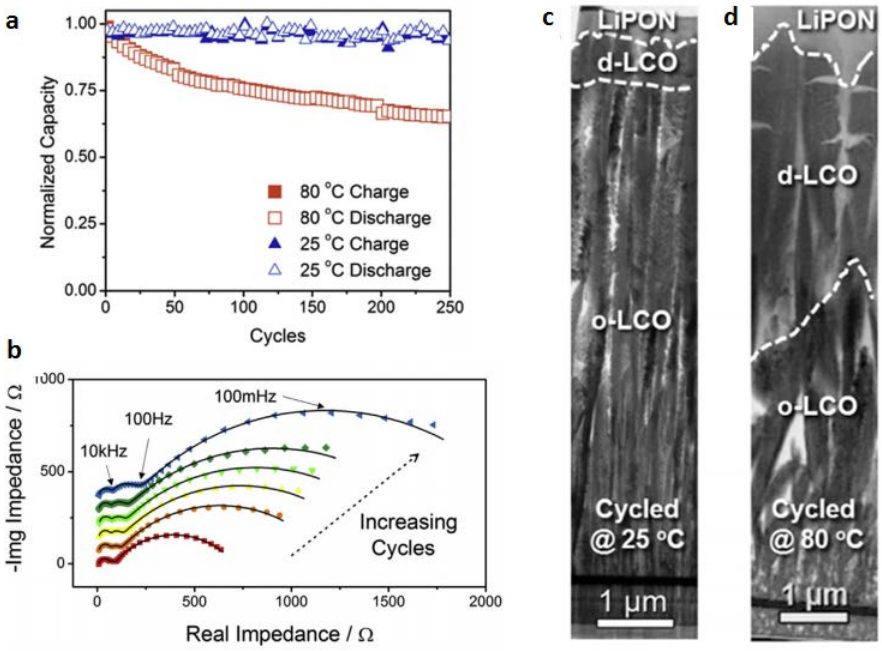

Figure 2.14. (a) cycling capacity, (b) electrochemical impedance spectroscopy and (c-d) TEM images of LCO/LiPON/Li thin film batteries cycled at 20°C and 80°C.[103]

Chapter 3. Overview of Advanced Characterization Techniques

3.1 Focused Ion Beam

Focused Ion Beam (FIB) systems are a heavily used tool in both industrial and academic fields, enabling fundamental studies to failure analysis of commercial devices. In a focused ion beam, a finely tuned beam of ions, usually gallium ions, is accelerated and focused by electrostatic lenses and rastered over the desired sample area. The resulting ion-solid interactions not only produce secondary electron emissions that can be used for imaging, but also cause sputtering of the sample material that can be used for micromachining.

A FIB instrument consists of a vacuum system and chamber, a liquid metal ion source, an ion column, a sample stage, detectors, gas delivery system, and a computer to run the instrument. They can either run independently or be integrating with other vacuum systems, most often with an SEM into a dual beam FIB/SEM. The capabilities of the FIB for small probe sputtering are made possible by the liquid metal ion source (LMIS), which provides a source of ions of ~5 nm in diameter. There are several metallic elements or alloy sources that can be used but gallium is the most common due to its low melting temperature (29.8°C at standard atmospheric pressure), low volatility, low vapor pressure, and low surface energy (**Fig. 3.1.a**). Ga ion emission occurs when (1) molten liquid gallium flows from the reservoir to the needle tip (tip radius ~5 μm), where an electric field causes the liquid Ga to form a point source in the shape of a "Taylor cone" (~2-5 nm) and (2) the extraction voltage pulls Ga from the tip creating a field emission of Ga^+ ions to form an ion beam. During this process a flow of Ga to the cone continuously replaces the evaporated ions. A finite voltage is needed to create the Taylor cone shape and result in a baseline emission current, which can then be increased with applied voltage. However, with

higher emission current there is increased likelihood of forming dimmers, trimers, charged clusters, and charged droplets. Once the Ga^+ ions are extracted from the LMIS, they are accelerated the ion column, which typically consists of (1) a condenser lens to form the probe and (2) an objective lens to focus the beam of ions at the sample surface (**Fig. 3.1.b**). Apertures of various diameters help define the probe size and provide a range of ion currents for different applications. The beam shape is optimized by centering each aperture, tuning the column lenses, and fine tuning the beam with the use of stigmators. And deflection plates are used to raster the beam over the sample surface.

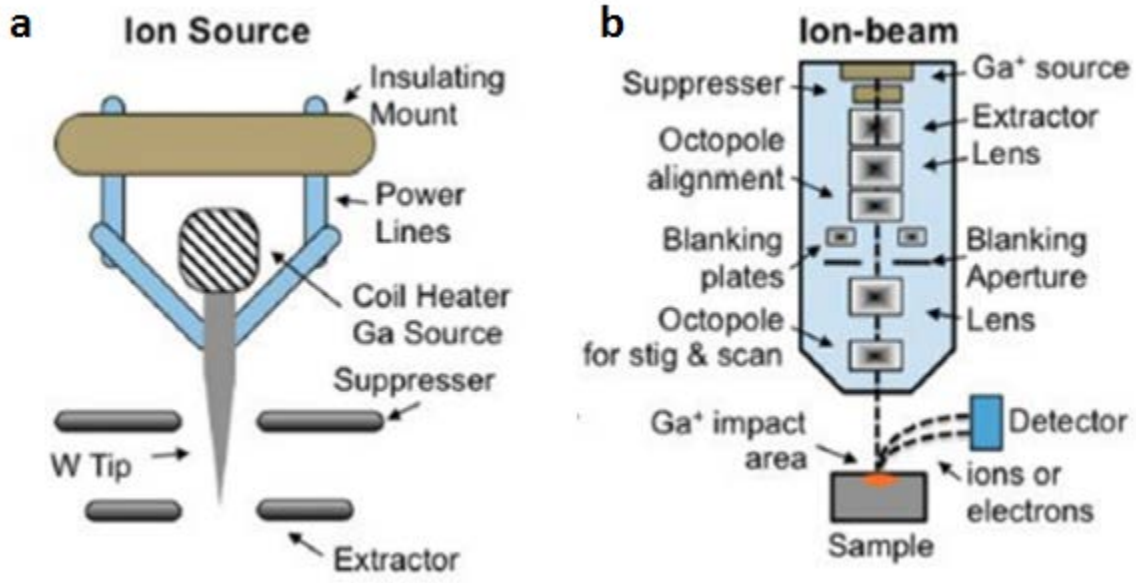

Figure 3.1. Schematic (a) liquid metal ion source (LMIS) and (b) focused ion beam (FIB) system.[104]

When the energetic Ga^+ ion hits the sample surface, kinetic energy is lost through ion-solid interactions resulting in a combination of backscattering (imaging), electron emission, electromagnetic radiation, implantation, sputtering, sample damage, and sample heating (**Fig. 3.2**). Ion milling requires considerable ion-solid elastic collisions where momentum is

transferred from the incident ions to the sample atoms within a collision cascade region. A surface atom will be ejected as a sputtered particle if it receives kinetic energy sufficient to overcome the surface binding energy (SBE) of the target material. Further inelastic scattering events can result in the production of phonons, plasmons, and the emission of secondary electrons (SE), which are detected for FIB imaging. Ion beams are not as finely focused as electron beams leading to lower resolution; however, ion induced secondary electrons offer various different contrast mechanisms that are not available for electron induced secondary electrons.

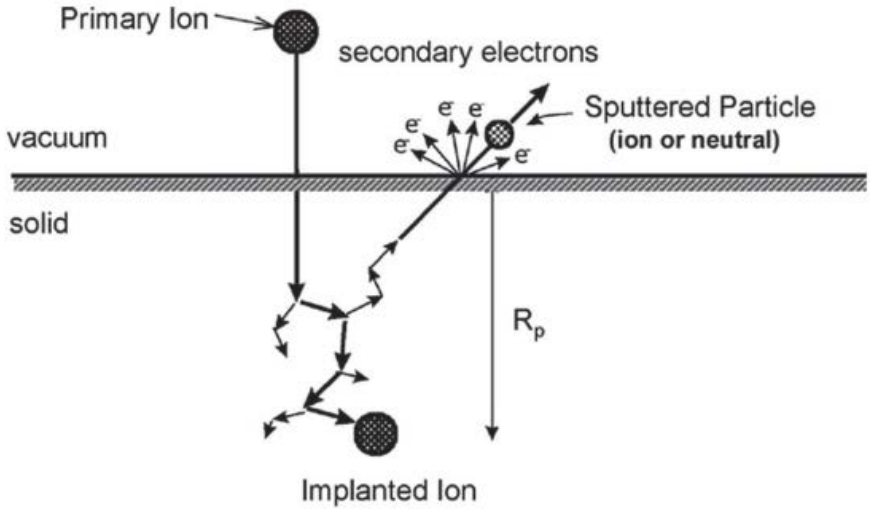

Figure 3.2. Schematic ion-solid interactions.[105]

If the incident Ga^+ ion is not backscattered out, it will eventually stop and stay implanted in the sample and some depth (R_p). After approximately 10^{-11} s, the Ga^+ ion comes to rest in the solid stopping the collision cascade, but there are still effects from emitted particles and radiation, and ion beam damage such as lattice defects, Ga implantation, and heat, all of which may continue to interact and evolve.[106] Monte Carlo calculations using the TRIM software

package are also well suited to simulating ion–solid interactions, and highlight important trends such as the correlation between melting temperature, density, and ion implantation (**Fig. 3.3**).

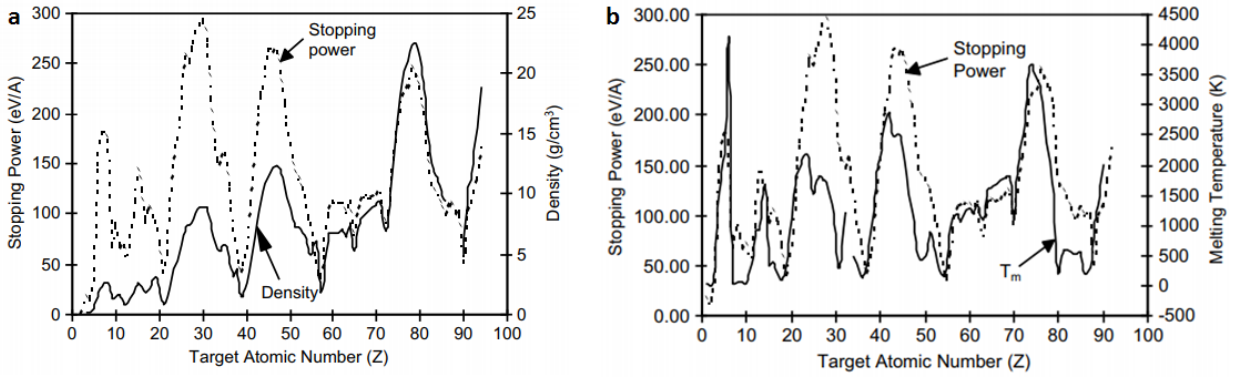

Figure 3.3. TRIM calculations to measure the total stopping power of a Ga^+ beam at 25 keV at 0° incident angle into various materials.[105]

The sputtering yield, is defined as the number of ejected particles per incident ion. Sputtering can be considered statistical phenomena caused by surface erosion on an atomic scale. Thus the more collisions that take place proximal to the surface, the higher the sputtering yield will be. The position of the cascade is determined by the nuclear stopping power of an ion in a given target material and the incident angle of the beam with respect to the target surface, which can be modeled with TRIM (**Fig. 3.4.a-b**). The periodic fluctuations in sputtering yield are manifestations of the influence that the interatomic potential exerts on the physical properties of a given material. Determining the sputtering yield for various elements indicates that periodic trends, associated with electronic structure of the elements, exert a controlling influence on the sputtering yield (**Fig. 3.4.c**). Thus it is intuitive that sputtering yield correlates with melting temperature, which in an indication of bond strength. The more tightly bound an atom is, the more difficult it will be to eject it as a sputtered particle. SEM images of FIB cross-sections

milled under constant conditions into different elements highlight the variable sputtering yield (**Fig. 3.4.d**).

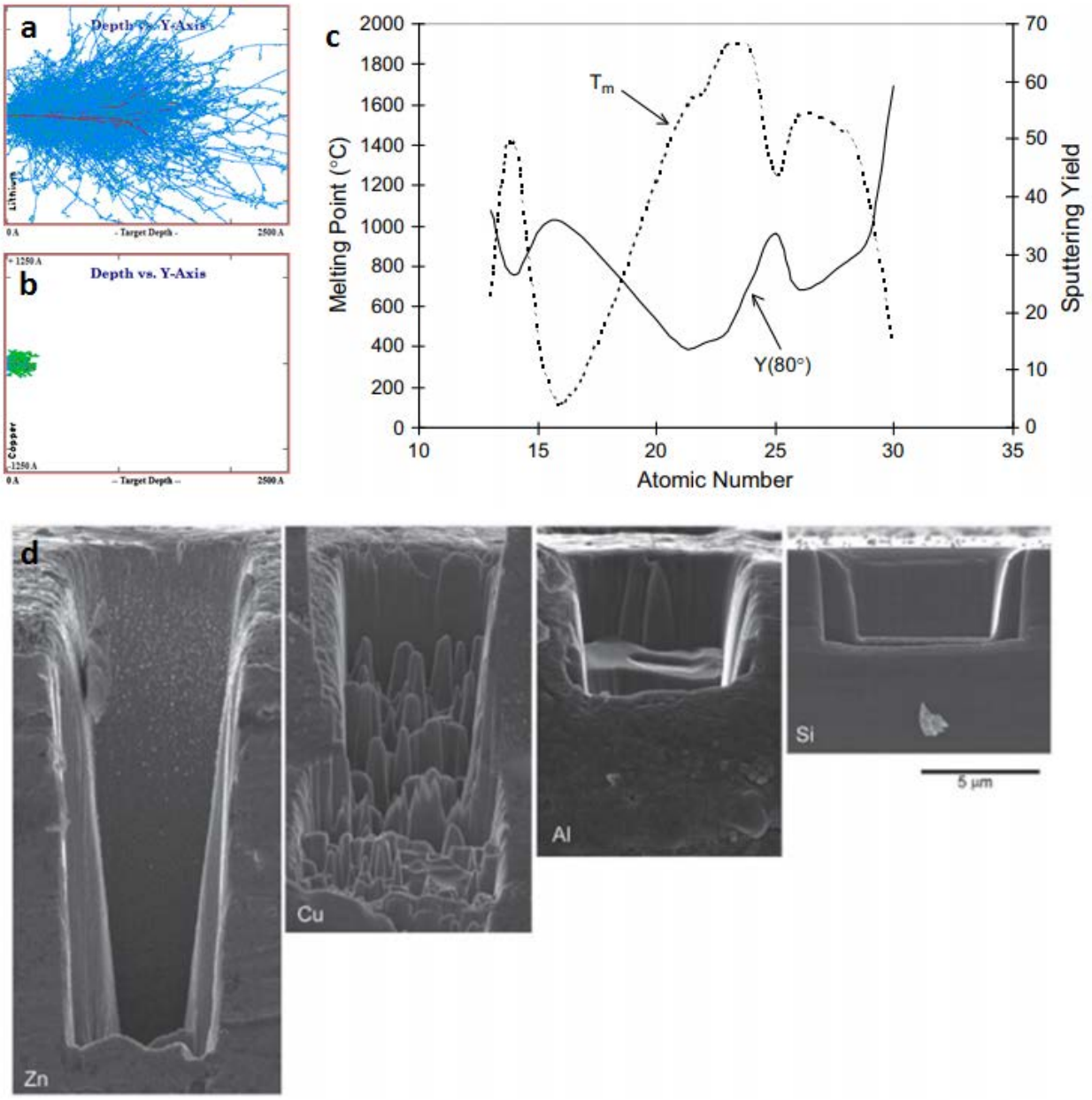

Figure 3.4. TRIM cascade models of 25 keV Ga^+ ions at 0° incident angle in (a) Li and (b) Cu and (c) resulting sputtering yields.(d) SEM images of FIB cross-sections milled at 25 keV and 0.1 nA for various materials.[105]

3.2 Transmission Electron Microscopy

Transmission electron microscopy (TEM) is a high resolution imaging technique where electrons and transmitted through an ultra-thin sample. The resolution (d) of a perfect optical system is described by Abbe's equation

$$d = \frac{0.612\lambda}{n \sin \alpha} \tag{3.1}$$

where λ is the imaging radiation wavelength, n is the index of refraction of the medium, and α is the half aperture angle. The wavelength of an electron can be approximated when ignoring relativistic effects as

$$\lambda = \frac{1.22\ nm}{\sqrt{V}} \tag{3.2}$$

where V is the accelerating voltage. In a TEM α is very small (~10^{-2} rad), so for a 100 keV electron the maximum resolution is ~2 Å, which is on the order of atoms. The TEM system consist of a high vacuum system, an electron source, a column with a series of electromagnetic lenses to refine, shape, and magnify the electron image, a stage to hold and manipulate the sample, and detectors to capture the image. The electron gun creates a beam of highly energized electrons either through thermionic or field emission (FEG). The condenser lenses take the electrons from the source and transfer them to the sample stage, where all of the electron beam-specimen interactions take place creating various signals which are subsequently magnified for viewing and recording. The objective lens is the most important lens in a TEM because its quality determines the signal quality. In standard TEM mode the condenser lenses are adjusted to irradiate the sample with a parallel beam of electrons, which is essential for good signal contrast (**Fig. 3.5.a**). A scanning transmission electron microscope (STEM) is modified with additional

scanning coils to raster the focused electron beam (e.g. probe) over the sample parallel to the optic axis (**Fig. 3.5.b**). This improves measurement resolution, but because of the highly localized interaction exceptional care must be taken to prevent beam damage influence.

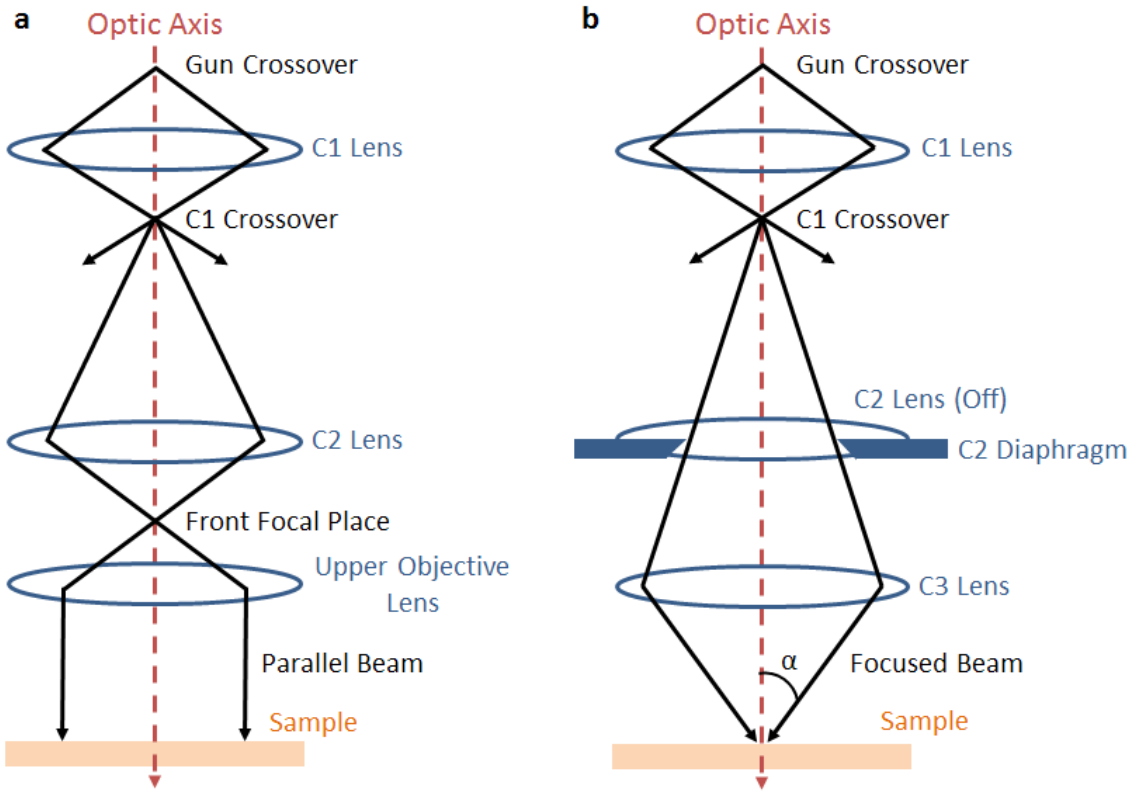

Figure 3.5. Schematic of illumination system in (a) parallel TEM mode and (b) STEM mode.

The core strength of TEM is the ability to obtain both a diffraction pattern and image from the same sample region (**Fig. 3.6.a**). The parallel electrons interact with the sample atoms creating image contrast affected by sample thickness, sample Z-number, crystallinity, and crystal orientation. Additionally, when the back focal plane is focused on the imaging plane, electron diffraction patterns are captured. Together, TEM enables studies of highly localized structural phenomenon.

By taking advantage of the various scattering processes that occur between the incoming electrons and atoms in the material, STEM has the added benefit of simultaneously imaging different structural and chemical information using multiple annular detectors (**Fig. 3.6.b**).[107] The high-angle annular dark-field (HAADF) detector configuration optimizes the electron detection, creating an image with contrast proportional to the atomic number Z (Z contrast).[108] Conversely, the annular bright field (ABF) detector creates an image with contrast inversely proportional to the atomic number, which is ideal for imaging light elements such as oxygen.[109] In addition, energy dispersive X-ray spectroscopy (EDS) and electron energy-loss spectroscopy (EELS) can be used to probe the electronic structures of materials for elemental analysis.[110] As the electron beam interacts with the sample, some electrons will lose kinetic energy via inelastic scattering. EELS characterizes the beam energy loss, which provides compositional and electronic bonding information about the sample.

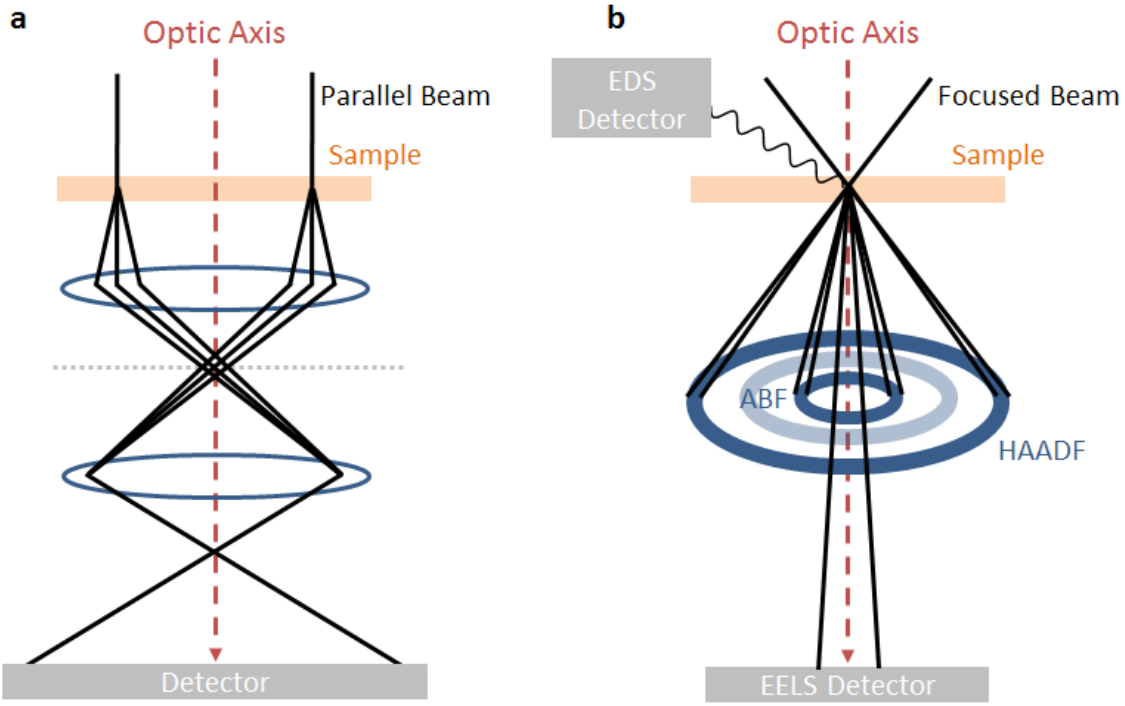

Figure 3.6. Schematic of signal detectors in (a) TEM and (b) STEM mode.

Chapter 4. Development of Amorphous Lithium Lanthanum Titanate Thin Films for Lithium-Ion Solid-State Batteries

Lithium lanthanum titanate (LLTO) is a promising solid state electrolyte for solid state batteries due to its demonstrated high bulk ionic conductivity. However, crystalline LLTO has a relatively low grain boundary conductivity, limiting the overall material conductivity. In this work, we investigate amorphous LLTO (a-LLTO) thin films grown by pulsed laser deposition (PLD). By controlling the background pressure and temperature we are able to optimize the ionic conductivity to $3x10^{-4}$ S/cm and electronic conductivity to $5x10^{-11}$ S/cm. XRD, TEM, and STEM/EELS analysis confirm that the films are amorphous and indicate that oxygen background gas is necessary during the PLD process to decrease the oxygen vacancy concentration, decreasing the electrical conductivity. Amorphous LLTO is deposited onto high voltage $LiNi_{0.5}Mn_{1.5}O_4$ (LNMO) spinel cathode thin films and cycled up to 4.8 V vs. Li showing excellent capacity retention. These results demonstrate that a-LLTO has the potential to be integrated into high voltage thin film batteries.

4.1 Introduction

Next generation lithium-ion batteries will require a broad range of energies to meet the challenges of portable electronic storage from electric vehicles to microelectromechanical systems (MEMS). The cost per Watt-hour of commercial batteries have shown incremental improvement due to better manufacturing design, but drastic increases in energy and power density are needed to satisfy projected demand.[111] Solid-state electrolytes are researched heavily because they have the potential to improve capacity loss, cycle lifetime, operation temperature, and safety. Lithium Phosphorous Oxynitride (LiPON) based thin-film solid-state batteries have excellent cycle life and are currently commercialized.[112, 113] However, LiPON has a relatively

low ionic conductivity ($1x10^{-6}$ S/cm) and other solid electrolytes have demonstrated conductivity several orders of magnitude higher.[17, 114]

Lithium lanthanum titanate (LLTO) is a promising solid-state electrolyte due to its high bulk ionic conductivity (~10^{-3} S/cm) at room temperature, negligible electronic conductivity, and high voltage, atmospheric, and temperature stabilities.[115-117] Extensive fundamental studies have been carried out to demonstrate this high ionic conductivity, elucidate the crystal structure, and determine the mechanism of lithium-ion conduction.[118-121] However, there are fundamental impediments to the implementation of crystalline LLTO into an actual device. One key issue is that crystalline LLTO has a relatively low grain boundary ionic conductivity (<10^{-5} S/cm), lowering the effective material ionic conductivity.[115] In addition, crystalline LLTO is unstable in contact with lithium metal because lithium will easily insert reducing Ti^{4+} to Ti^{3+}, thus increasing electronic conductivity.[122, 123]

Fortunately, amorphous LLTO has not only been shown to overcome these barriers, the lower energy constraints of fabricating amorphous LLTO opens up numerous thin film synthesis techniques. Amorphous LLTO thin films have been synthesized by pulsed laser deposition (PLD), RF magnetron sputtering, e-beam evaporation, atomic layer deposition, chemical solution deposition and sol-gel synthesis.[124-133] Furusawa et al. demonstrated amorphous LLTO thin films deposited via PLD with higher ionic conductivity ($8.98x10^{-4}$ S/cm) than polycrystalline thin films.[124] They suggest that this is likely due to the lack of grain boundaries and open disordered structure. However, these films also suffer from a high electronic conductivity of $4.0x10^{-5}$ S/cm. Furthermore, Ahn and Yoon deposited amorphous LLTO thin films by PLD with lower ionic conductivity ($2.0x10^{-5}$ S/cm) and found that there was no electronic conductivity degradation when in contact with lithium metal.[128] Zheng et al. also demonstrated that

amorphous LLTO powders by sol-gel synthesis remain ionically conductive in contact with lithium metal even though it undergoes the same lithium insertion and Ti^{4+} to Ti^{3+} reduction.[117] They hypothesize that this phenomenon is due to local atomic disorder in the amorphous case that localize electronic states.

Lastly, amorphous LLTO thin films have a large voltage stability window, which opens a pathway for high-voltage cathode materials, such as $LiNi_{0.5}Mn_{1.5}O_4$ (LNMO) spinel. High-voltage cathodes have the potential to greatly improve the energy density of lithium-ion batteries, but current liquid electrolytes face stability issues at high voltage due to strong oxidation reactions.[134] With proper optimization, amorphous LLTO is a high ion conductive solid-state electrolyte with the potential to enable high voltage batteries with lithium metal anode.

Therefore, in this work, we investigate amorphous LLTO thin films grown by PLD for high voltage thin film batteries. By controlling the background pressure and temperature we are able to grow films with high ionic conductivity ($3x10^{-4}$ S/cm) several orders of magnitude higher than its electronic conductivity. Grazing incidence X-ray diffraction (GIXRD), transmission electron microscopy (TEM), and electron energy loss spectroscopy (EELS) analysis confirms that the films are amorphous and indicates that sufficient oxygen background gas is necessary during PLD to minimize oxygen vacancy concentration, which lowers the electrical conductivity. Amorphous LLTO is deposited onto high voltage $LiNi_{0.5}Mn_{1.5}O_4$ (LNMO) spinel thin films and cycled up to 4.8 V vs. Li showing excellent capacity retention. These results demonstrate that a-LLTO is stable across the full voltage range and has minimal adverse interfacial reactions with LNMO.

4.2 Experimental

4.2.1. LLTO Synthesis.

The $Li_{0.5}La_{0.5}TiO_3$ (LLTO) target was synthesized via solid state reaction consistent with previous reports.[124, 128, 135] Stoichiometric amounts of Li_2CO_3 (Sigma Aldrich, 99.8%), La_2O_3 (Sigma Aldrich, 99.9 %), and TiO_2 (Fisher Scientific, 95.0%) powders were ground with an agate mortar and pestle and calcined in an alumina crucible in a box furnace under ambient atmosphere. Samples were heated to 1200 °C, held for 6 hours, and then cooled back to room temperature at a ramp rate of 5 °C/min. The powder was ground again and pressed in a 1-1/8 dye press with 10 tons of pressure for 5 minutes. The formed pellet was then sintered at 1300 °C for 5 hours, using a ramp rate of 5 °C/min.

X-ray diffraction (XRD) analysis of the resulting pellet was collected using a Rigaku SmartLab X-ray diffractometer with Cu Kα source operating at 30 kV and 15 mA with a step size of 0.05° at 1°/min, scanning over 10–80°. Reitveld refinement was used to determine the crystalline phases. Both sides of the LLTO pellet were coated with 100 nm of Au using a Denton Discovery 18 Sputtering System and a Biologic SP-200 Potentiostat was used to conduct electrochemical impedance spectroscopy (EIS). The frequency range was 7 MHz to 100 mHz with an amplitude of 10 mV and data was fit with a complex non-linear least square fitting method. The metal contacts were subsequently sanded off and the polished pellet was used for pulsed laser deposition (PLD).

4.2.2. Pulsed Laser Deposition of LLTO.

Thin films were grown using an Excel Instruments PLD-STD-12 chamber and 248 nm KrF Lambda Physik LPX-Pro 210 excimer laser. Before deposition the chamber was pumped

down to a baseline pressure of < $2.0x10^{-6}$ Torr. Amorphous LLTO thin films were deposited at a range of pressures and temperatures, with a constant ~2 J/cm^2 energy density and 4 Hz laser frequency. Amorphous LLTO was deposited on 2 different substrates for various analyses. For interdigitated samples, 2 electronically isolated interdigitated contact pads were sputtered on polished SiO_2/Si similar to Furusawa et al.[124] The interdigitated contact finger widths were ~120 μm with ~80 μm spacing and the films were ~300 nm thick. Resulting measurements correspond to conduction parallel to the thin film surface. For vertical samples, ~1.2 μm of amorphous LLTO was deposited on Pt coated SiO_2/Si. Another layer of Pt was deposited via DC sputtering to fabricate Pt/a-LLTO/Pt symmetric cells in the architecture necessary to eventually fabricate a solid-state battery device.

A Biologic SP-200 Potentiostat was again used to measure the electronic conductivity by DC polarization and the ionic conductivity by electrochemical impedance spectroscopy (EIS). The frequency range was 3 MHz to 100 mHz with an amplitude of 10 mV and data fitted with a complex non-linear least square fitting method. For low temperature EIS measurements the samples were placed in an Espec temperature chamber.

4.2.3. Electrochemical Testing.

The $LiNi_{0.5}Mn_{1.5}O_4$ (LNMO) target was synthesized by solid state reaction previously reported.[70] MnO_2 (Sigma Aldrich, 99.99%), NiO (Sigma Aldrich, 99.99%), and LiOH (Sigma Aldrich, 98.0%) powders were mixed, pressed in a 1-1/8 dye press with 10 tons of pressure for 10 minutes, and calcined in a box furnace under ambient atmosphere at 750 °C for 24 hours with a ramp rate of 3 °C/min. Afterwards, the powder was ball milled for 5 hours, pressed, and then sintered at 900 °C for 2 hours using a ramp rate of 3 °C/min. The resulting pellet was sanded and

used as a target for pulsed laser deposition (PLD). The LNMO target had excess lithium (1.3x Li) to compensate for Li loss during PLD. LNMO thin films were deposited on Pt-coated Al_2O_3 substrates at 600 °C, 0.2 Torr O_2 partial pressure, ~2 J/cm^2 energy density, and laser pulse frequency of 10 Hz for 40 minutes.

LNMO and LNMO/a-LLTO thin film electrodes were assembled into SS316L 2032 coin cells in a glovebox purged with high purity argon (99.9995%) and maintained with oxygen and water vapor levels at or less than 5 ppm. The cells consisted of Celgard (C480) polyprolylene separator (Celgard Inc., USA), 1 M $LiPF_6$ electrolyte solutions (battery grade, BASF) in ethylene carbonate/ethyl methyl carbonate (EC:DEC) (1:1 wt), and lithium metal as the counter electrode. An Arbin battery cycler was used to galvanostatically cycle the cells between 3.5 and 4.8 V. X-ray photoelectron spectroscopy (XPS) was performed using a Kratos AXIS Supra with Al Kα anode source operated at 15 kV. The chamber pressure was <10-8 Torr during all measurement sand spectra were calibrated using the hydrocarbon C1s peak at 284.8 eV. Samples were transferred from glovebox to XPS chamber via an air-free vacuum transfer system.

4.2.4. Transmission electron microscopy (TEM).

Electron-transparent cross-sectional lamellas were prepared using a FEI Helios NanoLab Dualbeam. The maximum ion beam current used for a regular cross sections is ~3 nA while the pixel dwell time was limited to 100 ns. The samples were extracted out of the thin film following standard lift out procedures and thinned down to ~80 nm using 0.3 nA cleaning cross sections. STEM-EELS images and spectrums were collected on a JEOL 2100F at 200 kV, located at the Center for Functional Nanomaterials at Brookhaven National Laboratory. For all spectra, the beam density measured by the fluorescent screen was 2.4 pA cm^{-2} and the beam diameter was

focused to approximately 0.2 nm. The energy resolution of the electron energy loss spectra was approximately 1 eV. For high-loss spectra, a 20 s pixel dwell time, and 0.2 eV per channel dispersion was used. Selected area electron diffraction (SAED) was collected with the smallest objective aperture (~150 nm in diameter). For the deposition temperature dependent study transmission electron microscopy (TEM) bright field and diffraction data were acquired using an FEI Tecnai G2 Sphera TEM equipped with a LaB6 source operating at 200 keV. Difftools, a Digital Micrography add-on made by Dave Mitchell, was used to calculate the integrated radial intensity pattern. A power law curve was used to subtract the background.

4.3 Results and Discussion

4.3.1 LLTO Target Characteristics

XRD of the sintered ceramic pellet confirms that the target is highly crystalline and consists of the cubic perovskite phase mixed with the tetragonal phase (**Fig. 4.1.a**). A two phase fit of the cubic phase (space group $Pm\bar{3}m$) and the tetragonal phase (space group $P4/mmm$) was performed resulting in a conventional Rietveld factor (R_{wp}) of 7.99. Room temperature EIS measurement using Au blocking electrodes reveals one high frequency semi-circle, one low frequency semi-circle, and a capacitive tail (**Fig. 4.1.b**). This is in agreement with previous reports designating the high frequency intercept as the lattice conductivity (R_L) and the low frequency intercept as the grain boundary conductivity (R_{GB}). The R_L and R_{GB} values were determined using the equivalent circuit displayed in the inset and the respective ionic conductivities were determined using

$$\sigma = \frac{d}{A\,R} \tag{4.1}$$

where d is the thickness of the sample, A is sample area, and R is the resistance. The pellet has a lattice conductivity of 8.0×10^{-4} S/cm and grain boundary conductivity of 2.5×10^{-5} S/cm, which is consistent with reported values.[119, 135]

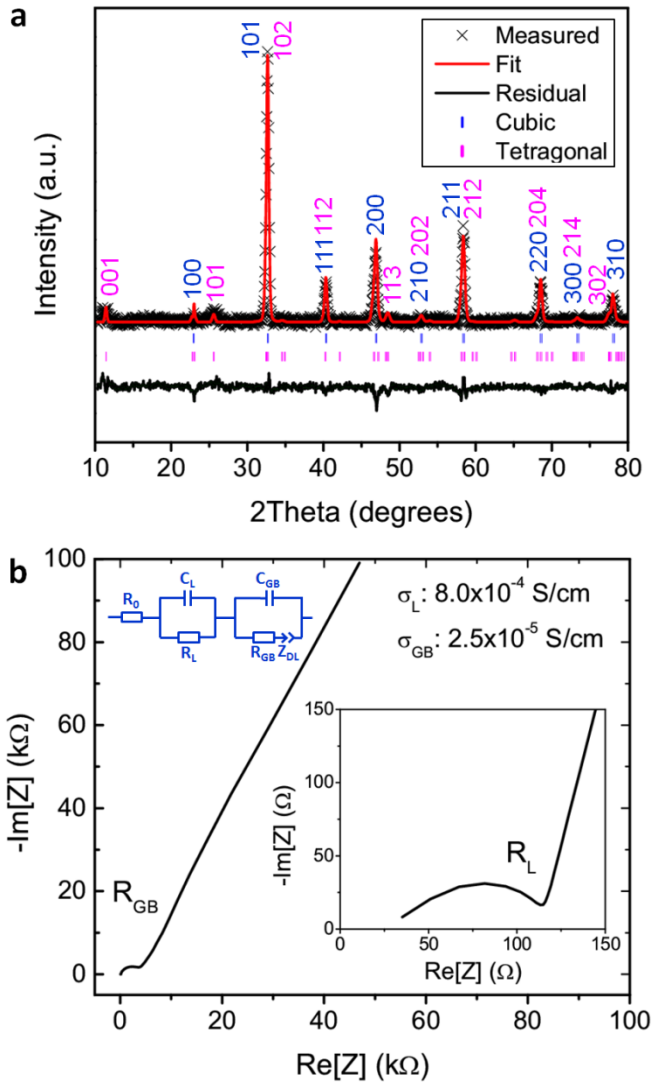

Figure 4.1. (a) XRD, Rietveld refinement, and (b) EIS of crystalline LLTO pellet

4.3.2. Deposition Pressure Dependence

There is discrepancy between previous reports of optimal amorphous LLTO PLD deposition conditions. Furusawa et al. deposited films in vacuum ($5x10^{-6}$ Torr), while Ahn and Yoon deposited at 0.1 Torr O_2 partial pressure (**Table 4.1**).[124, 128] Interestingly, Furusawa et al. produced films with higher ionic conductivity ($8.75x10^{-4}$ S/cm), but also significantly higher electronic conductivity ($4.0x10^{-5}$ S/cm). We deposited Pt/a-LLTO/Pt vertical films at 400 °C, 4 Hz, and ~2 J/cm^2 at various pressures: vacuum (~$1x10^{-5}$ Torr), 0.03 Torr, and 0.2 Torr O_2 partial pressure. DC polarization tests confirm that with higher oxygen pressure the electronic conductivity decreases (**Fig. 4.2.a**). In fact, for the vacuum and 0.03 Torr sample there is negligible polarization due to the high electronic conductivity. The vacuum film is black, also noted by Furusawa et al., while the 0.03 and 0.2 Torr O_2 films are transparent.[124] All samples are dense films with no pinholes, although there appears to be some vertical texturing in the 0.2 Torr sample (**Fig. 4.2.b-d**).

Table 4.1. Summary of previous reports of amorphous LLTO films grown by PLD

	Furusawa et al.[124]	Ahn and Yoon[128]
Pressure	$5x10^{-6}$ Torr	0.1 Torr
Temperature	25 °C	100-600 °C
Frequency	10 Hz	4 Hz
Energy	180 mJ/pulse	2 J/cm^2
Ionic Conductivity	$8.8x10^{-4}$ S/cm	$2.0x10^{-5}$ S/cm
Electronic Conductivity	$4.0x10^{-5}$ S/cm	$3.5x10^{-11}$ S/cm

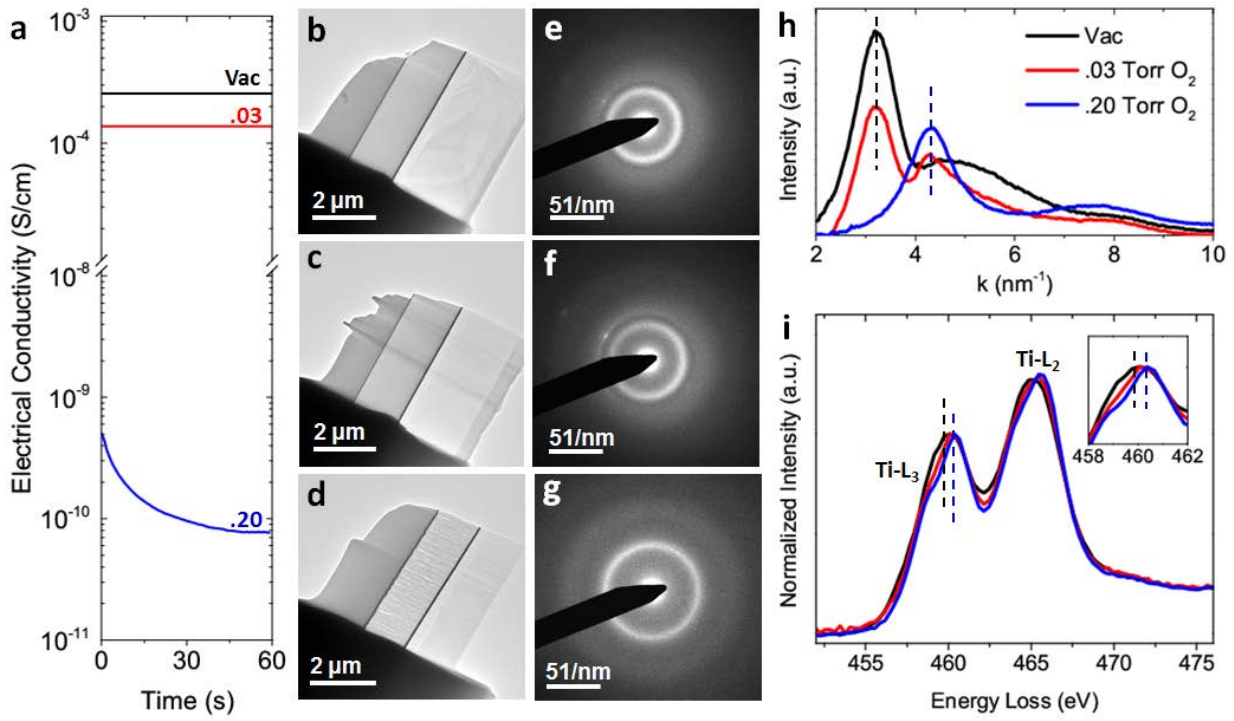

Figure 4.2. (a) DC conductivity of a-LLTO thin films at room temperature. TEM bright field image and SAED of samples prepared in (b, e) vacuum, (c, f) .03 Torr O_2, and (d, g) .2 Torr O_2 chamber pressure. Corresponding (h) intensity profile and (i) normalized Ti-L edge spectra.

STEM-EELS analysis was performed to probe the local bonding structure. Selected area electron diffraction (SAED) shows that while all three samples are amorphous, there are variations in the radial distance of the diffuse rings, indicating shifts in average bond length (**Fig. 4.2.e-g**). Plotting the radial intensity we see that there is a ~1.1 nm^{-1} peak shift between the vacuum sample and 0.2 Torr O_2 sample. Also of note, the 0.03 Torr O_2 sample has two diffuse rings aligning with both the vacuum and 0.2 Torr O_2 peak (**Fig. 4.2.h**). In addition, EELS analysis was performed and the Ti-$L_{2,3}$ edge reveals that for the vacuum sample there is a ~0.5 eV chemical shift and intensity reduction in the Ti-L_2 edge (**Fig. 4.2.i**). Gao et al. discovered a similar phenomenon in Ti-$L_{2,3}$ edge when comparing the La-poor and La-rich regions of crystalline LLTO and attributed the phenomenon to Ti^{4+} cations reducing to Ti^{3+} creating oxygen

vacancies.[120] It is reasonable to believe that for LLTO deposited in lower pressure, there is greater oxygen loss resulting in oxygen vacancies. These oxygen-deficient domains could result in regions of larger lattice spacing from repulsion of charged atoms, and this excess Ti^{3+} would also create electron conduction pathways increasing the electronic conductivity. Thus, high oxygen pressure is necessary during pulsed laser deposition to minimize oxygen vacancy formation reducing the electronic conductivity.

4.3.3. Deposition Temperature Dependence.

There is also inconsistency in previous reports on the optimal deposition temperature (**Table 4.1**). Crystalline LLTO thin films are deposited at 800 °C and LLTO will remain amorphous as long as the deposition temperature is < 700 °C.[136] We deposited a-LLTO on interdigitated contacts at 0.2 Torr oxygen, 4 Hz, and ~2 J /cm^2 at various temperatures expanding the full range from Furusawa et al. and Ahn and Yoon.[124, 128] The Nyquist plots show a single semicircle and dielectric capacitance tail (**Fig. 4.3.a**). The data was fit using the equivalent circuit in **Figure 4.3.b**, which is consistent with the models used for lithium phosphorous oxynitride (LiPON) thin film electrolytes.[137] Since the films are amorphous, there are no separate lattice and grain boundary parameters, but two RC circuits are needed to fit the data. This is likely due to sample roughness and/or contact interfacial phenomenon. Plotting the ionic conductivity across temperature we see that our films are on par with previous literature (**Fig. 4.2.c**). Films deposited at 200 °C and 400 °C showed the highest ionic conductivity of 3.0×10^{-4} S/cm. Additionally, at high temperature our films show a similar trend to Ahn and Yoon, where the samples decline in ionic conductivity above 400 °C.[128]

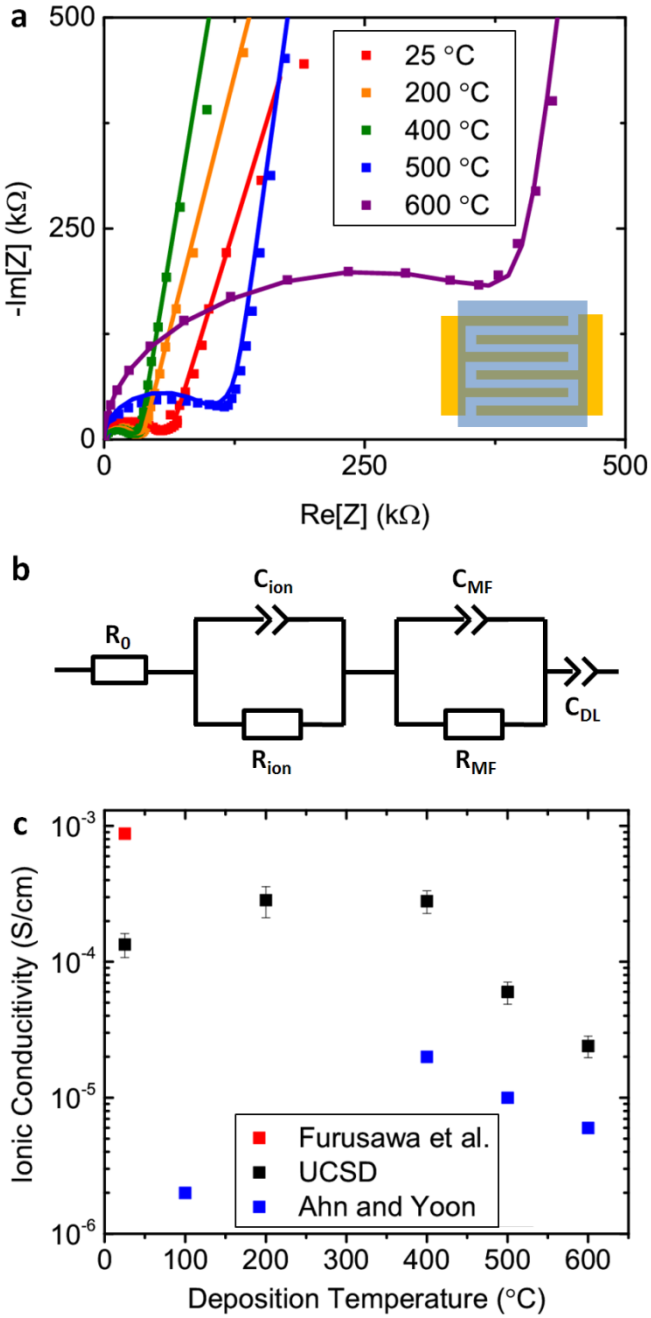

Figure 4.3. (a) Nyquist plot of a-LLTO thin film samples deposited at various temperatures with interdigitated contacts. (b) Equivalent circuit corresponding to Nyquist plot. (c) Variation in ionic conductivity as a function of deposition temperature.

Grazing angle XRD indicates that films deposited up to 600 °C remain amorphous, with only peaks from the platinum coated substrate (**Fig. 4.4.a**). However, SAED of a-LLTO deposited at 600 °C features both an amorphous diffuse ring and diffuse diffraction spots (**Fig. 4.4.c.**). The sample is still overwhelmingly amorphous, and these peaks cannot be indexed to a particular crystal structure, but it is likely that at higher temperatures LLTO nanocrystals begin to form. Any crystallization will be detrimental to ionic conductivity due to grain boundary diffusion. Crystalline LLTO thin films deposited by PLD have been shown to be up to an order of magnitude lower in ionic conductivity than amorphous. Thus, for good ionic conductivity we must keep the deposition temperature ≤400 °C.

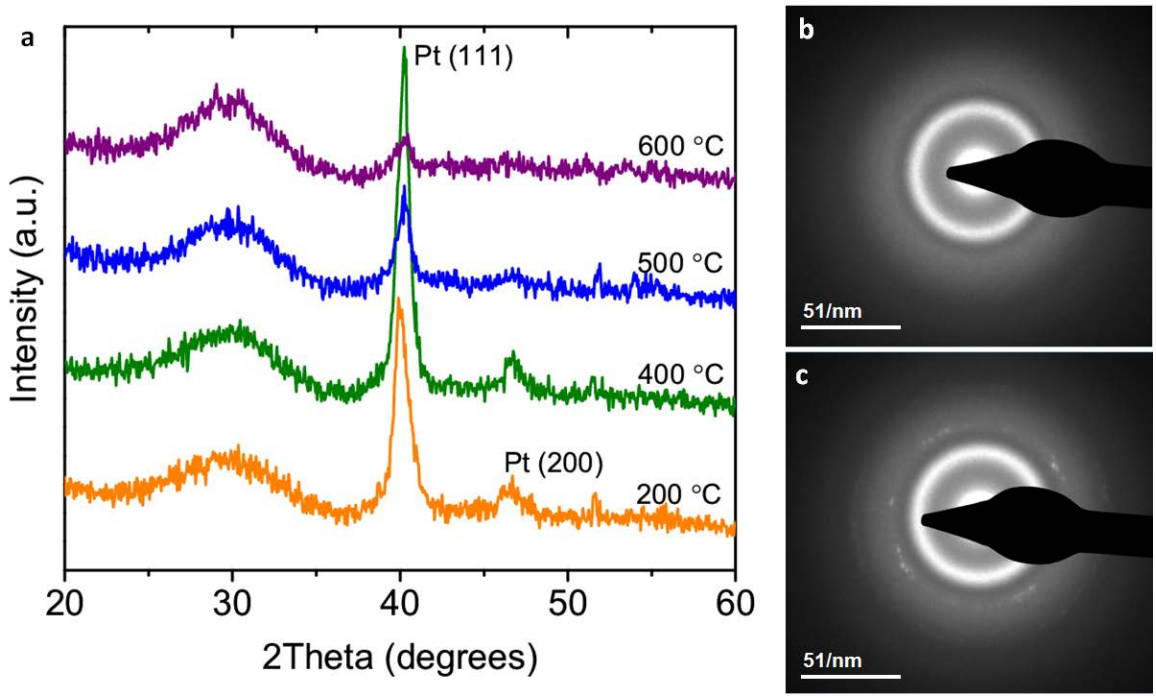

Figure 4.4. (a) Grazing angle XRD of a-LLTO thin films deposited at various temperatures. SAED of samples deposited at (b) 400 °C and (c) 600 °C.

The temperature series conditions were also deposited in the Pt/LLTO/Pt vertical configuration to confirm its compatibility with integration into a thin film device. Given the

geometrical constraints and high ionic conductivity the semicircle was too small to detect at room temperature. Instead there is only the capacitive tail. To obtain an accurate calculation of ionic conductivity the samples were cooled to various temperatures. At lower temperatures the ionic conductivity decreases, increasing the resistance and signal (**Fig. 4.5.a**). From the Arrhenius plot we are able to extrapolate activation energy on par with previous experimental and computational results and a room temperature ionic conductivity, which was in agreement with the interdigitated contact values (**Fig. 4.5.b**).[124-126, 138] The electronic and ionic conductivity is summarized in **Figure 4.6**. Similar to Furusawa et al. room temperature PLD resulted in a thin film with high ionic conductivity, but also high electronic conductivity.[124] The electronic conductivity decreased with higher temperature, probably correlating with greater oxygen incorporation kinetics. For a good solid-state electrolyte there needs to be several orders of magnitudes between the high ionic and low electronic conductivity. Therefore, the optimal deposition temperature should be at 400 °C.

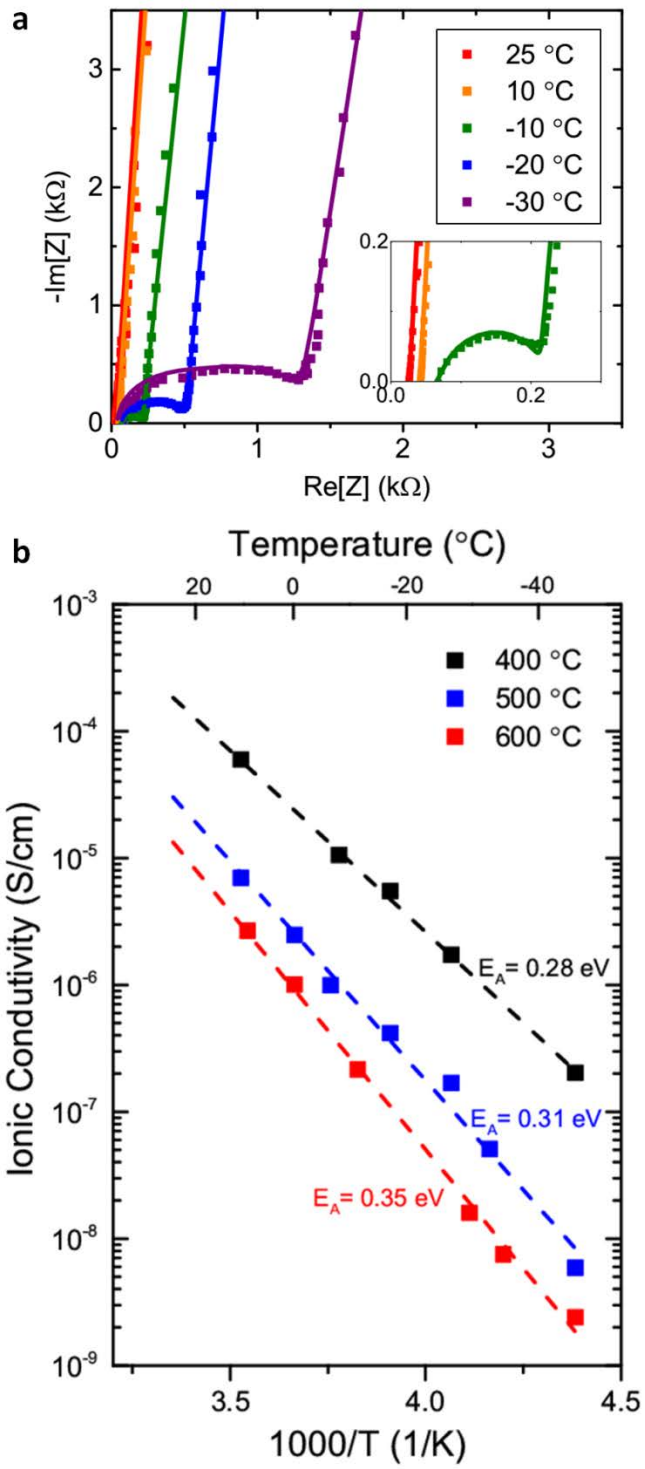

Figure 4.5. (a) Nyquist plot at various temperatures of a-LLTO thin film sample deposited at 400 °C with vertical contacts. (b) Arrhenius plot of various deposition temperatures.

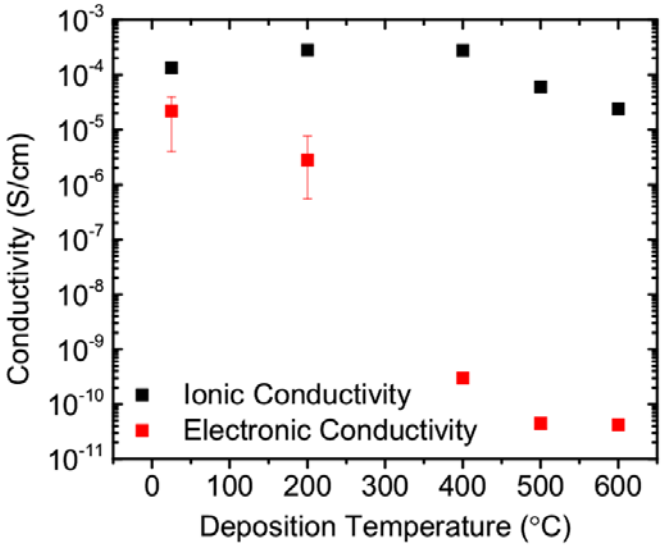

Figure 4.6. Ionic and electronic conductivity at various temperatures.

4.3.4. Electrochemistry. The optimized a-LLTO deposition conditions (0.2 Torr O_2, 400 °C, ~2 J/cm^2, 4 Hz) was used to coat a $LiNi_{0.5}Mn_{1.5}O_4$ (LNMO) electrode, thus referred to as the LNMO/a-LLTO electrode. The cycling performance of the LNMO and LNMO/a-LLTO electrode are in **Figure 4.7**. The a-LLTO deposition does not alter the LNMO intercalation chemistry as both cells show the characteristic voltage profile for LNMO, exhibiting the Ni^{2+}/Ni^{4+} (4.7 V) and Mn^{3+}/Mn^{4+} (4.0 V) redox couples. For a pure phase LNMO film, we shouldn't observe this 4 V Mn^{3+}/Mn^{4+} redox signal, but Mn^{3+} ions have been previously found in composite and PLD electrodes.[61, 139] This is potentially due to non-stoichiometric oxygen or nickel transfer during PLD. The LNMO/a-LLTO cell exhibits superior reversible capacity stability with 98% discharge capacity retention after 50 cycles (**Fig. 4.7.b**). This corresponds to a 0.036% capacity fade per cycle. However, the coulombic efficiency is relatively low for both cells at 96%. This charge loss is due to electrochemical decomposition of the liquid electrolyte at extremely high voltage such as 4.8V during each cycle. And going to a full solid-state device would overcome such effects.

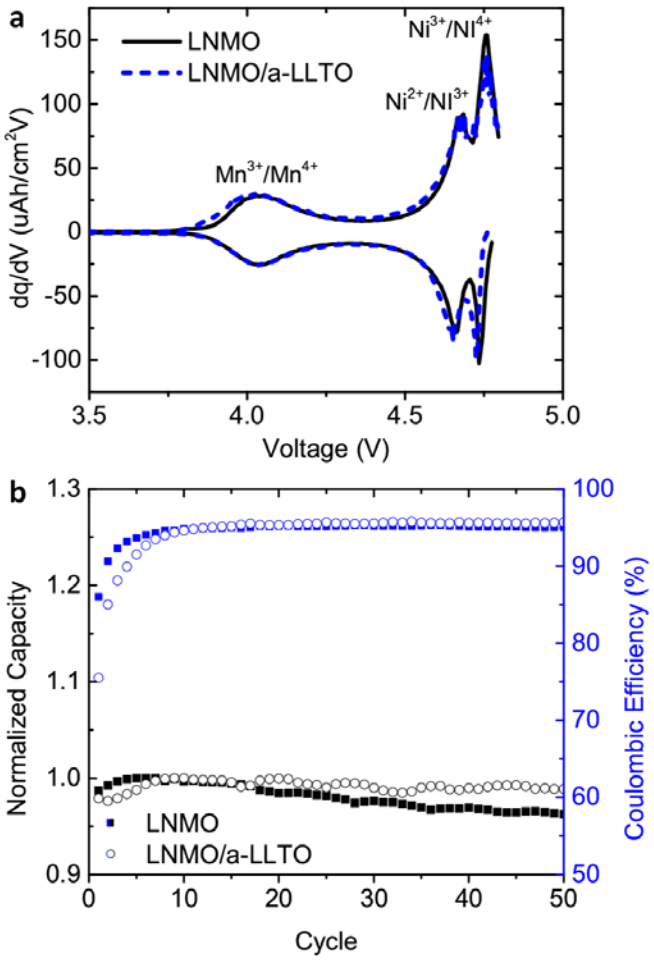

Figure 4.7. (a) Cycling profile and (b) performance of 300 nm $LiNi_{0.5}Mn_{1.5}O_4$ and 300 nm $LiNi_{0.5}Mn_{1.5}O_4$ with 500 nm a-LLTO coating.

For the LNMO/a-LLTO electrode there is no significant change in the voltage profile and the cell maintains comparable discharge capacity for a variety of cycling rates (**Fig. 4.8).** The interfacial compatibility between the LNMO and a-LLTO is crucial for cell performance and previous attempts to pair PLD a-LLTO with $LiCoO_2$ (LCO) resulted in extreme performance deterioration from a highly resistive interfacial layer.[128] The excellent capacity retention is indicative of minimal formation of an unfavorable interfacial LNMO/a-LLTO reaction, but this is further investigated with EIS (**Fig. 4.9**). XPS analysis confirms that the a-LLTO remains on

the LNMO electrode surface with no dissolution during cycling (**Fig. 4.10**). Thus, we have shown that a-LLTO has good rate performance and is electrochemically compatible with LNMO for future high voltage thin film battery devices.

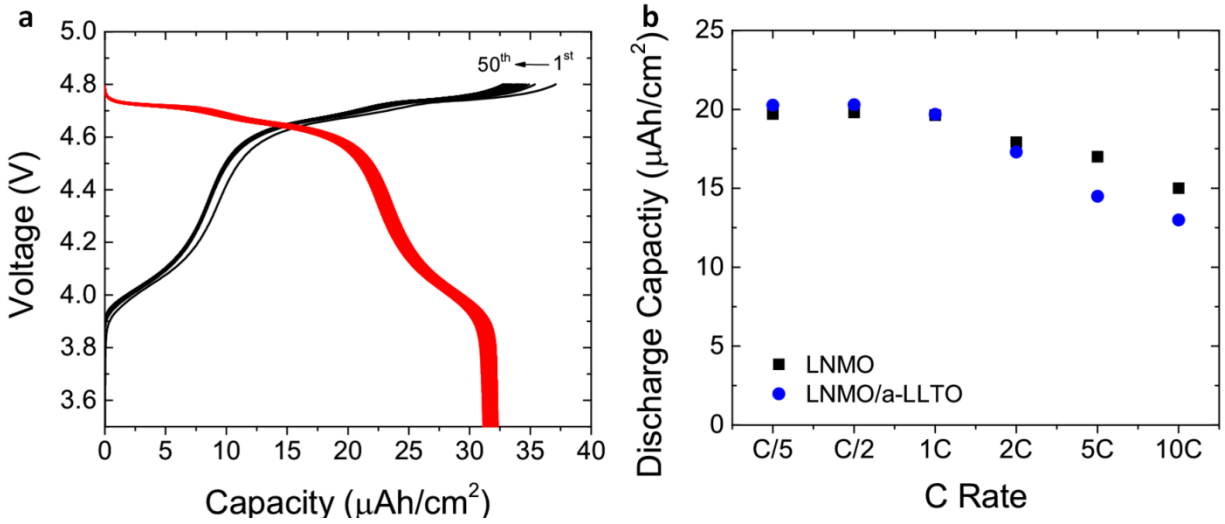

Figure 4.8. (a) Voltage profile of LNMO/a-LLTO sample at 1C rate. (b) Discharge rate performance of batteries at various rates.

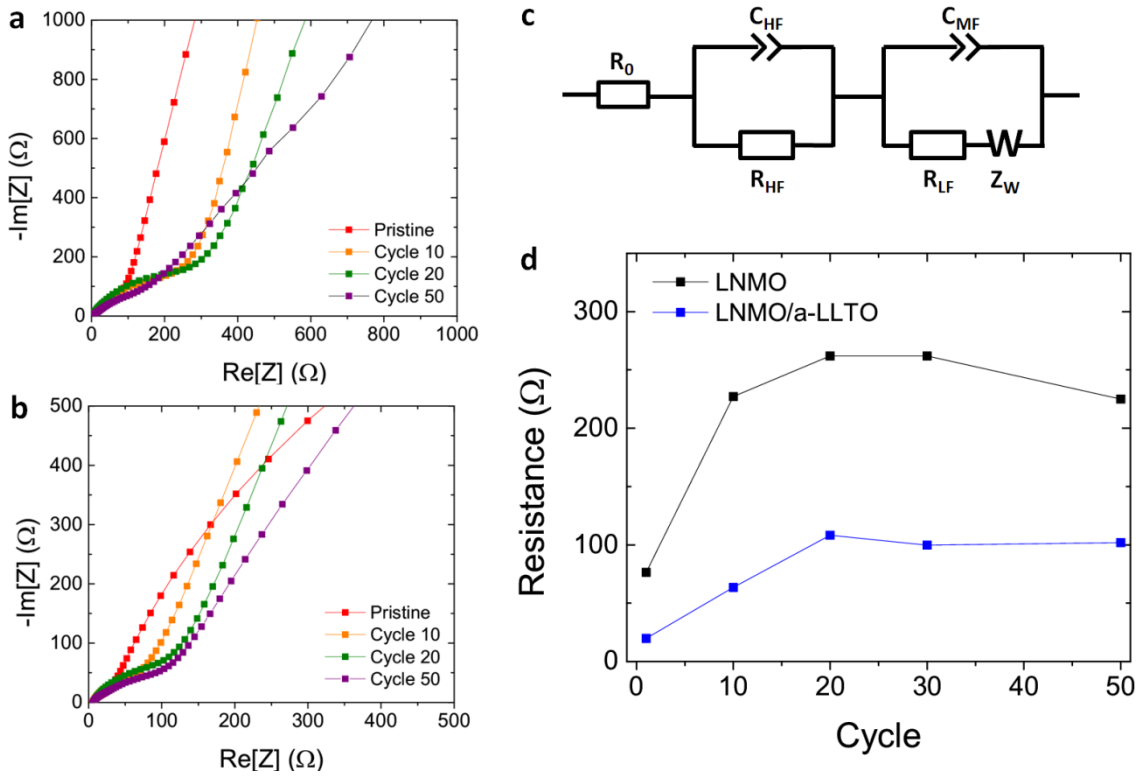

Figure 4.9. Nyquist plot of (a) LNMO and (b) LNMO/a-LLTO obtained at discharged state. Fit with equivalent circuit (c). C_{HF} and R_{HF} represent a combination of interfacial resistance and electrolyte resistance. R_{LF}, C_{LF}, and Z_W represent the charge transfer resistance, double layer capacitance, and diffusion Warburg elements (d) Calculated cell resistance at different cycles.

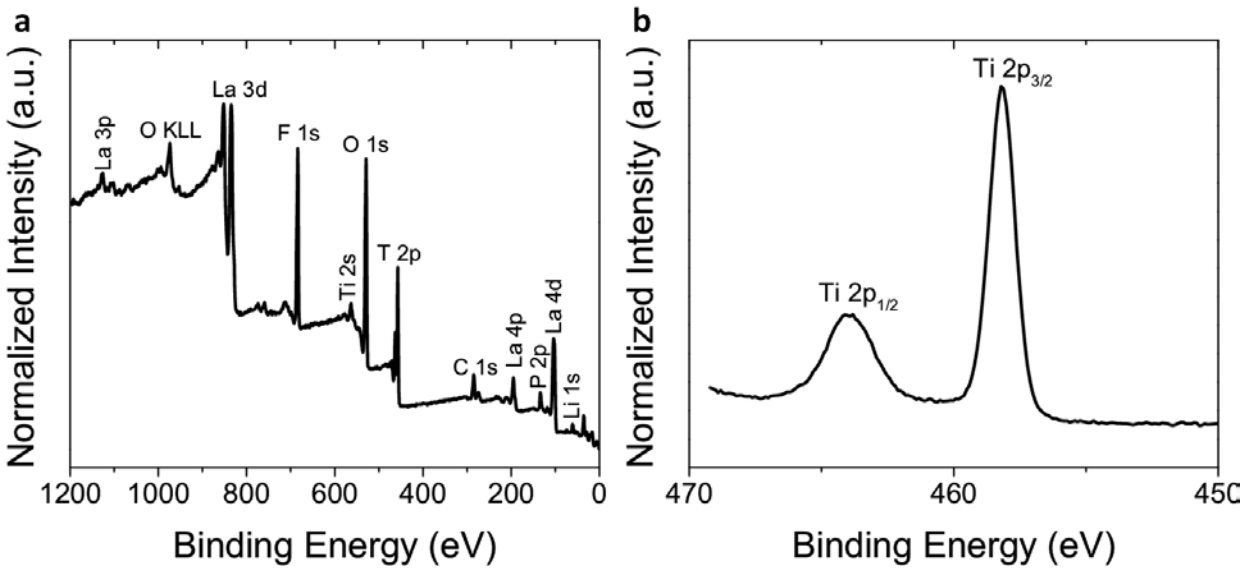

Figure 4.10. XPS (a) survey scan and (b) Ti 2p region scan of LNMO/a-LLTO after 50 cycles. a-LLTO remains on the LNMO surface as there are clear Ti 2p peaks and no Mn 2p (~641.4 eV) peaks.

4.4 Conclusion

In this work, we prepared amorphous LLTO thin films by pulsed laser deposition for use in high voltage thin film lithium-ion batteries. Various deposition conditions were optimized to maximize ionic conductivity while maintaining sufficiently low electronic conductivity to function as an effective solid-state electrolyte. Our ~1.2 μm thick a-LLTO film grown at 0.2 Torr O_2, 400 °C, ~2 J/cm^2, and 4 Hz exhibits an ionic conductivity of 3.0×10^{-4} S/cm and electronic conductivity of 3.0×10^{-10} S/cm. This condition is used to fabricate a LNMO/a-LLTO half-cell, which maintained 98% capacity retention after 50 cycles. There was no significant degradation in cycling performance indicative of excellent compatibility between LNMO electrode and a-LLTO electrolyte. Future work will be done to further examine the LNMO/a-LLTO interfacial stability and develop a high voltage LNMO/a-LLTO based thin film solid-state battery.

This chapter, in full, is a reprint of the material “Amorphous Lithium Lanthanum Titanate For Solid-State Microbatteries” as it appears in the Journal of the Electrochemical Society, J.Z. Lee, Z. Wang, H.L. Xin, T.A. Wynn, and Y.S Meng, 2017, 164, A6268. The dissertation author was the primary investigator and first author of this paper. All the experiments and writing were done by the author expect for the x-ray diffraction and STEM-EELS data collection.

Chapter 5. Air-Free Mechanical Testing of LiPON Thin Film Solid-State Electrolyte

Lithium phosphorus oxynitride (LIPON) exhibits remarkable stability as a solid-state thin film electrolyte in all-solid-state batteries that include lithium metal electrodes.[91, 140] LIPON has been reported previously as a mechanically stiff material with Young's elastic moduli similar to that of silica glass and aluminum (~70 GPa).[141, 142] Thus, one rationale for LIPON performance as a solid electrolyte is that this material may resist lithium (Li) dendrite growth upon repeated battery charging cycles through such resistance to reversible or elastic deformation. However, prior mechanical characterization of this material was conducted in ambient humidity environments. comprising water vapor, which is known to also alter surface chemistry and electrolyte performance of LIPON.[143] For that reason, this material is processed and packaged to minimize such ambient humidity exposure in solid state battery applications. Here, using nanoindentation in controlled physical environments[144] that reflect the minimized exposure to ambient humidity for solid electrolyte use in solid state batteries, we show that this material exhibits mechanical stiffness that is lower than reported previously by two orders of magnitude. This finding of significantly reduced mechanical stiffness prior to exposure to ambient humidity illustrates the importance of material characterization under environments consistent with battery assembly and operation.[144, 145] Further, given the robust performance of LIPON as an electrolyte in thin film batteries[146], this finding challenges the concept that high material stiffness is a key parameter required of LIPON solid electrolytes to block Li dendrite growth.[147]

5.1 Introduction

Lithium-ion batteries (LIBs) are used for a wide range of energy storage technologies[148] that leverage high energy and power densities, including for portable electronics, electrified

vehicles, and utility storage for intermittent (solar and wind) power sources.[149, 150] While the organic liquid electrolytes typically employed by LIBs offer fast Li ion conduction and electrochemical stability up to ~4.5 V,[151] flammability of liquid electrolytes under conditions of Li dendrite-induced electrical shorting has led to safety concerns.[152] All solid-state batteries (SSBs) with solid-state electrolytes (SSEs) have emerged as non-flammable, safer alternatives that may also enable the use of electrodes with higher energy density.[113, 153-155] In particular, thin film SSBs such as those using LIPON SSE, high voltage cathodes, and Li metal anodes have exhibited long cycle life and stability under repeated electrochemical cycling.[113, 146]

While electrochemical behavior of LiPON and other candidate SSEs is studied more intensively, Mechanical performance of SSEs is critical to reversible cycling, as the associated chemomechanical strains in the SSEs, adjacent electrodes, and electrode-electrolyte interfaces may lead to fracture, interfacial delamination, and capacity fade.[156, 157] Previous theoretical work by Monroe and Newman suggested that polymer SSEs with higher Young's modulus may suppress Li dendrite growth more effectively, and established that the SSE shear elastic modulus should be greater than twice that of Li metal to prevent Li dendrite penetration. Although others have attempted to apply this criterion generally to SSEs, many state-of-the-art sulfide and oxide SSEs with elastic moduli satisfying the Monroe-Newman criterion still suffer from electrical shorting that exhausts useful lifetime of such SSB designs. Several such SSEs also exhibit low fracture toughness of $\leq$1 MPa-m$^{1/2}$,[144, 158, 159] suggesting that fracture mechanisms may play a role in device failure, e.g., via infiltration of Li into SSE cracks prior to electrical shorting.[160] Thus, there is growing evidence that other physical and mechanical properties of materials within a SSB also contribute significantly or even chiefly to electrical shorting, though initial

considerations emphasized the role of putatively high SSE Young's moduli that would resist Li dendrite penetration via elastic deflection of the solid electrolyte.

In the context of these emerging explanations for material properties that govern battery performance, most current studies attribute stable cycling of SSBs comprising thin film LIPON electrolyte to the higher mechanical stiffness or Young's elastic modulus of this material as compared with Li metal.[113, 161-163] The Young's modulus *E* of LIPON, reported in multiple thorough studies employing nanoindentation and acoustic measurements, is in the range of *E* = 67-80 GPa.[141, 142] This magnitude of elastic modulus is approximate to that of silica glass or aluminum, and exceeds that of Li metal electrodes by more than an order of magnitude (*E* = 2 - 5 GPa).[164] However, LIPON is also known to be highly sensitive to water vapor, with ionic conductivity reduced dramatically after minutes of exposure to ambient humidity, and in practice requires an inert atmosphere for handling and electrochemical cell assembly.[143] LIPON is primarily sensitive to moisture, but has little to no sensitivity to oxygen or dry air.[165-169] Despite this known environmental sensitivity, all previously reported studies of LIPON mechanical behavior have been conducted in ambient humidity. As a result, it has remained unconfirmed whether those measured mechanical properties accurately represented those exhibited by this material in an environment representative of glove-box assembled and operating solid-state batteries. Thus, here we measured elastic and plastic properties of LIPON before and after exposure to ambient humidity, using our established approaches for instrumented nanoindentation under controlled physical environments.[144] We identified an increase in *E* by more than one order of magnitude after exposure of LIPON to ambient humidity, indicating that LIPON is of much lower mechanical stiffness under solid state battery-assembled conditions than would be inferred from prior reports.

5.2. Experimental

5.2.1. LiPON Deposition

LiPON thin films were deposited on SiO_2/Si (MTI) and Al_2O_3 ceramic (MTI) substrates by RF sputtering of a 2" Li_3PO_4 target (Plasmaterials) at 50W in 15 mTorr N_2. The base pressure of the chamber was 1.2 x 10^{-6} Torr. Pristine samples were transferred directly into a glovebox purged with high purity argon (99.9995%) and maintained with oxygen and water vapor levels at or less than 5 ppm. Air exposed samples were left out in ambient humidity for 24 hours before stored in the glovebox until further testing.

5.2.2. Electrochemical and Chemical Characerization

Electrochemical Characterization. Si/SiO_2/Pt/LiPON (pristine and air-exposed)/Pt symmetric cells were fabricated and a Biologic SP-200 Potentiostat was used to conduct electrochemical impedance spectroscopy (EIS). The frequency range was 3 MHz to 100 mHz with an amplitude of 10 mV and data fitted with a complex non-linear least square fitting method.

X-ray Photoelectron Spectroscopy (XPS). XPS was conducted using a Kratos AXIS Supra with the Al anode source operated at 15 kV with a 500 mm Rowland circle monochromator. The chamber pressure was <10^{-8} Torr during all measurements. High resolution spectra were calibrated using the hydrocarbon C1s peak at 284.8 eV. Fitting was conducted using CasaXPS software using a Shirley-type background. Samples were air-free transferred to the XPS chamber from a glove box via vacuum transfer.

Scanning Transmission Electron Microscopy (STEM). Electron-transparent cross-sectional lamellas were prepared using a FEI Helios NanoLab Dualbeam. The maximum ion beam current used to prepare cross sections was ~3 nA while the pixel dwell time was limited to 100 ns. The samples were extracted out of the thin film following standard lift out procedures and thinned down to ~80 nm using 0.3 nA cleaning cross sections. STEM/EDX images and maps were collected on a JEOL 2800 at 200 kV. STEM/EELS spectra were collected on a JEOL JEM-ARM300CF at 200 kV.

Atomic Force Microscopy (AFM). AFM imaging was conducted to obtain LiPON surface roughness, using a Veeco scanning probe microscope equipped with a standard silicon probe (Umasch NSC15/AlBS) in tapping mode. Data were processed using NanoScope software.

X-Ray Diffraction (XRD). Grazing angle XRD spectra were collected with a Rigaku SmartLab X-Ray diffractometer with Cu Kα source operating at 30 kV and 15 mA with a step size of 0.05° at 1°/min scanning over 10-70°.

5.2.3. Mechanical Characterization

Experimental Design. Pristine LiPON was exposed to ambient humidity for 8-12 hours prior to mechanical testing, after testing in oil and wiping off oil using a kimwipe. To measure Young's modulus *E* and hardness *H*, instrumented indentation under reduced humidity was used as reported in detail in our recent work.[144] LiPON samples were secured to a stainless steel spacer and then onto a steel stub with low-viscosity cyanoacrylate (Loctite) and placed into a fluid cell designed for use with a nanoindentation system (Micromaterials, LLC, Wrexham, UK). To minimize air exposure, the basin of the fluid cell was filled with mineral oil (Alfa Aesar) in an argon glovebox (less than 10 ppm H_2O and 1 ppm O_2) before careful mounting into the

instrumented indenter under continuous oil immersion. A lever arm was attached to the pendulum, and the indenter tip was screwed into this lever arm. Both the tip and the sample were immersed constantly in the oil during measurements.[170, 171] Machine compliance calibrations were conducted to determine the change in machine compliance after attachment of the lever arm.

Young's modulus was measured at distinct sample surface locations in a rectangular grid of replicate load-displacement profiles, with center-to-center spacing among indentations of 50-70 μm. Results were reproduced with low standard error among indentation sets, over multiple substrates and thicknesses. A diamond nanoindentation probe of Berkovich (trigonal pyramid) geometry was used, and diamond area functions were obtained for experiments on fused silica for the maximum plastic depths attained on LiPON. Load-depth hysteresis were acquired to a maximum of ~0.1 mN for LiPON prior to air exposure, and of 1 mN after air exposure. These loads corresponded to average depths of ~360 nm prior to air exposure (due to instrument contact algorithm limitations), and ~80 nm to 545 nm after air exposure. A study of depth-dependence of Young's modulus of ambient humidity-exposed LiPON showed that over the range of maximum depths of 60-500 nm, the Young's modulus did not change within error . This indicates that the observed difference in Young's modulus between pristine and ambient humidity-exposed LiPON is not due to differences in maximum measurement depth. For pristine LiPON, loading occurred over 120 sec and unloading over 30 sec, with a dwell time of 10 seconds at maximum load. This corresponded to loading and unloading rates of 6.7×10^{-4} mN/sec and 3×10^{-3} mN/sec, respectively.

For ambient humidity-exposed LiPON, the loading and unloading rate was 0.05 mN/second with a dwell time of 5 seconds at maximum load. As the LiPON film thickness was

~1 μm, maximum indentation depths of > 300 nm (prior to air exposure) may have resulted in mechanical contributions from the underlying substrate. Therefore, the Young's modulus values reported herein are maximum values, as the silicon and alumina substrates are ~180 GPa and ~215 GPa, respectively.[172]

Instrument Calibration. Due to pristine LiPON's relatively high compliance and contact detection algorithms of Nanotest 3 software, precontact test data saved automatically with each load-depth hysteresis curve had minimum contact depths of ~300 nm. It is not possible to achieve contact depths smaller than this with such compliant samples in our current software/hardware configuration. The nanoindentation load-depth curves were corrected for the unavoidable precontact depth by examination of precontact data for 10 curves per sample and averaging to obtain load and depth corrections, which were then applied.

Indentation Data Analysis. Nanoindentation data was analyzed using standard techniques.[173, 174] Indenter Young's modulus E_i and Poisson's ratio ν_i of the diamond indenter were taken to be 1140 GPa and 0.07, respectively,[175] and the Poisson's ratio ν of the sample was assumed as 0.25.[142]

All Young's moduli are reported as mean ± standard deviation with averaged Young's moduli from 31-98 load-hysteresis curves per sample.

5.3. Results and Discussion

5.3.1. Mechanical Properties of Li_2CO_3

To measure Young's modulus E and hardness H for Li_2CO_3, a pellet was prepared by spark plasma sintering Li_2CO_3 powder (Sigma Aldrich, 99%) for 10 min. at 300 °C and 60 MPa applied pressure (Thermal Technology SPS 10-3). This sample was polished in ambient air using

SiC grinding papers to grit size of 15 μm and diamond polishing pads (Buehler Limited, Lake Bluff, IL) to grit size of 0.5 μm. Since Li_2CO_3 has non-negligible solubility in water, mineral oil was used as the polishing fluid. Optical microscopy revealed interconnected porosity in this sample, with flat regions typically on the order of tens of microns; an image of the surface is shown in the **Figure 5.1**.

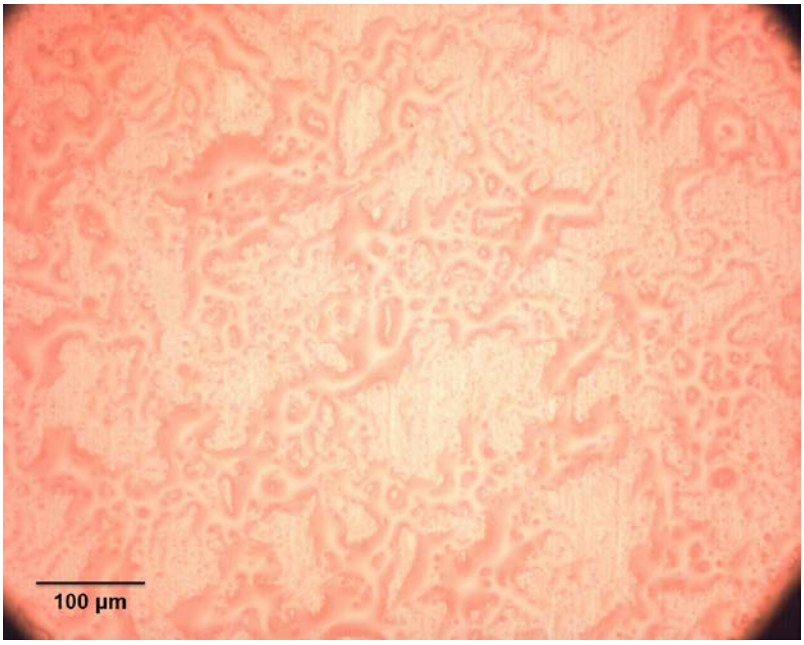

Figure 5.1. Optical Micrograph of Spark-Plasma-Sintered Lithium Carbonate (Li_2CO_3).

Mechanical measurements on Li_2CO_3 were obtained by conducting indentations with a Berkovich tip in grid patterns over the porous sample. Maximum loads of 1.0 mN and 0.5 mN were applied in square grids of 100 and 144 indentations, respectively, with 20 μm spacing between each indentation. Loading and unloading took place at 0.05 mN/s, with a dwell period of 5 s at maximum load. Many of the resulting hysteresis data were excluded from analysis based on influence from nearby porosity. Only indentations with maximum depths less than 100 and 70

nm were analyzed for the 1.0 mN and 0.5 mN tests, respectively, yielding a final sample size of 38 indentations (**Fig. 5.2**).

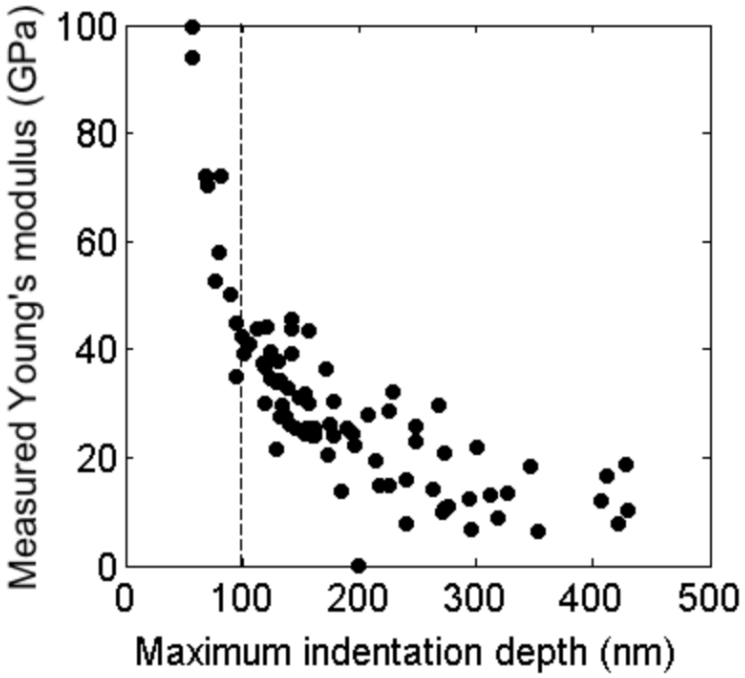

Figure 5.2. Young's Modulus of Li_2CO_3 as a Function of Maximum Indentation Depth. Dashed line indicates cutoff below which values were used to determine an average Young's modulus. Scatter plot banana shape characteristic of indentations affected by porosity is observed; the cutoff was chosen so as to minimize the effect of porosity while still also having a reasonable sample size for averaging. The result of this experiment was still affected by porosity even though such a cutoff was employed, so this estimate on the modulus of Li_2CO_3 represents a lower estimate.

5.3.2. LiPON Stability in Mineral Oil

LiPON samples were immersed in mineral oil (Alfa Aesar) for 24 hours in a glovebox purged with high purity argon (99.9995%) and maintained with oxygen and water vapor levels less than 5 ppm. Afterwards the residual oil was wiped off and washed with hexanes (Fisher Scientific). Fourier transform infared spectroscopy (FTIR) was performed (Perkin Elmer Spectrum Two) to probe bulk film structural analysis, and x-ray photoelectron spectroscopy (XPS) was performed (Kratos AXIS Supra) to detect any surface reactions (**Fig. 5.3**). After

exposure to mineral oil, there is little change in the sample appearance and reflectivity. For both samples the IR spectra exhibit the characteristic vibrations of LiPON with peaks corresponding to asymmetric stretching of PO_2^- (1240 cm^{-1}), asymmetric stretching of PO_4^{3-} (1100 cm^{-1}, 1000 cm^{-1}), asymmetric stretching of PO_3^{2-} (1066 cm^{-1}), symmetric stretching of P-O-P (880 cm^{-1}), and the bending motion of PO_4^{3-} (582 cm^{-1}). While there is significant increase in C 1s signal, this is likely due to residual mineral oil on the sample surface, and there is no change to Li 1s, P 2p, O 1s, and N 1s spectra. Therefore, we conclude that mineral oil is an effective way to isolate LiPON from adverse environmental considerations during mechanical testing.

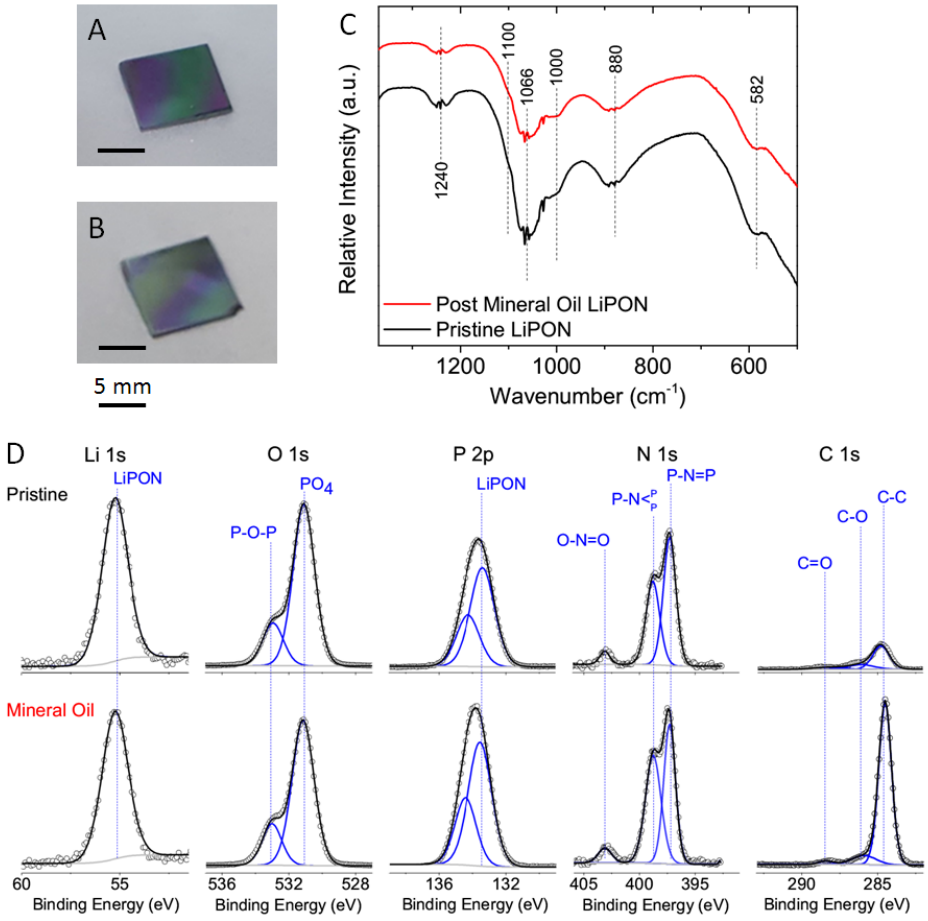

Figure 5.3. Optical and chemical characterization of LIPON before and after mineral oil exposure. Camera image of pristine (A) and mineral oil immersed (B) LiPON along with (C) FTIR spectroscopy and (D) XPS analysis indicates no chemical reaction between LiPON and mineral during mechanical measurement.

5.3.3 Mechanical Properties of LiPON

We determined mechanical properties of LiPON via instrumented indentation, prior to exposure to ambient humidity (i.e., unexposed or pristine LiPON) and after that controlled exposure. **Figure 5.4** summarizes the approach and Young's elastic modulus *E* that we obtained for both conditions. Prior to air exposure, LiPON was significantly more compliant (>200-fold) than previously reported,[142] with *E* = 0.2-0.4 GPa (**Fig. 5.4.B**). However, after exposure to ambient humidity, the Young's modulus of all LiPON films ranged between 67-80 GPa. This stiffness agreed well with magnitudes reported in previous studies that conducted experiments in ambient humidity[141, 142] or simulated pristine LiPON. We found that LiPON exposed to ambient humidity ranged in *E* from 77-80 GPa, while LiPON exposed to O_2 and H_2O levels >10 parts per million as well as other materials for prolonged periods (stored in a vented glovebox prior to mechanical characterization) was similar and ranged 67-72 GPa. Given the evidence in the literature for Li_2CO_3 growth upon exposure of such materials to ambient humidity, we speculated that this change in *E* was due to formation of Li_2CO_3 at the exposed surface. **Figure 5.4** supports that hypothesis, in that *E* for ambient humidity-exposed LiPON corresponded to both elastic moduli calculated for Li_2CO_3 and to our own measured *E* for pure Li_2CO_3 (**Fig. 5.4.B** and **Fig. 5.2**). We also measured the hardness of LIPON under these distinct conditions, as one measure of resistance to plastic or permanent deformation, with similar reduction in pristine LIPON. **Figures 5.4.C** and **5.4.D** illustrate this effect of exposure to ambient humidity schematically, where the indentation deformation volume under a given load is larger upon exposure to ambient humidity, consistent with the orders of magnitude lower stiffness and hardness.

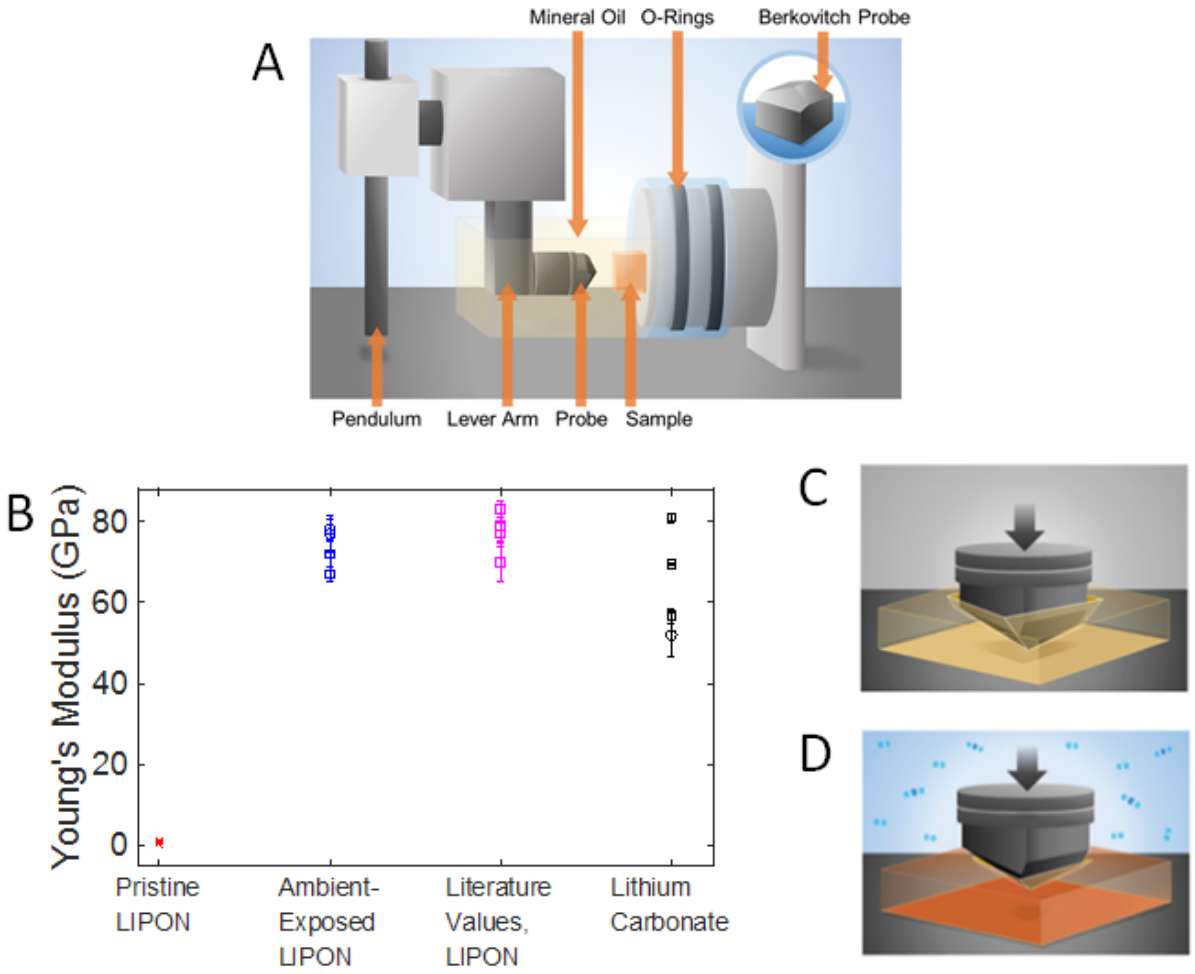

Figure 5.4. Nanoindentation of LiPON Before and After Exposure to Ambient Humidity. (A) Schematic of nanoindenter probe and mineral-oil filled fluid cell used for instrumented nanoindentation of LIPON. Immersion of the sample in mineral oil significantly mitigates sample exposure to ambient humidity.(B) Young's modulus of LiPON before (pristine, or unexposed to humidity) and after exposure to ambient humidity. C, D. Schematic of indentation of LIPON at identical applied load, indicated by arrow, before (C) and after (D) exposure to ambient humidity. In B, blue circles indicate LIPON exposure to ambient humidity, while blue squares indicate exposure to oxygen, water vapor and potentially other gases in a vented glove box environment. Black squares represent simulated lithium carbonate,[172] while the open-black circle represents our experimental result for lithium carbonate. Young's modulus data for LiPON in (B) are from Xu et al.[141] and Herbert et al.[142], and for simulated lithium carbonate are from the Materials Project.[172]

During indentation, samples were immersed in mineral oil to mitigate exposure to ambient humidity, as shown in **Figure 5.4**. This fluid is inert and not known to react with Li,[176] and we and others have found this approach more effective in mitigating air exposure than gas-purged environments that require sample exchange. This approach has been established previously by us and others for Li and Li-containing materials including battery electrode materials, to facilitate mechanical characterization of samples that otherwise react rapidly with air and humidity. [144, 145, 176, 177] Previous nanoindentation studies comparing mechanical properties measured for various materials in air and in mineral oil found no detectable differences.[176] Ambient humidity-exposed samples were equilibrated in air for several hours prior to nanoindentation experiments, after removal of the mineral oil simply by wiping the sample surface with Kimwipe® paper. We identified no detectable change in the sample translucence after oil removal and no change in the film chemistry (**Fig. 5.3**). Furthermore, ambient humidity-exposed LiPON samples that were then later immersed and tested in mineral oil (blue points in **Fig. 5.4.B**) did not show a decrease in Young's modulus or hardness.

5.3.4. LiPON Characterization

Figure 5.5 summarizes surface characterization of LiPON before and after exposure to ambient humidity, by which we established that such marked differences in mechanical properties are attributable to formation of lithium carbonate (Li_2CO_3) upon exposure to ambient humidity.[165, 172] X-ray photoelectron spectroscopy (XPS) spectra of the LiPON surface before and after air exposure showed clear changes in surface chemical composition, with formation of new chemical species after air exposure (**Table 5.1**). Before air exposure, the peak positions and ratios of lithium, oxygen, phosphorus, nitrogen and carbon were consistent with previous reports for pristine LiPON.[89, 143, 178] However, after air exposure, peaks characteristic of LiPON

decreased significantly, and larger peaks corresponding to lithium carbonate (Li_2CO_3) and lithium hydroxide (LiOH) appeared along with a shift in the N 1s spectra. Furthermore, atomic composition analysis identified increases in the atomic percent of carbon and lithium after air exposure, at the expense of phosphorus and nitrogen (**Fig. 5.6**). Grazing angle X-ray diffraction (XRD) showed that LIPON is amorphous before and after air exposure, but the XRD spectrum of ambient humidity-exposed LIPON exhibits increased intensity in regions similar to regions of highest intensity in Li_2CO_3.

To further probe this reaction, high-angle annular dark field (HAADF) scanning transmission electron microscope (STEM) imaging and energy-dispersive X-ray spectroscopy (EDX) mapping of the air exposed sample indicated the formation of a large outer surface layer (~400 nm) composed of C and O (**Fig. 5.5.B**). There is an additional distinct intermediate layer with reduced C and P signal. Selected spectra from electron energy loss spectroscopy mapping of the different layers confirms that the outer most layer has significant lithium accumulation and a shift in oxygen k-edge spectra corresponding to Li_2CO_3 (**Fig. 5.5.C**).[179, 180] The intermediate layer is lithium deficient with reduced amounts of nitrogen phosphorous. Further, in the intermediate layer there is an additional pre-peak in the O-K edge and a decrease in the P L_3/L_3 ratio indicative of an increase in oxidation due to water absorption.[181, 182] This is similar to previous studies that hyhpothesize this phenomenon to H^+/Li^+ proton exchange due to reactions with atmospheric H_2O.[183] Although the nitrogen signal is weak, normalizing the XPS N1s spectra reveals an additional surface species, likely NH_3 formed from a reaction with atmospheric H_2O (**Fig. 5.6**).[143] [184] Together these results indicated that upon air exposure, LIPON hydrates and subsequently reacts with CO_2 to form Li_2CO_3.

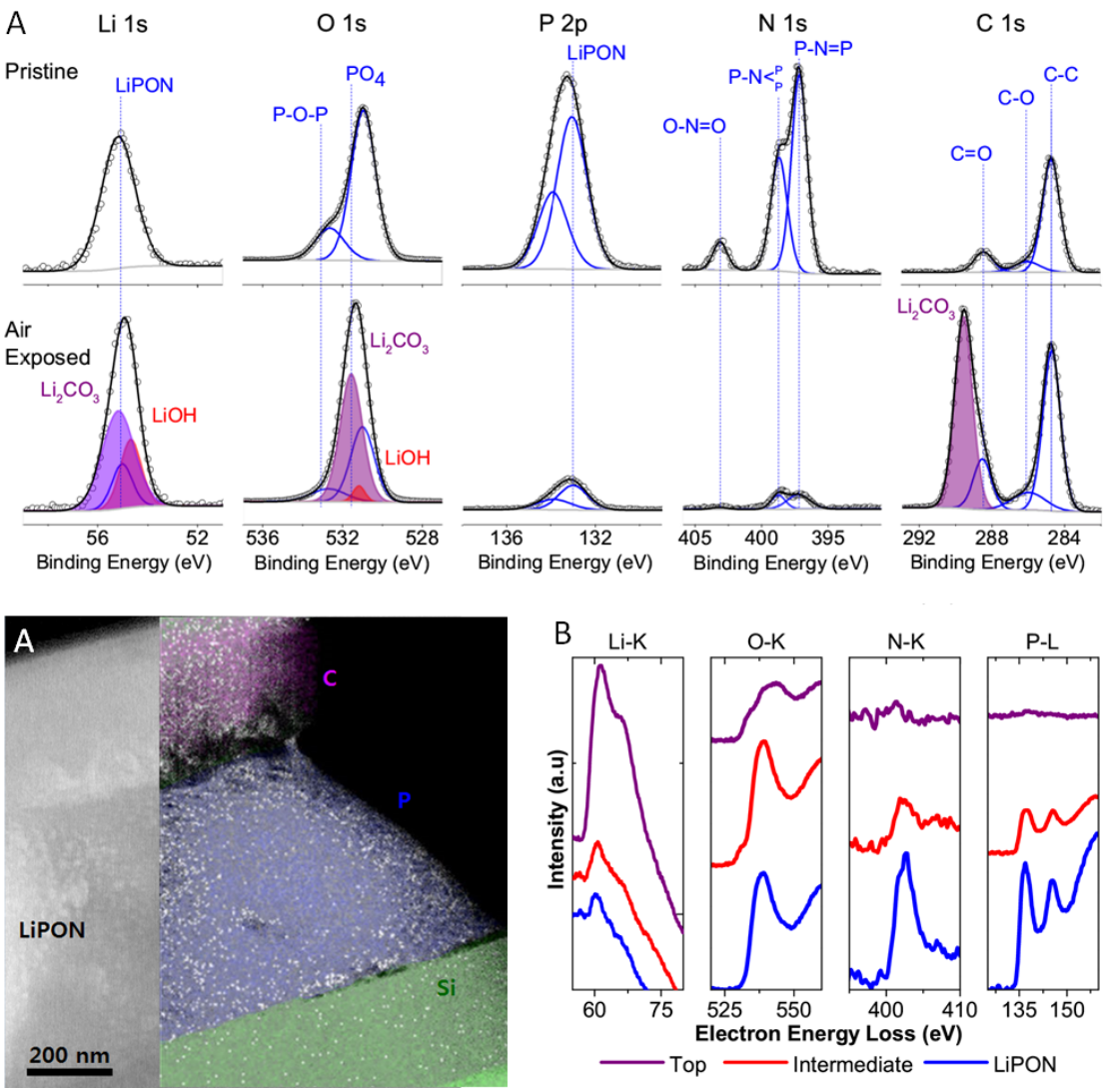

Figure 5.5. Characterization of LIPON before and after air exposure. (A) XPS spectra, (B) TEM image with EDX elemental mapping, and (C) EELS Li K-edge, N K-edge, and O K-edge of LIPON indicating the formation of Li_2CO_3, LiOH, and NH_3 after air exposure. For all data blue represents LiPON, purple Li_2CO_3, and red the intermediate layer of LiO_H and NH_3.

Table 5.1. XPS binding energies for LiPON components.

Surface Component	Li 1s	O 1s	P 2p	N 1s	C 1s
LiPON	**55.1**		**133.0**		
	55.0[184] 55.6[89]		132.8[178]		
	55.4[143] 55.8[185]		133.6[89]		
P-O-P		**532.6**			
		532.7[184] 532.8[143]			
		533.0[89] 532.3[185]			
PO_4		**531.0**			
		530.6[184] 531.3[185]			
		531.4[89]			
O-N=O				**403.1**	
				~404[140]	
P-N$<^{P}_{P}$				**398.7**	
				398.6[184] 399.0[89]	
				398.9[140] 399.4[185]	
P-N=P				**397.2**	
				396.6[184] 397.6[89]	
				397.4[140] 397.8[185]	
Li_2CO_3	**55.3**	**531.6**			**289.6**
	55.3[186]	531.9[186]			290.1[186]
	55.2[187]	531.5[187]			289.8[187]
LiOH	**54.6**	**531.1**			
	54.7[186]	531.1[186]			
	54.9[187]	531.3[187]			
NH_3				**398.6**	
				398.5-400.9[188, 189]	

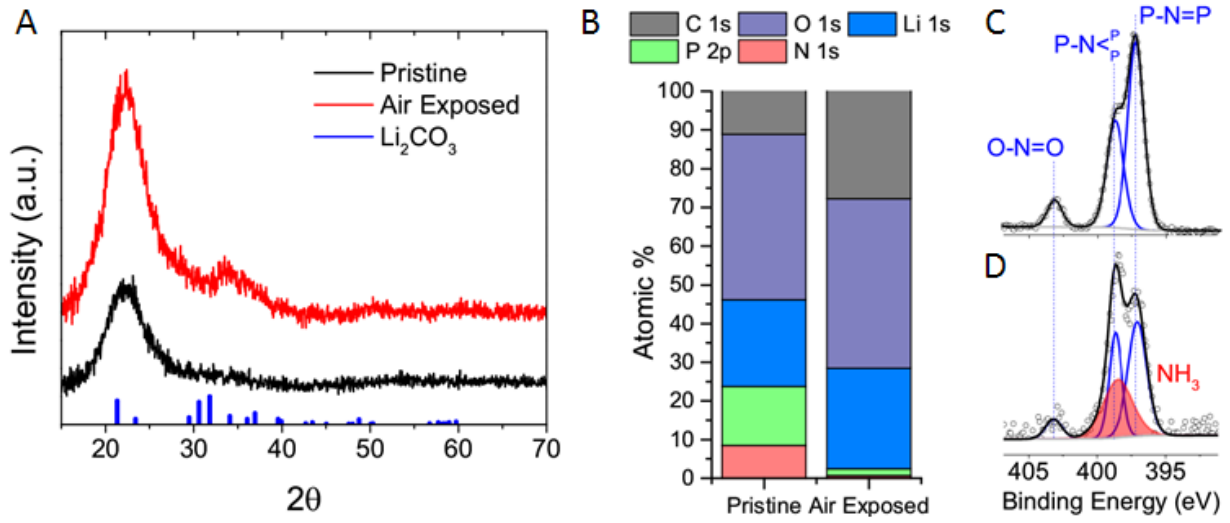

Figure 5.6. XRD and XPS of LIPON before and after air exposure. (A) XRD indicates increased intensity in areas corresponding to lithium carbonate after air exposure. (B) XPS elemental analysis reveals increased carbon and lithium at the surface after air exposure. Normalized high resolution N 1s spectra of (C) pristine and (D) after air exposure reveal that there is an additional nitrogen surface reaction, likely the formation of NH_3 from atmospheric moisture.

Electrochemical impedance spectroscopy (EIS) measurements before and after air exposure were also consistent with the formation of an electrochemically detrimental surface reaction layer upon exposure to air. Impedance spectra of pristine LiPON showed ionic conductivity of 1.8 x 10^{-6} S/cm, consistent with previous reports.[146] Upon exposure to ambient humidity, the ionic conductivity of the film immediately began to decay as shown in **Figure 5.7**. After several hours of ambient humidity exposure, the impedance spectra must be modeled as two pairs of RC components in series (**Fig. 5.8.A-B**), including a high resistivity component absent in pristine LIPON, which is attributed to the impedance of the surface reaction products, in addition to the low resistivity component representative of bulk lithium diffusion. There is also a reduction in bulk ionic conductivity, likely due to Li loss from the surface reaction. (See **Table 5.2** for electrochemical impedance spectral fitting parameters.) Both scanning electron

microscope (SEM) images (**Fig. 5.8.C-D**) and atomic force microscope (AFM) images showed detectable increases in surface roughness upon air exposure of LIPON (**Fig. 5.9.**).

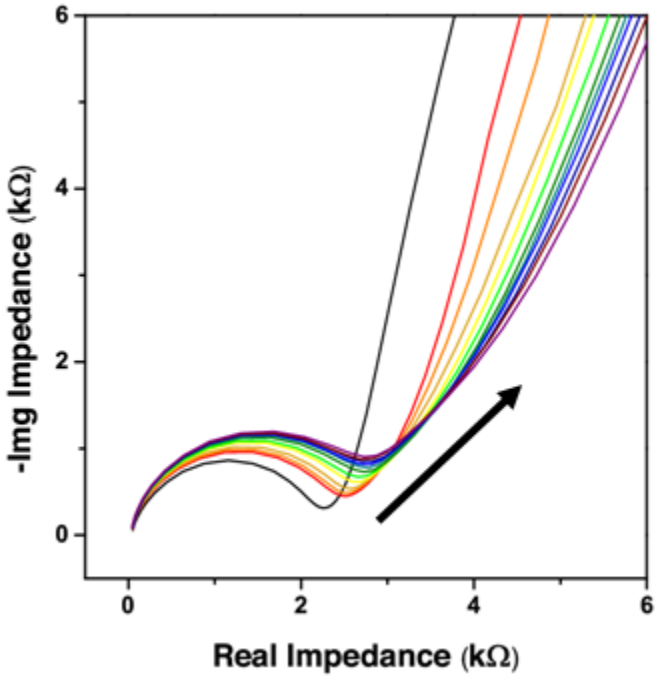

Figure 5.7. Evolution of Electrochemical Impedance Spectra of LIPON Exposed to Air Over Time. Electrochemical impedance spectra acquired every two hours follow the trend of increasing impedance with time, as indicated by the arrow.

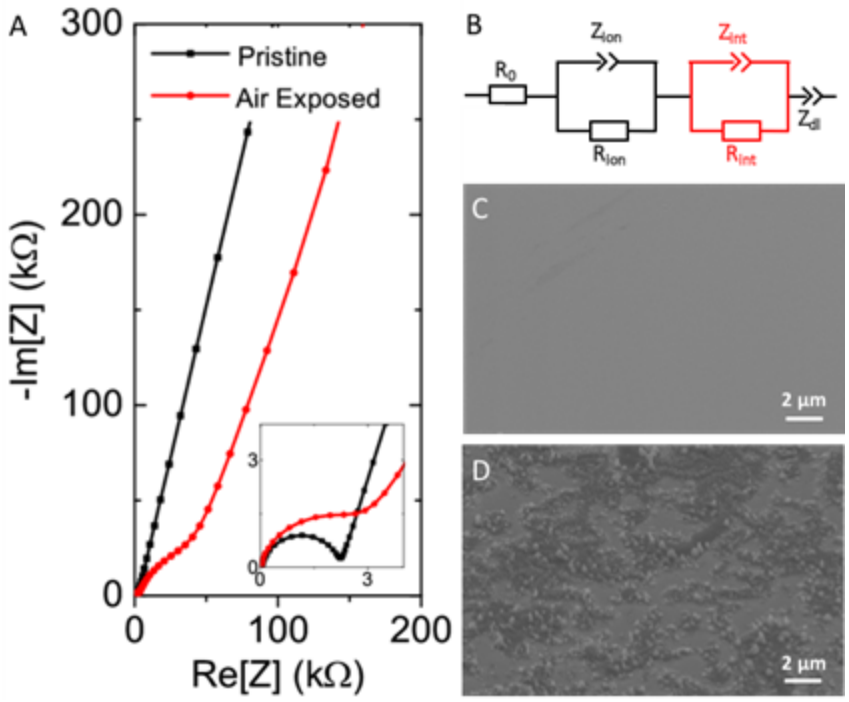

Figure 5.8. Electrochemical and SEM Characterization of LIPON Samples. (A) Electrochemical impedance spectrum of LIPON before and after air exposure, indicating drastically decreased ionic conductivity after air exposure. (B) Equivalent circuit corresponding to Nyquist plot. Scanning electron microscopy images of (C) pristine LiPON, prior to air exposure; and (D) after air exposure.

Table 5.2. Fit parameters used in the impedance spectra in Figure 3.

			CPE_{ion}			CPE_{int}		CPE_{dl}	
	R_0 (Ω)	R_{ion} (Ω)	C ($\overline{F\ s^{\eta-1}}$)	η	R_{int} (Ω)	C ($\overline{F\ s^{\eta-1}}$)	η	C ($\overline{F\ s^{\eta-1}}$)	η
Pristine	38.51	2211	6.59×10^{-9}	.87				3.25×10^{-6}	.81
Air	21.96	2530	2.24×10^{-9}	.93	34668	$.276 \times 10^{-6}$	.735	1.07×10^{-6}	.74

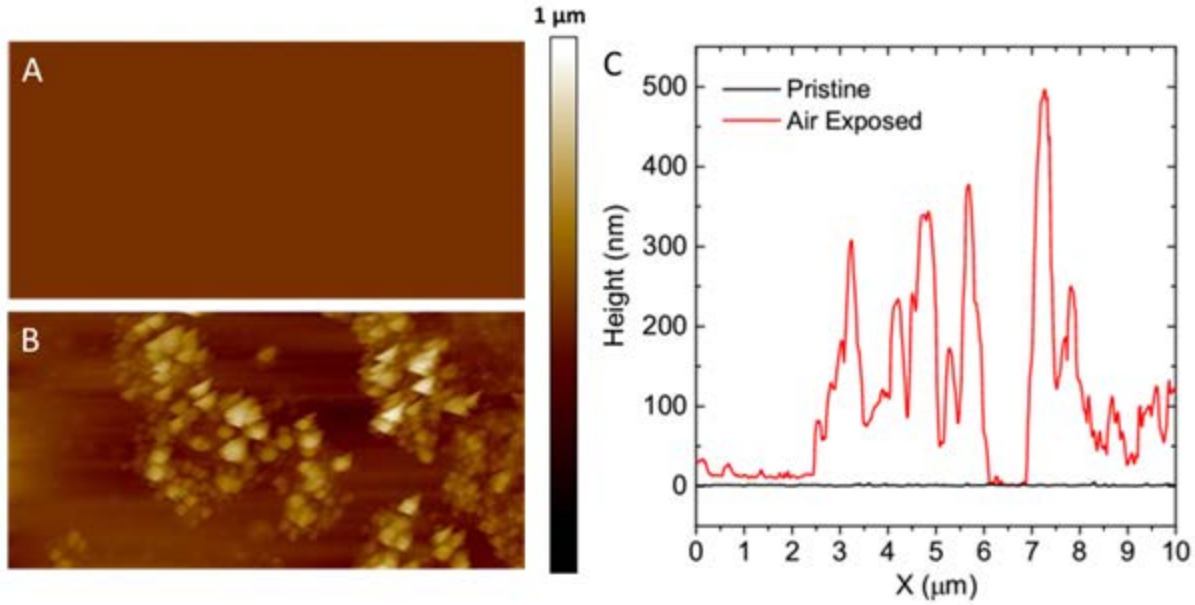

Figure 5.9. Surface Roughness Characterization of LIPON Samples. Atomic force microscopy images of (A) pristine and (B) air-exposed LIPON. (C) Resulting surface profile scans. Root mean square roughness of pristine LIPON was 0.52 nm. Roughness of ambient-exposed LIPON alternated between relatively flat areas and very rough areas as depicted.

5.4 Conclusion

The observed changes in mechanical properties and surface chemistry after exposure to ambient humidity highlights the importance of environmentally controlled mechanical testing of LIPON and other SSB materials. Note that the elastic modulus of LIPON that had not been exposed to ambient humidity was lower than that of Li metal electrodes by approximately one order of magnitude.[164] This relatively higher stiffness was not attributable to any detectable reactions with the environment used to mitigate water vapor exposure, and is in contrast with previous findings implying that this solid electrolyte was stiffer than Li metal. This LIPON Young's elastic modulus E corresponds to a shear modulus G = 0.1-0.2 GPa, which is more than forty-fold lower than that required to block dendrite penetration according to the Monroe-Newman criterion.[147] In other words, pristine LIPON does not meet this mechanical criterion and

would be predicted to be sufficiently compliant to facilitate dendrite penetration through the SSE bulk if this criterion accurately predicted this failure mode. Given the lack of documented dendrite growth in LIPON, these findings contrast strongly with the concept that SSE stiffness controls resistance to dendrite growth.

Figure 5.10 summarizes the relative macroscale mechanical differences and potential microscale implications of the findings in this work. As pristine LiPON is relatively compliant and soft, for a given indentation depth (and associated strain), the resulting stress would be lower due to the lower elastic modulus; rings in **Figure 5.10.a** schematize stress contours due to indentation at a given depth. Consequently, one would predict a lower associated lower stress in response to macroscale, externally applied deformation during battery assembly or to internal stresses in the SSE generated by strains associated with Li dendrite plating or other electrochemical cycling effects than those predicted for ambient humidity-exposed LiPON of relatively higher stiffness and hardness. In addition, the significantly lower hardness of pristine LiPON as compared to ambient humidity-exposed LiPON may facilitate conformation of this SSE to the electrode surface. While direct testing of these hypotheses in cycled electrochemical cells is beyond the scope of this study, we note that such relatively low stiffness and hardness of pristine LiPON in all-solid-state-batteries would promote the strain accommodation and previously observed ability of LiPON to sustain months of cycling with no evident degradation of the electrode-electrolyte interface.[140] Consistent with that prior work, our high-resolution scanning transmission electron microscopy (STEM) images of LiPON-electrode interfaces – using deposition methods and configurations relevant to all-solid-state microbattery designs – showed no evidence of LiPON internal porosity or LiPON-electrode interfacial defects (**Fig. 5.11**).

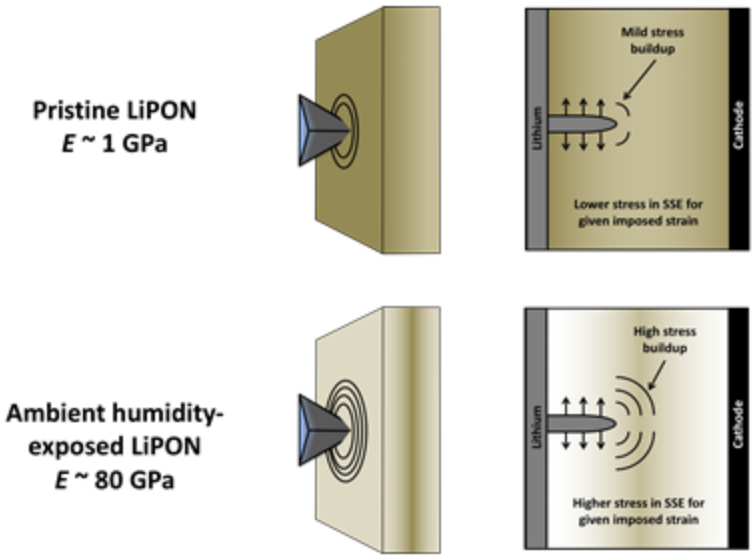

Figure 5.10. Schematic contrasting relative differences in mechanically distinct pristine LiPON and ambient humidity-exposed LiPON. (A) Application of indentation contact load, indicative of relatively low stress (rings as stress contours) at a given indentation depth, and (B) correspondingly mild internal stress in response to Li dendrite-associated strains (arrows) within the relatively compliant and soft solid state electrolyte (SSE) during cycling in pristine LiPON. (C) Application of the same indentation depth generates larger indentation stress, and (D) correspondingly higher internal stress from dendrite-associated strains if the LiPON SSE were exposed to and reacted with ambient humidity.

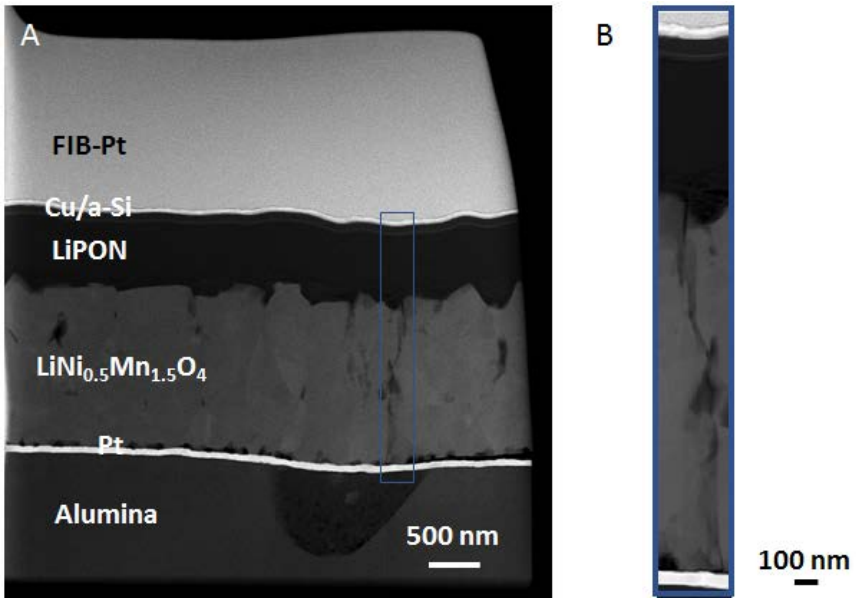

Figure 5.11. STEM Images of LiPON-electrode interfaces. HAADF image shows no visible defects at electrode-electrolyte interfaces.

The elastic modulus we measured for LIPON prior to air exposure (i.e., pristine, as-fabricated state) was also lower than that reported for other oxide or sulfide solid electrolytes. Those other solid electrolyte candidates range in *E* from ~18 GPa for glassy (amorphous) lithium phosphorus sulfide to ~200 GPa for oxide garnets.[144, 158, 190, 191] LIPON stiffness was also lower than that of crystalline silicon oxynitrides (*E* ~ 235-250 GPa[192]) and phosphate glasses (30-80 GPa[193-195]). Indeed, the stiffness of pristine LIPON was more similar to that of chalcogenide glasses, which can be as low as 5-10 GPa.[196] However, the hardness of pristine LIPON was one to two orders of magnitude lower than reported values for fully dense oxide or chalcogenide glasses.[144]

In summary, our work finds that LIPON, a widely used solid electrolyte, exhibited a Young's modulus that was 200-fold lower than that measured for such samples after exposure to ambient humidity. These findings highlight the importance of reduced humidity and *operando* techniques to quantify mechanical properties of candidate materials in solid state batteries, to guide both SSB design and modeling predictions of mechanical failure associated with electrochemical cycling.

This chapter in full, is currently being prepared for submission for publication "LiPON Solid Electrolyte Stiffens Upon Exposure to Ambient Humidity," S.N Raja, J.Z. Lee, T.A. Wynn, F.P. McGrogan, T. Swamy, Y.M. Chiang, Y.S. Meng, and K. Van Vliet. The dissertation author was the co-primary investigator and co-first author of this paper. All of the experimental parts were performed, analyzed, and written by the author except for the film growth and mechanical testing.

Chapter 6. Focused Ion Beam Fabrication of Electrochemically Active LiPON-based Solid-State Lithium-Ion Nanobatteries for *In Situ* Testing

Solid-state electrolytes are a promising replacement for current organic liquid electrolytes, enabling higher energy densities and improved safety of lithium-ion (Li-ion) batteries. However, a number of setbacks prevent their integration into commercial devices. The main limiting factor is due to nanoscale phenomena occurring at the electrode/electrolyte interfaces, ultimately leading to degradation of battery operation. These key problems are highly challenging to observe and characterize as these batteries contain multiple buried interfaces. One approach for direct observation of interfacial phenomena in thin film batteries is through the fabrication of electrochemically active nanobatteries by a focused ion beam (FIB). As such, a reliable technique to fabricate nanobatteries was developed and demonstrated in recent work. Herein, a detailed protocol with a step-by-step process is presented to enable the reproduction of this nanobattery fabrication process. In particular, this technique was applied to a thin film battery consisting of $LiCoO_2$/LiPON/a-Si, and has further been previously demonstrated by in situ cycling within a transmission electron microscope.

6.1 Introduction

Focused ion beams (FIB) have been used chiefly for transmission electron microscopy (TEM) specimen preparation and circuit editing.[105, 197] Nanofabrication using FIB has progressed significantly during the last two decades with much focus on semiconductor materials.[198] Despite its importance to scientific advances, major concerns with FIB techniques are ever present, and include surface damage, re-deposition, and preferential sputtering due to high current density.[199, 200] There have been several articles on the FIB damage of bulk materials during preparation of TEM specimens and several methods to reduce this damage have been proposed.[201-204] However,

FIB fabrication of active devices that consist of multilayers with different functionality are still limited.

For solid-state devices, especially in the field of energy storage, interfaces play a crucial role, and the solid-solid interface is most often seen as a dominant source of impedance.[103] These interfaces are particularly difficult to characterize, due to a combination of their buried nature and data convolution in the presence of multiple interfaces in a single device. The fabrication of all-solid-state nanobatteries is critical to probe and understand the dynamic nature of these interfaces, ultimately impacting the electrochemical processes in batteries. Thin film batteries based on lithium phosphorous oxynitride (LiPON) were demonstrated more than two decades ago and are currently commercialized.[140] Although FIB fabrication of electrochemically active nanobatteries from a thin film battery is critical for enabling *in situ* evaluation of interfaces, most attempts to fabricate nanobatteries using FIB fail to retain the electrochemical activity due to short-circuiting.[205] Initial attempts at *in situ* cycling thinned only a small portion of the nanobattery, to observe the lithium distribution by electron holography.[206]

More recent work has demonstrated the successful FIB fabrication of electrochemically active nanobatteries, which enabled both *ex situ* and *in situ* scanning transmission electron microscopy (STEM) and electron energy loss spectroscopy (EELS) characterization of interfacial phenomenon.[207, 208] Important FIB fabrication parameters that help to retain the electrochemical activity have been indicated by Santhanagopalan et al.[207], and a further detailed protocol is presented in this manuscript. This procedure is based on a model $LiCoO_2$/LiPON/a-Si battery, but will ultimately enable exploration of further thin film battery chemistries.

This method can help answer key questions in the solid-state electrochemistry field, uncovering the nature of buried solid-solid interfaces, including their thermodynamic and electrochemical stability during cycling. The main advantage of this in situ technique is that the nanobattery is never exposed to external factors, allowing an unhindered view of the dynamic processes limiting solid-state battery operation.

6.2 Experimental Protocol

6.2.1 Preparation of the Sample and System

Attain a complete thin film battery consisting of an Al_2O_3 substrate (500 µm thick), a gold cathode current collector (100 - 150 nm thick, DC sputtered), a $LiCoO_2$ cathode (2 µm thick, RF sputtered), a LiPON electrolyte (1 µm thick, RF sputtered), an amorphous silicon anode (80 nm thick, RF sputtered), and a Cu anode current collector (100 nm, DC sputtered).[209, 210] Mount a complete thin film battery on a 25 mm diameter aluminum SEM stub, and use a copper tape to electrically connect the cathode current collector to the SEM stub to minimize charging effects.

Prior to pumping down the chamber, confirm a low-noise electrical pathway exists to the copper grid, which the nanobattery will be mounted on and will serve as the conductive pathway to the cathode (**Fig. 6.1**). Connect the cathode lead to the stage through a shielded electrical feedthrough, as is present in systems equipped for electron beam induced current (EBIC) measurements with the appropriate connection type. Internally, connect the feedthrough to the stage with a shielded wire with an exposed tip; the method of securing the exposed wire tip will depend on the sample stage type, and, here, it is held in place by an unused stage set screw. Alternatively, and depending on the configuration of the grounding circuit of the instrument's

stage, connect the cathode lead of the potentiostat to the stage ground using a BNC cable as shown in **Figure 6.1**.

Perform the low-current noise test using the potentiostat in constant current mode. Apply the current with which in situ cycling is to be performed, and observe the accuracy and precision of the measured current. Note that using the configuration described above, a measured current of 1 pA ± 0.1 pA was achieved. Similarly, create a conductive pathway from the micromanipulator tip to the outside of the probe by connecting the anode lead of the potentiostat to the micromanipulator ground using a BNC cable or an alligator clip as shown in **Figure 6.1**. Again perform the low-current noise test using the potentiostat in constant current mode. Note that using the connections described, the minimum stable current achieved was 10 pA ± 1 pA, due to unshielded grounds connected to the micromanipulator.

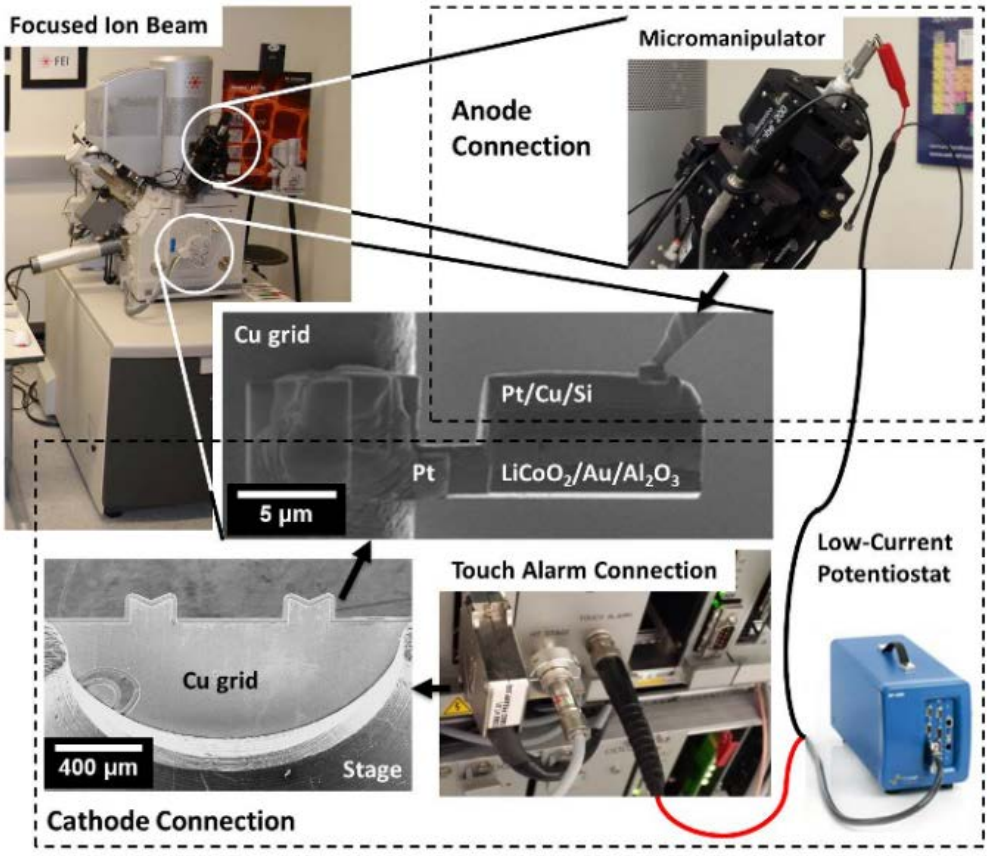

Figure 6.1. Electrical connection schematic. A potentiostat is connected to the FIB nanobattery via external connections: 1) the negative terminal of the potentiostat to the disconnected ground of the micromanipulator needle; 2) the cathode side to either an electrically shielded vacuum feedthrough or a direct connection to the stage ground such as a touch alarm circuit (shown). Internal connections are made between the tip of the micromanipulator and the anode, and between the cathode and stage through a copper TEM lift-out grid.

6.2.2 Lift-Out Nanobattery

Load the sample into the SEM/FIB chamber and pump down to system specified high vacuum (≤ 10-5 mbar) before turning on the electron beam and ion beam imaging. Focus the electron beam on the thin film battery surface and determine the eucentric height using standard SEM/FIB procedures.[105] Tilt the sample such that the ion beam is normal to the battery surface (here 52° sample tilt), and deposit a 1.5 to 2 µm thick layer of FIB deposited organometallic

platinum on the top current collector of the thin-film battery using an ion beam current of around 0.3 nA and dwell time of 200 ns over an area of 25 x 2 µm (**Fig. 6.2**).

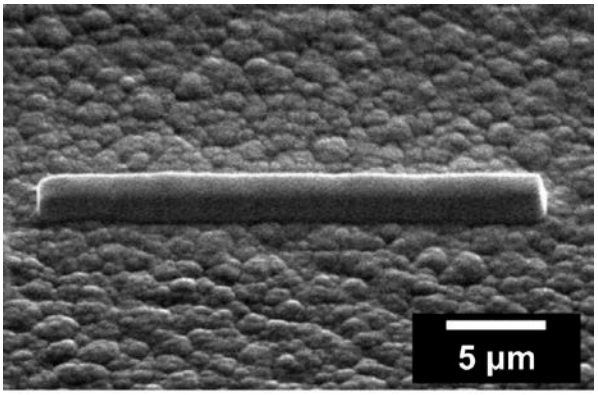

Figure 6.2. Pt deposition. SEM image of the Pt protective cap deposited on the thin film battery surface to avoid damage and making contact.

Set ion beam voltage to 30 kV and ion beam dwell time to 100 ns for the remainder of the experimental protocol. Use a step-pattern cross-sectional FIB milling option, as provided in the FIB software, to expose the nanobattery stack around the Pt-deposit, as in TEM lamella preparation.[1] Select a milling current ≤2.8 nA. Input a mill depth extending at least 1 µm beneath the active thin film battery (Z = 5 µm in this case), a cross-sectional width (X) of 25 µm and a cross sectional height (Y) of 1.5 x Z (here, Y = 7.5 µm). Afterwards, the battery cross-section is exposed, to be viewed in SEM (here, the electron beam is 52° from surface normal) as in F**igure 6.3**. Note that the actual milled depth is thin film battery dependent. Use a cross-section cleaning procedure, provided in the FIB software, where the ion beam incrementally rasters closer to the surface being cleaned, with an ion beam current ≤ 0.3 nA to clean off re-deposited material and clearly expose the layered structure (**Fig. 6.3**).

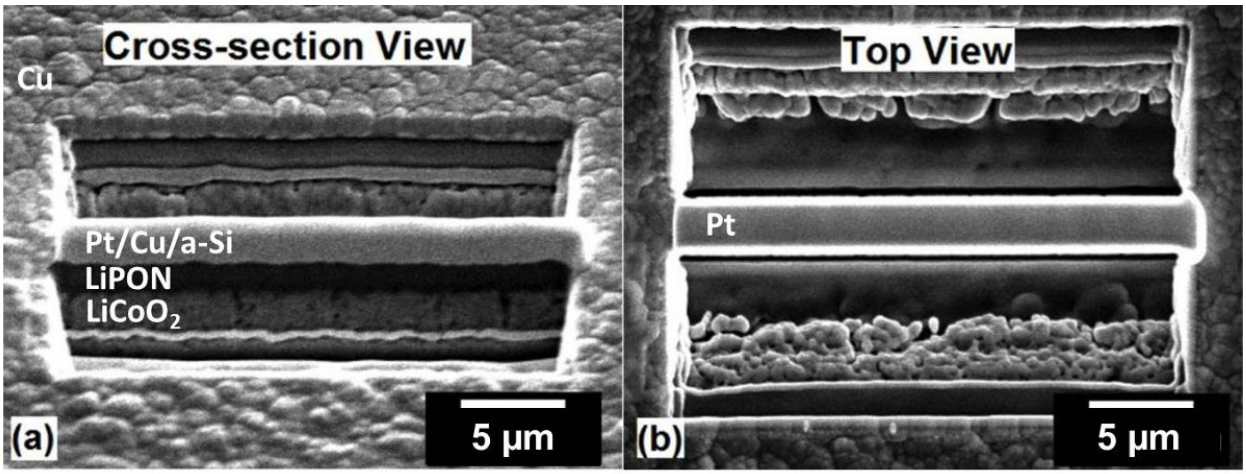

Figure 6.3. Nanobattery cross-section. SEM images of the nanobattery lamella after cross-sectional cutting at (a) 52° cross-section view and (b) and 0° top view.

Perform a series of rectangle under-cuts (also called J-cuts or U-cuts) at a stage tilt of 0° and beam current ≤2.8 nA to isolate the majority of the nanobattery. Make under-cuts consisting of i) a lower rectangle 0.5 x 25 µm below the Au current collector onto the Al2O3 substrate, ii) a vertical rectangle 0.5 µm wide (X) and through the entirety of the nanobattery thickness (Y), and iii) a vertical rectangle 0.5 µm wide (X) and with a height less than the nanobattery thickness (Y - 2.5 µm) around the Pt-coated nanobattery as in **Figure 6.4.a**. These three under-cuts should be performed in parallel mode (simultaneously milled), to prevent re-deposition of material within the under-cut regions. Rotate the sample 180° and repeat the same horizontal undercut. This isolates the bottom and sides of the nanobattery except for the remaining connected region. Rotate the sample 180°.

Insert the micromanipulator to the park position specified in the control software, then slowly bring it in contact with the nanobattery using the x-y-z movement of the software. Fix the micromanipulator to the Pt region on top of the nanobattery by ion-beam depositing 0.5 µm thick

Pt using a 30 keV ion beam with a current of 10 pA over an area of 2 x 1 µm. Ion mill the remaining connected portion of the nanobattery with a beam current around 1 nA, and raise the nanobattery vertically with the micromanipulator (**Fig. 6.4.b**).

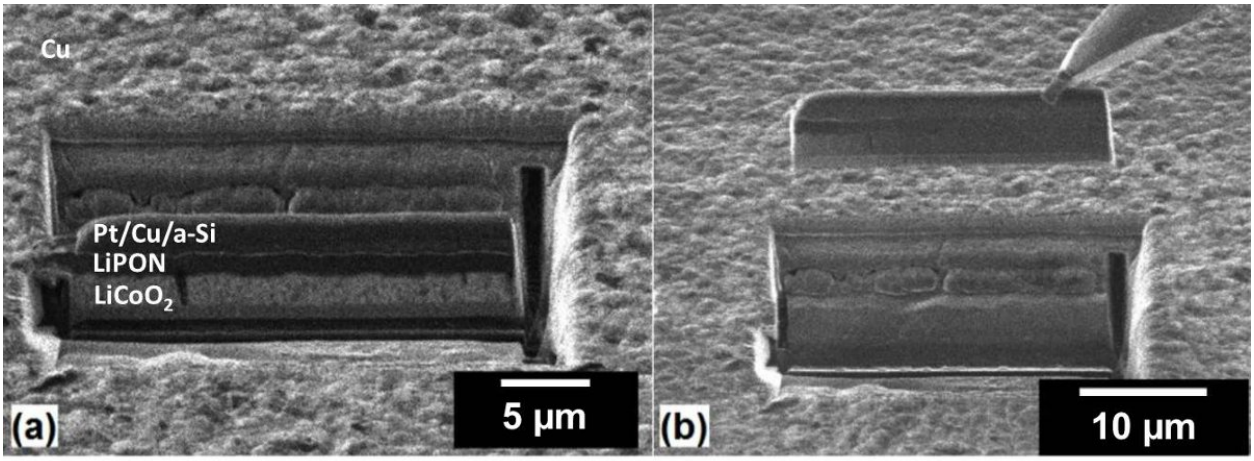

Figure 6.4. Nanobattery liftout. Ion-beam images of (a) the lamella with under-cut and (b) lift-out of the isolated nanobattery by the micromanipulator.

Mount the nanobattery on a Cu FIB lift-out grid with 2 µm thick ion-beam deposited Pt using a 30 keV ion beam with a current of 0.28 nA over an area of 10 x 5 µm. Ion mill away the connection between the micromanipulator and nanobattery using a 30 keV ion beam with a current of 0.28 nA over an area of 1 x 1 µm to a depth of 2 µm, leaving a freestanding section attached to the Cu grid (**Fig. 6.5**). Note that the Cu lift-out grid provides a flat base for mounting the nanobattery as well as serving as a conductive pathway between the stage and the nanobattery.

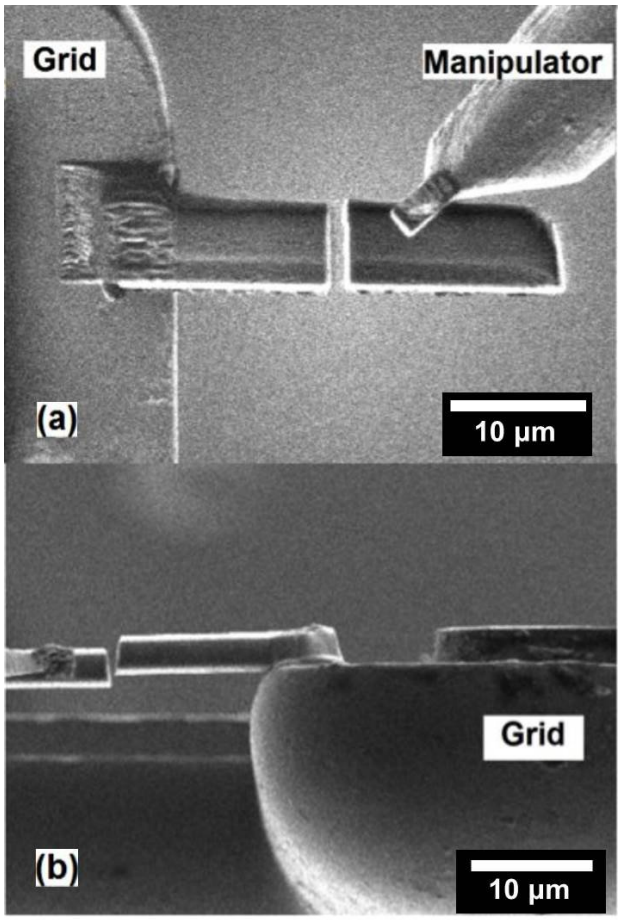

Figure 6.5. Nanobattery mounting. (a) Ion-beam and (b) SEM image of welding the lifted nanobattery to the copper TEM grid.

6.2.3 Cleaning and Cycling Nanobattery

Tilt the sample such that the ion beam is normal to the battery surface and use a cross-sectional cleaning procedure to remove re-deposited material over a 5 µm wide section of the nanobattery near the Cu grid, leading to a clear view of individual layers of the nanobattery (**Fig. 6.6.a**). Note that the re-deposited material from previous milling steps must be removed from the grid-mounted nanobattery to expose the electrochemically active core of the nanobattery and prevent shorting. Deposit 500 nm thick FIB-Pt using a 30 keV beam with a current of 0.1 nA

over an area of 1 x 2 µm to create an electrical contact between the cathode current collector and the metallic grid, which is electrically connected to the stage (**Fig. 6.6.b**). Tilt the sample to 0° and, using an ion beam current of 1 nA, make a rectangular cut 3 µm wide and deep enough (Z ~ 2 µm) to completely remove the anode current collector and electrolyte, isolating the anode from the Cu grid (**Fig. 6.6.c**). Isolating the anode and anode current collector before making electrical contacts is the most crucial step described in the protocol. Without appropriate connection and isolation, the nanobattery will be shorted and will not cycle. Use the cross-section cleaning procedure with an ion beam current around 0.1 nA to remove the re-deposited material around all sides of the nanobattery cross-section until all the individual layers are distinctly visible as shown in **Figure 6.6.d**. Insert the micromanipulator to the park position and, using the control software, bring the micromanipulator in contact with the Pt above the anode current collector. Ion beam deposit 0.2 µm thick Pt using a 30 keV ion beam with a current of 10 pA over an area of 2 x 1 µm to "weld" connect the micromanipulator and current collector (**Fig. 6.6.d**) Run the potentiostat in galvanostatic cycling mode. Current parameters used depend on the ultimate cross-sectional area of the fabricated nanobattery and desired C-rate, but will generally be on the order of a few nA. We select charge and discharge currents such that the current density is on the order of tens of µA/cm2 . For $LiCoO_2$-based thin film batteries, the voltage range is 2.0 and 4.2 V.

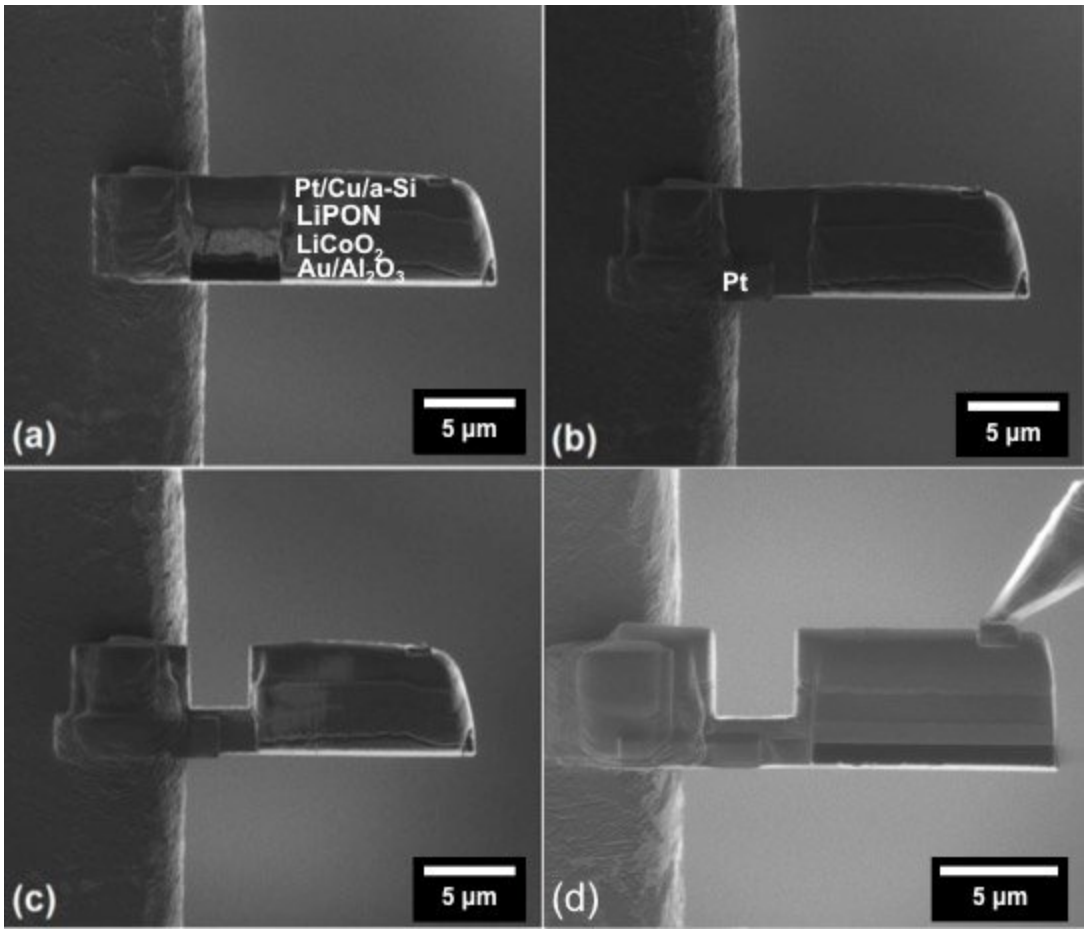

Figure 6.6. Nanobattery cleaning. Ion-beam images of (a) cleaning one of the nanobattery cross-sections, (b) electrically connecting the grid and cathode current collector by Pt deposition, (c) cut to isolate anode from the TEM grid, and (d) cleaning the cross-section of the front, back, and sides to remove all re-deposited material. Final contact is made to the anode using the micromanipulator for biasing.

6.3 Results and Discussion

6.3.1 Cycling of LCO Nanobettery

Figure 8 shows in situ testing of the electrochemical charging profiles of two cells that were fabricated. Both profiles clearly show a 3.6 V plateau corresponding to $LiCoO_2$/a-Si full cell chemistry and oxidation of $Co^{3+} \rightarrow Co^{4+}$. Cell-1 (**Fig. 6.7.a**) was tested at a lower current density (50 µA/cm^2) limiting the charge capacity to 12.5 µAh/cm^2. Cell-2 (**Fig. 6.7.b**) presents a

charging profile at a higher current density, 1.25 mA/cm^2, that was limited by the upper cut-off voltage of 4.2 V. The capacity recorded was about 105 µAh/cm^2, close to the theoretical capacity of Cell-2 (110 - 120 µAh/cm^2). The first discharge capacity of the nanobatteries has been poor while the subsequent cycle capacities (both charge and discharge) were limited due to the first cycle irreversibility. The discharge process of nanobatteries is still not optimized, however, a representative charge/discharge profile at a current density of 60 µA/cm^2 is presented in **Figure 6.8**. The charge capacity was limited to 30 min and the discharge was limited to 2 V, and it is evident that the reversibility is about 35%. Though the reversibility is a lot better than what is reported in the literature,[207] further optimization is necessary. If the voltage profile is not consistent with the thin film battery chemistry, this is likely due to either beam damage or shorting from re-deposited material.

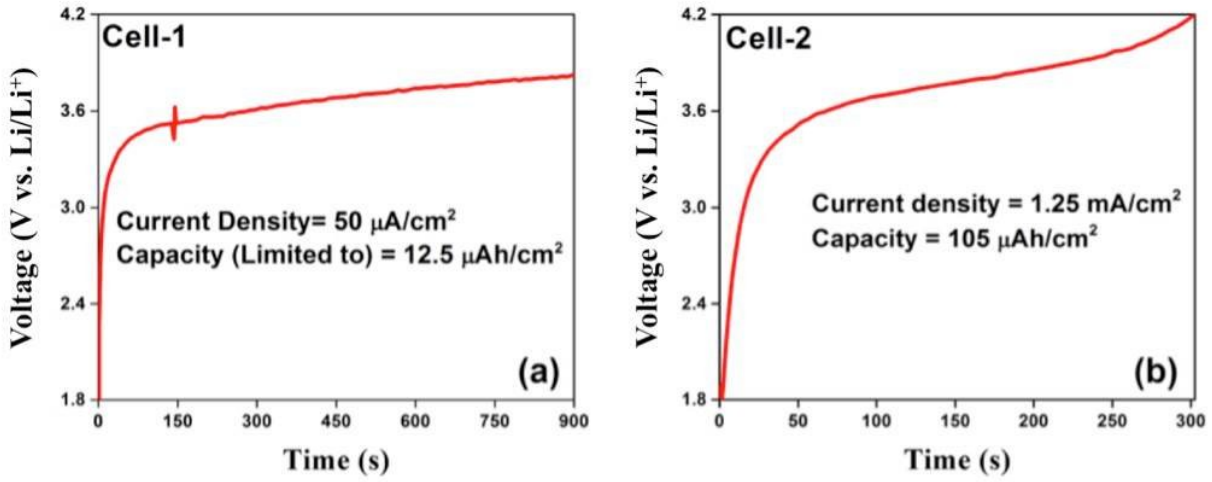

Figure 6.7. Nanobattery charging data. FIB fabricated nanobattery electrochemical charging profile at different current densities with (a) the capacity limited to 12.5 µAh/cm^2 and (b) the voltage limited to a 4.2 V cut-off.

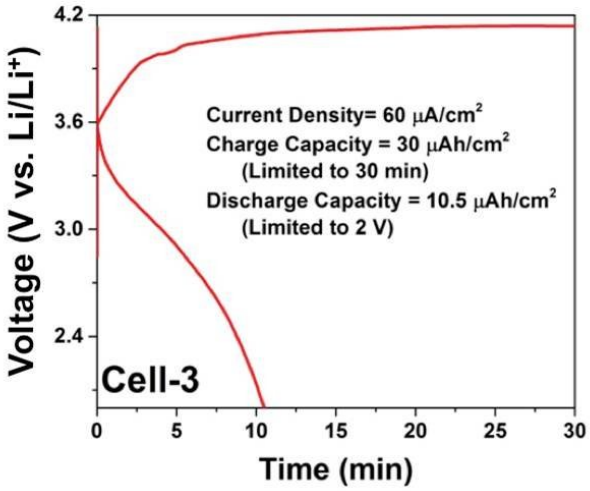

Figure 6.8. Nanobattery cycling profile. FIB fabricated nanobattery electrochemical charging and discharging profiles at a current density of 60 μA/cm^2.

6.3.2 FIB Protocol Obstacles

The technique described produces electrochemically active nanobatteries lifted out from a larger thin-film battery. Such techniques have enabled both ex situ and *in situ* STEM/EELS characterization of the buried interfaces by galvanostatically biasing the nanobattery.[207, 208] This allows unprecedented high-resolution characterization of quantitative chemical phenomena linked to the electrochemical state of charge. However, to achieve these results, a number of specific obstacles must be overcome.

Before beginning FIB processing, constant current testing should be conducted to ensure that there is a low-noise electrical pathway to the cathode and anode of the nanobattery. Cathode-side testing may be performed with the FIB chamber vented. Before pumping down the chamber for nanobattery fabrication, the positive terminal should be connected as if performing the experiment (either through a vacuum feedthrough or stage ground), and the negative terminal

connected directly to the stage. Note that if using the touch alarm as a stage connection, the touch alarm capability of the instrument may be disabled, and the connection should only be made when no further tilting of the stage is necessary. However, here the test will require the system to be under vacuum, and the current will pass through both the micromanipulator and the stage circuit. The micromanipulator can be electrically adhered with Pt to the copper grid for constant current noise tests. If current resolution issues persist, contact your vendor for information on how to decouple the stage from the system ground.

For this technique to work, it is critical to use the provided ion beam specifications to minimize damage to the solid-electrolyte LiPON. LiPON is highly sensitive to prolonged exposure to (i) humid atmospheric conditions, (ii) electron beam, and (iii) ion beams. Hence the solid-state nanobattery fabrication process requires minimization of exposure to all three of these conditions. Pre- and post-fabrication exposure to atmospheric conditions should be absolutely minimized. The in situ FIB cycling process described was developed as a solution to minimize this exposure. During and after fabrication, electron beam imaging should be limited, as it damages the solid-electrolyte. Similarly, ion beam imaging should also be limited to avoid degradation of the electrolyte and other active components as well. The specific milling files and times are based on the equipment outlined in the table of materials/equipment for specific reagents, equipment, and manufacturers; this may vary between FIB instruments, and modifications may be required when using another instrument.

Of all parameters in the FIB fabrication of a nanobattery, the most critical considerations are the use of low beam current and dwell time to minimize damage.[207] Whenever required, imaging is performed with electrons at low pixel dwell times and with the ion beams at lower beam current (usually in pA) and low dwell time (100 ns). Most of the time, high dwell time

electron beam imaging produces visible changes on the LiPON electrolyte. **Figure 6.9.a** shows an undamaged LiPON and further imaging with an electron beam induces damage to the LiPON layer as shown in **Figure 6.9.b**. This damage is irreversible resulting in a contrast change and will render the nanobattery electrochemically inactive.

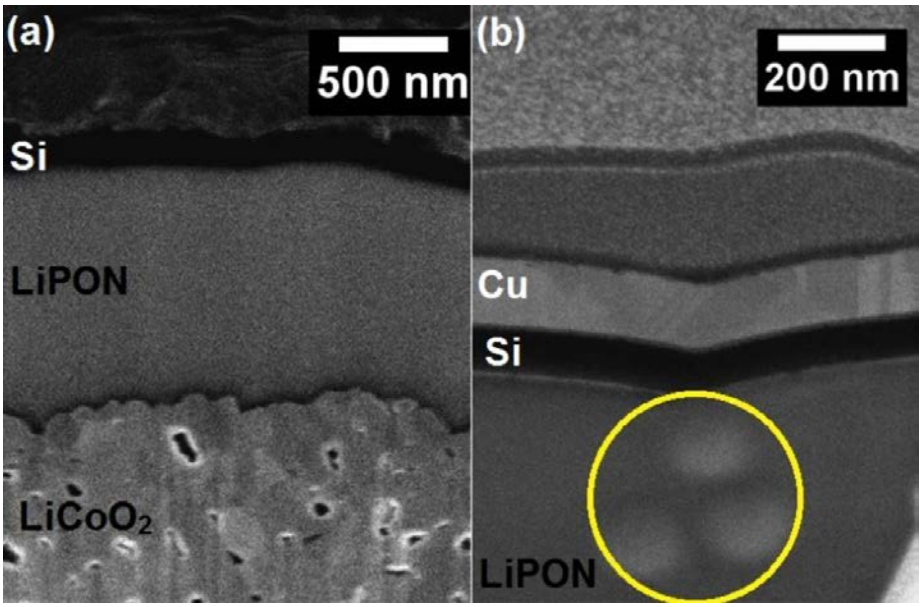

Figure 6.9. Nanobattery damage. SEM images of a nanobattery cross-section with (a) undamaged LiPON layer and (b) imaging at higher magnification induced damage in the LiPON layer indicated by the circle. High dwell time electron beam imaging produces visible changes in the LiPON electrolyte.

Further, for electrochemical cycling, proper care must be taken to make electrical contact between the cathode current collector and the grid properly (**Fig. 6.6.b**). It is similarly important to maintain the micromanipulator contact to the anode; as seen in **Figure 6.7.a**, at around 150 s, a spike in the electrochemical data corresponds to a vibration induced contact issue with the anode. Given the potential for instability of the micromanipulator-anode contact, the in situ testing time is minimized by limiting the nanobattery capacity, in turn reducing the charging time.

If the voltage profile is not consistent with the thin film battery, the cleaning procedure is repeated as there is likely some re-deposition causing shorting issues (**Fig. 6.10**). The anode isolation step in particular is a large source of re-deposited material. The micromanipulator must be removed and further cross-sectional cleaning steps are needed to remove this material. This cleaning procedure decreases the nanobattery cross-section, so the current density should be corrected accordingly. It is noted that ion beam damage cannot be completely avoided and it is limited to between a few nm to a maximum of 25 nm into the surface, as calculated from ion scattering simulations SRIM program for 30 keV Ga+ into the electrode materials.[211] Low energy processing can reduce the damage to a large extent.[202] The FIB process demonstrated here is unique, and fabrication, manipulation, and in situ testing of nanodevices is enabled by FIB-SEM dual beam systems. It is possible to extend the process to any other battery chemistries and other nanoscale devices.

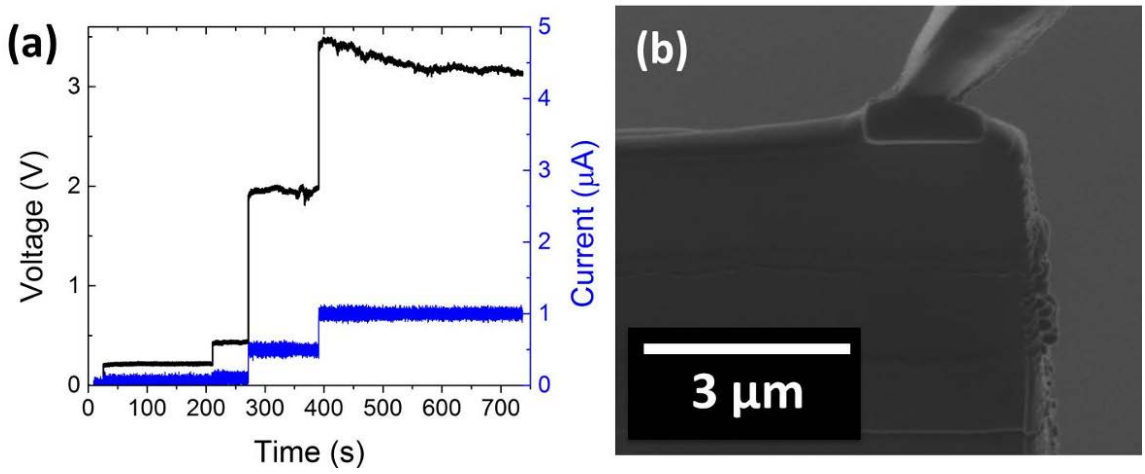

Figure 6.10. Shorted nanobattery. (a) Voltage profile of a nanobattery that had not been cleaned properly resulting in shorting from re-deposited material and (b) the cross sectional ion-beam image.

6.4 Conclusion

It is important to note that the specific parameters provided in this protocol may not directly transfer well to alternate electrochemical systems. LiPON was determined to be sensitive to thermal effects from the ion beam under high scanning rates. However, other electrolytes may suffer from other sensitivities. Similarly, although the material system tested in this protocol showed good electrochemistry after Ga^+ ion milling, other materials systems may be more susceptible to ion straggle and implantation. As such, more exploration of the parameter space may be required for alternate material systems. More sensitive materials such as sulfides may perform poorly after ion milling, though this area of research is largely unexplored with advanced characterization techniques. Realistically, these parameters will translate to most material systems of interest, as modern solid electrolytes are generally crystalline and more robust than LiPON. Despite these potential limitations, the technique will be applied to new material systems, offering the potential to discover alternate interfacial phenomena, ultimately uncovering impedance mechanisms. A natural follow-up to this technique is the observation of electrochemical cycling in the TEM. This has been performed on the system described in this protocol, and uncovered previously unseen behavior at these interfaces. This technique will enable the observation of alternate forms of impedance.

This chapter in part, is a reprint of the material, “Focused Ion Beam Fabrication of LiPON-based Solid-state Lithium-ion Nanobatteries for In Situ Testing” as it appears in the Journal of Visualized Experiments, J.Z. Lee, T.A. Wynn, Y.S. Meng, and D. Santhanagopalan, 2018, 133, e56259. The dissertation author was the co-primary investigator and co-first author of this paper. All of the experimental parts were developed and performed by the author. Thomas A. Wynn and the author analyzed and wrote the results.

Chapter 7. Cryogenic Focused Ion Beam Characterization of Lithium Metal Anodes for Lithium-Ion Batteries

Lithium metal is viewed as an ideal battery anode, but the implementation has been largely prevented by issues of dendrite formation and low coulombic efficiency. Determining the fundamental properties affecting lithium metal plating is challenging because characterization methods are largely limited by the ease with which lithium metal is damaged, notably altering structure and morphology. Recent work demonstrates the ability of cryogenic transmission electron microscopy (cryo-TEM) to observe the morphology and surface chemistry of nanoscale electrochemically deposited lithium. We extend cryogenic techniques to focused ion beam (cryo-FIB) characterizing bulk morphology of electrochemically deposited lithium. We demonstrate not only the importance of cryo-FIB for handling sensitive materials, but also elucidate the impact of electrolyte and additive selection in the density and morphology of plated lithium, which directly impacts long term cycling performance. We further extend cryo-FIB to process and analyze TEM lamella of lithium metal and lithium metal solid-state batteries.

7.1 Introduction

There is significant effort to enable lithium metal anodes for rechargeable batteries due to its low electrode potential (-3.04 V vs. standard hydrogen electrode) and high theoretical specific capacity (3860 $mAhg^{-1}$). However, despite nearly a half-century of research efforts, several challenges still exist such as the high lithium reactivity with electrolyte preventing the formation of a stable solid electrolyte interphase (SEI) and dendrite formation, resulting in short cycle life and safety risks. While various techniques have been applied to study lithium-ion battery mechanisms, there are key limitations to characterizing lithium because of its intrinsic high

chemical reactivity, low thermal stability, and low atomic number making it prone to contamination and melting, while exhibiting weak scattering characteristics for electrons and x-rays.[212] Elucidating the dynamic and complex phenomena during lithium deposition and SEI composition is necessary to developing mitigating strategies to enable widespread adoption.

Recently, cryogenic transition electron microscopy (cryo-TEM) techniques, which have a rich history of use in visualizing the structure of biomolecules[213], have proven powerful for observing the fundamental structure and SEI composition of nanoscale electrochemically deposited Li.[214, 215] Specialized holders maintain the sample temperature at -170°C during imaging minimizing electron beam damage. This results in previously unattainable imaging resolution and insight into the crystallography of Li dendrite growth and the effects of electrolyte chemistry on SEI.

However, this technique alone is limited to very thin specimens (<100 nm) deposited onto TEM grids, preventing analysis of traditionally prepared and cycled bulk materials. Therefore, we explore the ability of cryogenic focused ion beam (cryo-FIB) to process bulk lithium metal structures for advanced characterization. FIBs are versatile instruments for milling, imaging, and deposition used primarily for transmission electron microscopy (TEM) specimen preparation. Nevertheless, there are major concerns with FIB techniques due to surface damage, redeposition, and preferential sputtering at high current density.[199] Ion milling requires considerable ion beam/sample elastic collisions to transfer kinetic energy and eject material from the sample. Lithium metal due to its low melting temperature, density, thermal conductivity, and shear modulus is especially sensitive to deleterious cascade effects such as Ga-ion implantation.[105]

We demonstrate not only the importance of cryo-FIB for handling sensitive materials, but also elucidate the impact of electrolyte and additive selection in the density and morphology of plated lithium, which directly impacts long term cycling performance. We further extend cryo-FIB to process and analyze TEM lamella of lithium metal and lithium metal solid-state batteries.

7.2 Experimental

7.2.1 Cryogenic Focused Ion Beam

Samples were mounted on a 12.7 mm diameter SEM stub (Ted Pella) in a glovebox (O_2 and H_2O < 1ppm) then transferred at room temperature to a FEI Scios Dualbeam equipped with a CryoMat integrated cryo-stage and air-free quick loader (FEI). To improve sample conductivity and reduce curtailing artifact during FIB milling the samples were first coated with organometallic platinum using the gas injection system operated at room temperature. For baseline comparisons, samples were milled using standard room temperature FIB conditions at 30 kV and various currents. For cryogenic experiments, at high vacuum (~10^{-6} mbar) the samples were cooled down to -170°C and maintained under continuous liquid nitrogen cooling during SEM imaging and FIB operation. After experimental protocols, samples were brought to room temperature and transferred directly from high vacuum to inert environment via the air-free quick loader (FEI) and stored in a glovebox until further analysis. For 3D reconstructions FIB data was collected using FEI Auto Slice and View Software and analyzed using Avizo software.

7.2.2 Electrochemical Sample Preparation

The electrolytes were prepared using Lithium bis(fluorosulfonyl) imide (LiFSI Oakwood Products, Inc.-battery grade (>99%)), Lithium (trifluoromethanesulfonyl) imide (LiTFSI BASF-battery grade), lithium hexafluorophosphate ($LiPF_6$ BASF-battery grade), dimethoxyethane

(DME, BASF-battery grade), ethylene carbonate (EC, BASF-battery grade), and ethylmethyl carbonate (EMC, BASF-battery grade). All lithium salts were dried under vacuum for 24 hours and the solvents were dried using molecular sieves for 72 hours prior to making the electrolytes (moles of salt/volume of solvent). Seven salt-solvent electrolyte compositions were used in this work: 4.0M LiFSI-DME, 4.0M LiFSI:2.0M LiTFSI-DME, and 1.0M $LiPF_6$ EC: EMC (3:7 wt). All electrolyte solvents and solutions were stored and handled in an argon-filled Vacuum Atmospheres Nexus One glovebox with measured levels of O_2 and H_2O < 1ppm.

Copper foil was cut into ½ inch diameter disks (1.27cm^2) and washed in 1.0M HCl solution for 10 minutes. The Cu disks were rinsed with deionized water (three times) and acetone (three times), dried under vacuum for 12 hrs. The washed Cu foil was assembled in the coin cell as the working electrode while the Li metal (1.5mm thick, FMC Corp) was the reference and counter electrode. Asahi Kasei C5 was used as the separator and soaked in 120 µL of electrolyte. The cells were first discharged until they reached an area capacity of 0.5mAh/cm^2 (plated sample) and charged until reaching 1.0V (stripped sample). The deposited Li metal on Cu foil were disassembled and washed with anhydrous DMC in the glovebox.

7.2.3 Cryogenic Transmission Electron Microscopy

FIB prepared TEM lamellae on Cu Omniprobe grids were loaded in a covered cryogenic dewar with continuous Ar flow. The holder was pumped down to 10^{-5} bar and quickly loaded into a vacuum-transfer chamber, where it remained under vacuum to be cooled to 100 K before introducing it to the microscope for viewing.[214] Micrographs were recorded on a JEOL JEM-2100F TEM with cryo-pole-piece, cold stage, and Gatan K2 direct detection camera, and OneView camera operated at 200 kV.

7.3 Results and Discussion

7.3.1 Focused Ion Beam

Using standard room temperature FIB conditions, commercial Li foils were milled with the ion beam normal to the sample surface using cross-sectional and cross-sectional cleaning procedures at 30 kV and various currents (**Figure 7.1**). At a relatively high milling current of 5 nA there are affects from local melting and quenching along with redeposition, resulting in artificial features and porosity. Counterintuitively, reducing the mill current does not improve these defects and at 1 nA the ion bombardment energy is not sufficient to induce milling at reasonable time rates.

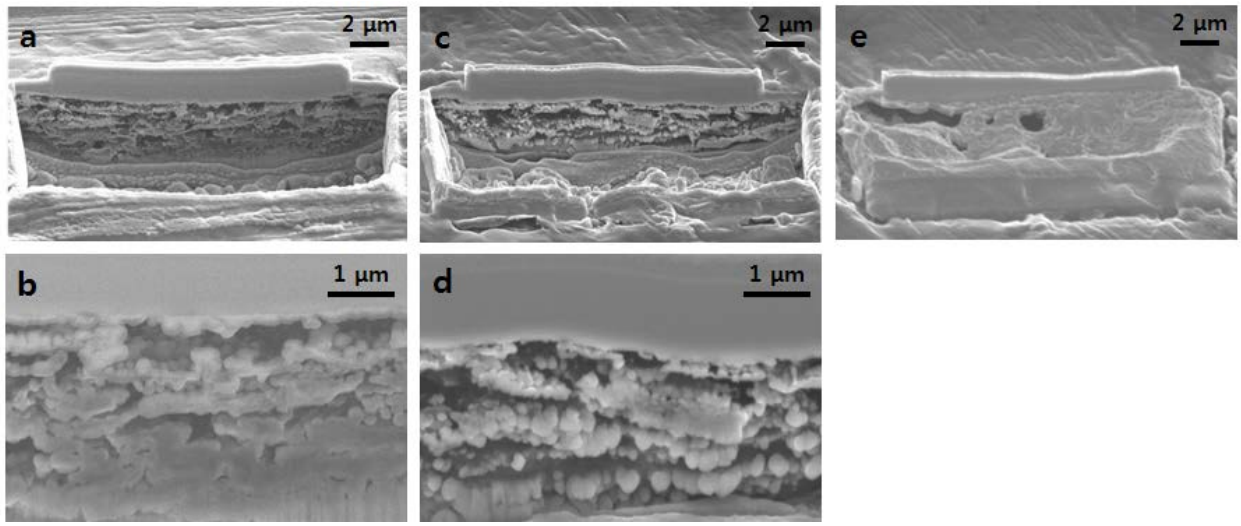

Figure 7.1. SEM image of cross-sections of commercial Li metal foil after standard room temperature FIB cross-sectional cut using (a-b) 5 nA, (c-d) 3 nA, and (e) 1 nA followed by a .5 nA cross-sectional cleaning cut.

Gallium liquid metal ion sources (LMIS) are the most prevalent in FIB instruments due to its low melting temperature (29.8°C at standard atmospheric pressure) and its low volatility.

However, some materials show sensitivity to the Ga^+ ion beam resulting in changes to the structure and chemical composition upon exposure. When the energetic ion hits the sample surface, kinetic energy is lost through ion-solid interactions resulting in a combination of backscattering (imaging), electron emission, electromagnetic radiation, implantation, sputtering, sample damage, and sample heating.

To model Ga^+ ion penetration, Monte Carlo simulations with the TRIM software package were used to calculate penetration profiles and kinetics.[216] Ions at 30 keV were bombarded at various degrees into samples of copper, silicon, and lithium (**Figure 7.2**). Lithium due to its low density and melting temperature has a low stopping power so Ga^+ ions have a significantly longer implantation depth. Sputtering is a surface phenomenon, so this longer penetration depth reduces the sputtering yield. As the incidence angle increases the ion beam/sample interaction area increases resulting in greater collision cascades and increased sputtering yield. Surprisingly, at high angles the sputtering yield of Li drastically increases surpassing both Cu and Si. Previous calculations of higher atomic number materials result in sputtering yield proportions that are invariant to incident angle.[105] Further, the incorporated Ga atom fraction at steady state is inversely proportional to sputtering yield, so this high sputtering yield at glancing angles indicates that there should be minimal deleterious effect from Ga implantation during cleaning cuts, but major contamination during the initial cross cuts. This suggests that implantation effects can be minimized if samples are prepared at grazing angles, but such techniques greatly limit experimental procedures and cannot be implemented for TEM lift-out sample preparation. In addition, even at these high angles there is still significantly more Ga contamination in Li compared to materials such as Cu and Si.

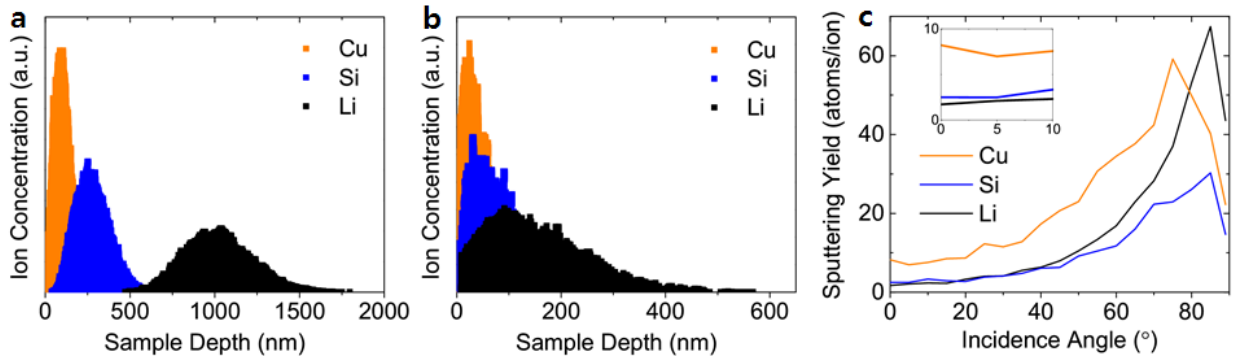

Figure 7.2. TRIM ion trajectories and penetration depth for 30 keV Ga^+ ions implanted at (a) 0° and (b) 89° along with the resulting (c) sputtering yields for various incidence angles.

Another significant side effect from the ion-solid interaction to consider is local heating. The simplest model uses the formalism from laser heating to calculate stationary FIB irradiation.[217] To calculate the maximum temperature increase we neglect all power losses via sputter, lattice damage, electron emission, and ion backscattering and we assume energy loss to nuclear and electronic stopping power contribute to local heating. The maximum temperature increase for a stationary circular beam is

$$\theta_{MAX} = \frac{I\,V}{\sqrt{\pi}\,\kappa\,d} \tag{7.1}$$

where I is the beam current, V is the beam voltage, κ is the thermal conductivity, and d is the beam diameter. It is difficult to measure the FIB beam spot size, as it is limited by the chromatic aberration from energy broadening due to space charge effects at the ion source and the column, but can go down to ~5 nm.[106] Given the relatively high voltage, currents, and aperture size used in the system we will approximate the beam diameter from 50-100 nm and to determine the temperature increase for various materials (**Figure 7.3**). Values for Si are in good agreement with previous work.[217] Li metal has a relatively high thermal conductivity and the local

temperature should only increase ~10-20°C milling at 5 nA currents. However, this simplistic thermal model neglects phenomena due to Ga implantation, defect formation, redeposition, and mechanical deformation. For example, although local heating is minimal, Si is prone to FIB surface amorphization and certain Cu crystallographic directions can form a Cu_3Ga phase. Given the significant Ga implantation depths (**Figure 7.2**) there is likely the formation of new G and O containing species which can alter properties such as heat diffusivity and melting temperature.[197]

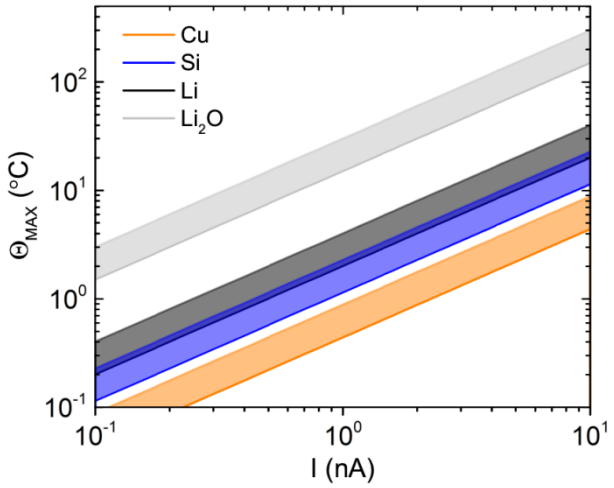

Figure 7.3. Maximum local increase in temperature for Cu, Si, Li, and Li_2O bulk samples exposed to 30 kV FIB at room temperature.

FIB ion-solid interactions are further complicated beyond ion range, sputtering, and heating calculations due to the non-linearity of site specific and scanning milling, which means the physical interactions above and below the surface cannot be approximated as a planar surface. At the boundary conditions of these 3D surface features there are variations in in fundamental sputtering properties such as ion cascades and heat transfer which can significantly alter sputtering yield and local temperature. For example, when imaging and thinning high aspect ratio samples such as TEM lamellae, the sample geometry limits heat transfer, which can further increase local temperatures even for reduced energy beam conditions.[106, 217]

7.3.2 Cryogenic Focused Ion Beam

Cryo-FIB, primarily developed for preparing biological samples for cryo-TEM[218], aims to minimize thermal damage and redeposition to preserve sensitive materials while maintaining high speed milling and functionality. **Figure 7.4** outlines the key components of a cryo-FIB system where the sample is in thermal contact with a liquid nitrogen source. Once the system is stabilized cryogenic temperature can be maintained for several hours. Using standard room temperature milling processes, the commercial Li foil exhibits significant affects from local melting and quenching along with Ga and O contamination. Cleaning this surface at cryo temperatures helps minimize the Ga and O contamination, but morphological distortions penetrate several hundreds of nanometers into the sample, creating redepostion traps. Only when the entire milling process is done using cryo-FIB at -170°C are the deleterious side effects minimized to observe a dense, uniform, pristine Li foil (**Figure 7.5** and **Figure 7.6**).

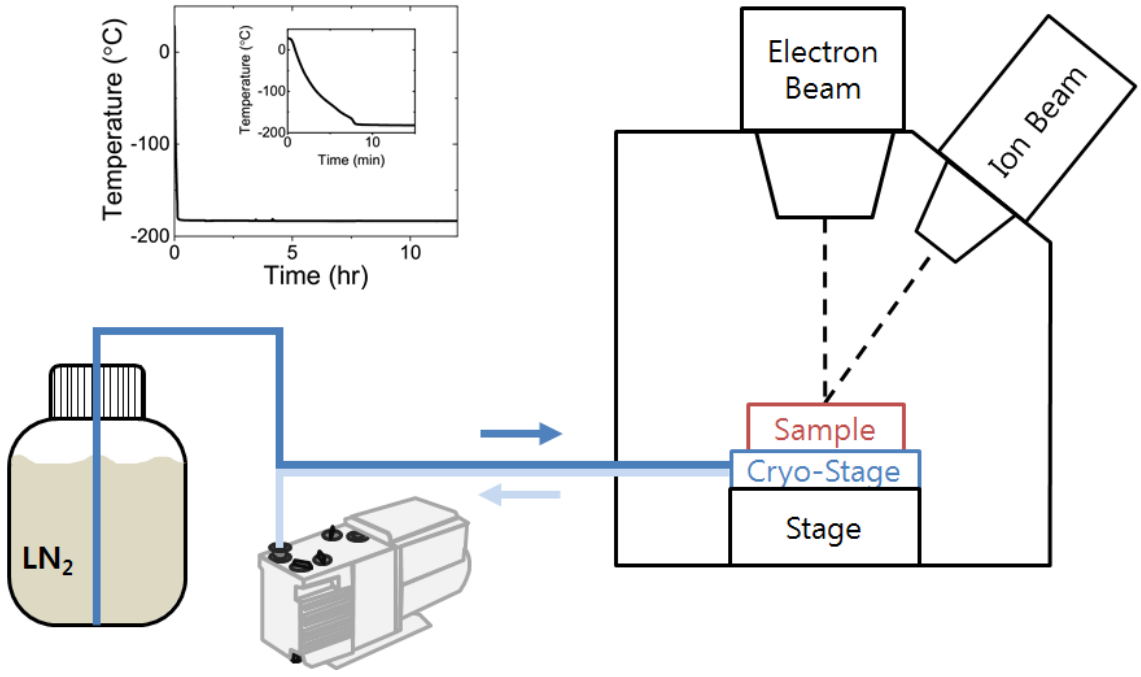

Figure 7.4. Operating principle of cryogenic focused ion beam system maintaining sample temperature at -170°C during ion beam milling and electron beam imaging.

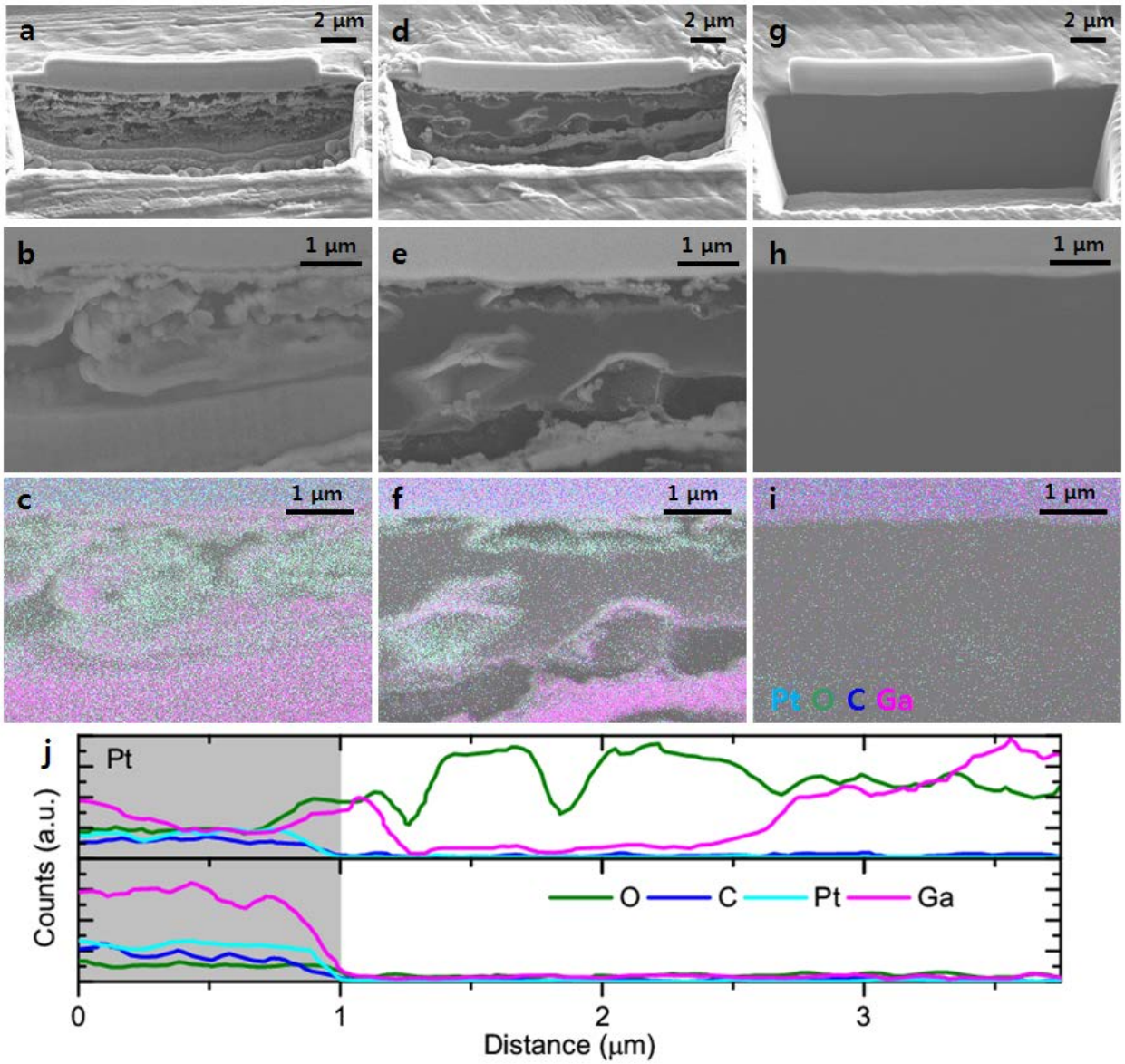

Figure 7.5. SEM images and EDS elemental mapping of cross-sections of commercial Li metal foil (a-c) cross-sectioned and cleaned at room temperature, (d-f) cross-sectioned at room temperature and cleaned at cryogenic temperature, and (g-i) cross-sectioned and cleaned at cryogenic temperature. (j) Quantitative elemental line scans through room temperature (top) and cryogenic temperature (bottom) cross-sections.

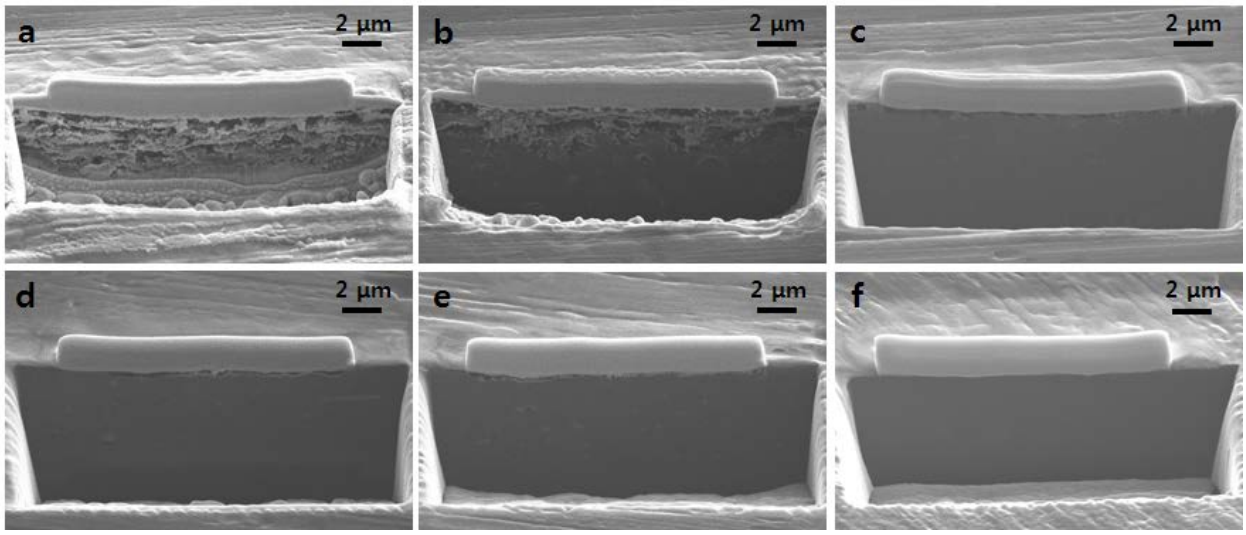

Figure 7.6. SEM images of cross-sections of commercial Li metal foil after FIB cross-sectional cut and clean at (A) room temperature, (B) 0°C, (C) -50°C, (D) -100°C, (E) -150 °C, and (F) -170°C.

7.3.3 Statistical Analysis of Electrochemically Deposited Li Metal

FIB cross-sections are often employed in Li metal battery studies to correlate performance with plating morphology and density, but there must be great efforts to decouple electrochemical phenomena and artifacts from processing. While the sample milled using traditional room temperature processes appears analogous to previous representations of mossy lithium, using cryo-FIB the bulk dendritic features are preserved (**Figure 7.7**). At room temperature the core lithium metal is likely more sensitive to local evaporation, leaving behind a network of SEI components, which have higher melting points, and various redeposited damaged compounds. This method also avoids mechanical deformation associated with “cutting” methods (i.e. microtome, scissors, etc.), thereby obtaining a true representation of the bulk film.

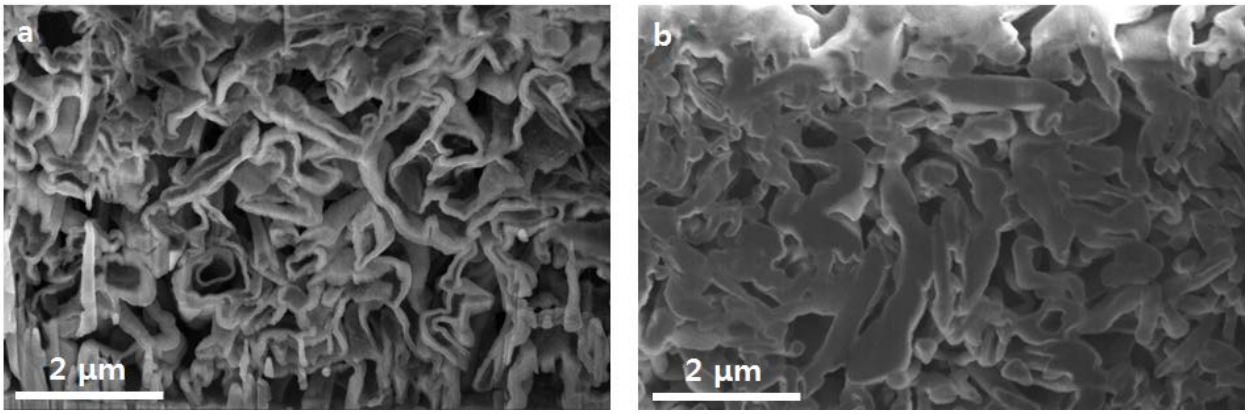

Figure 7.7. SEM image of cross-sections of electrochemically deposited Li in 1.0M LiPF6 EC: EMC electrolyte after FIB preparation at (a) room temperature and (b) cryogenic temperature.

There has been significant effort to develop and engineer new electrolytes to enable Li metal anodes for lithium-ion batteries, with the goal of reducing chemical and morphological inhomogeneities and improving plating/deplating efficiencies >99.9%. Further, next generation lithium metal batteries will require a cathode that demands a voltage stability window beyond the upper stability limit achieved by previously published ether-based or carbonate systems. Recently, inspired by recent progress with increasing salt concentration (>3M) and using multiple salts in basalt combinations, high concentrations of LiFSI and LiTFSI in DME have been shown to improve Li plating efficiency while expanding the stability window to enable $LiNi_{0.6}Mn_{0.2}Co_{0.2}O_2$ (NMC-622).[63, 219] The plating efficiency of bisalt ether electrolyte ("**BSEE**", 4.6m LiFSI + 2.3m LiTFSI in DME), the concentrated single salt ether electrolyte ("**SSEE**", 4.6m LiFSI-DME), and a carbonate baseline ("**Gen II**", 1.0m $LiPF_6$ EC/EMC 3:7) was tested in Li vs Cu coin cells at 0.5 mA/cm^2 to an areal capacity of 0.5 mAh/cm^2 with the intent of simultaneously gauging both chemical and electrochemical stability over long term cycling (**Table 7.1**).[219] The ether-based electrolytes exhibited significantly higher initial efficiencies than the carbonate-based electrolyte.

Table 7.1. Coulombic efficiency of Li vs. Cu cells with different electrolytes.

Coulombic Efficiency (%)	Gen II	SSEE	BSEE
1st Cycle	55%	82%	82%
100th Cycle	77%	98.5%	98.8%

Due to the extreme chemical/electrochemical reactivity of lithium metal, the morphology and packing density of plated lithium are key factors that have a critical impact on cell efficiency and lifetime because they define the true surface area of the reactive Li-electrolyte interface. Some insight regarding the effects of certain cycling parameters (primarily the cycled Li capacity and current density) on growth morphology has been established[220], but the influence of electrolyte composition and the underlying mechanisms for interphase formation and maintenance still generally remain a mystery. Despite this, the impact of electrolyte chemistry is obvious. SEM images of cryo-FIB cross-sections of the plated films were generated to examine the bulk plating behavior and examine the Li-Cu interface. For the lithium plated with the carbonate baseline, the film has a continuous, highly porous network with lithium metal branching and significant void spaces at the Li/Cu foil interface propagate throughout the film, with a thickness ~6 μm (**Figure 7.8.a**). This is consistent with previous results and eventually leads to catastrophic cell failure.[221, 222] For the SSEE, the porosity in deposited Li is reduced, with no observable dendritic Li, but some pores throughout the film and interface, and a thickness ~4 μm (**Figure 7.8.b**). In contrast to these systems, the lithium film plated with the BSEE exhibits a drastic improvement in film density and a reduced plated layer thickness of only ~2.5 μm (**Figure 7.8.c**).

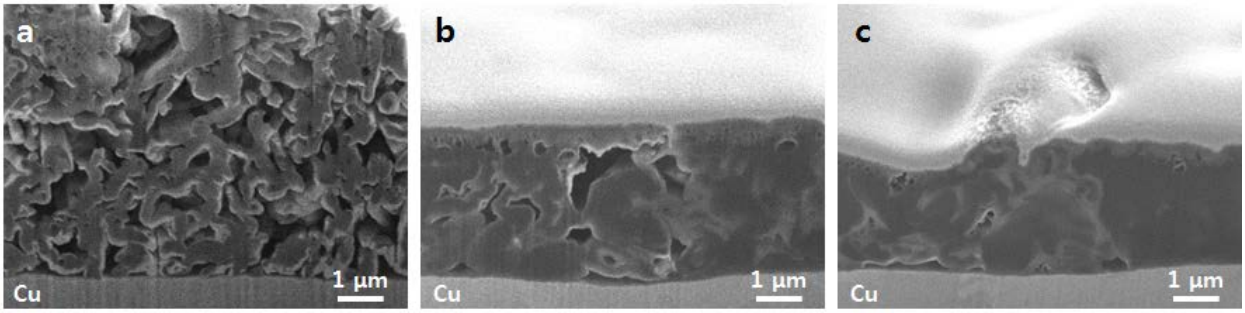

Figure 7.8. SEM cross-section of electrochemically deposited Li under 0.5 mA/cm^2 to an areal capacity of 0.5 mAh/cm^2 in (a) 1.0M LiPF6 EC: EMC (Gen II), (b) 4.6m LiFSI-DME (SSEE) (c) 4.6m LiFSI + 2.3m LiTFSI in DME (BSEE).

Although this kind of qualitative analysis is powerful for elucidating the trends in correlating morphology, packing density, and electrochemical performance, these are still highly local observations and may not accurately represent the global average. With limitation in mind, we collected a series of high resolution SEM cross-sectional images as we sequentially milled through a large area parallel to the current collector (**Figure 7.9**). For each region of interest, gray scale intensity values were assigned to different elements and quantified using Amira-Avizo software (**Figure 7.10**).

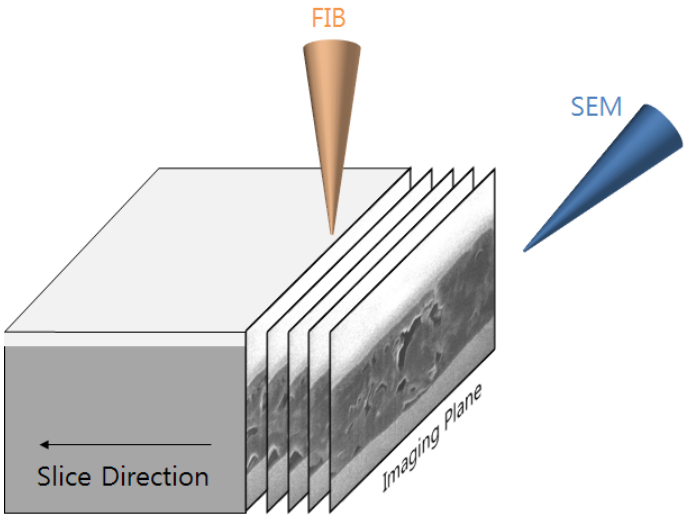

Figure 7.9. Schematic of FIB-SEM slice and view methodology for 3D reconstruction.

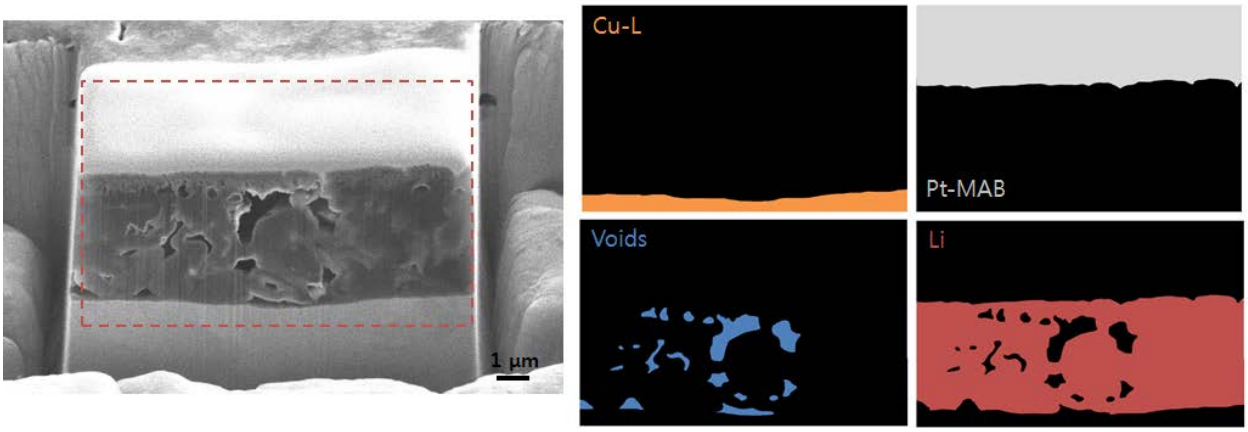

Figure 7.10. Schematic of gray scale histogram element segmentation for 3D reconstruction.

Stacking a series of 2D images, we can create 3D reconstructions of electrochemically deposited Li were created to quantify a large total volume of sample to obtain microstructural statistical information (**Figure 7.11.a-f**). We observe not only the total packing density of Li, but also the size, shape and distribution of voids. In agreement with the trends extracted from the single cross-sectional images, Li deposited in Gen II carbonate electrolyte has dendritic growth and a large network of evenly distributed and connects pores. Li deposited in SSEE and BSEE as significantly more dense. Further, we can quantify the total volume of various components and the surface area between each phase. And with this information extract more precise values to quantify the quality of plated Li. While each sample has the same total quantity of Li plated, the electrolyte chemistry will influence the plating kinetics. Li plated in Gen II carbonate electrolyte has an average thickness of 6.7 µm and 83% packing density. Li plated in high concentration SSEE has a reduced average thickness to 3.7 µm, but only a marginally better packing density of 86%. While the deposited Li is much smoother with no dendrites, there are still large voids throughout the film and at the Cu/Li interface. Li plated in the BSEE is the thinnest and densest film. Most importantly, we can now quantify the true Li metal/electrolyte interface, which will

determine SEI surface area (i.e. the area of parasitic side reactions). This suggests a synergistic mechanism between LiFSI and LiTFSI in generating more uniform Li nucleation and deposition, particularly at the Li-Cu interface.

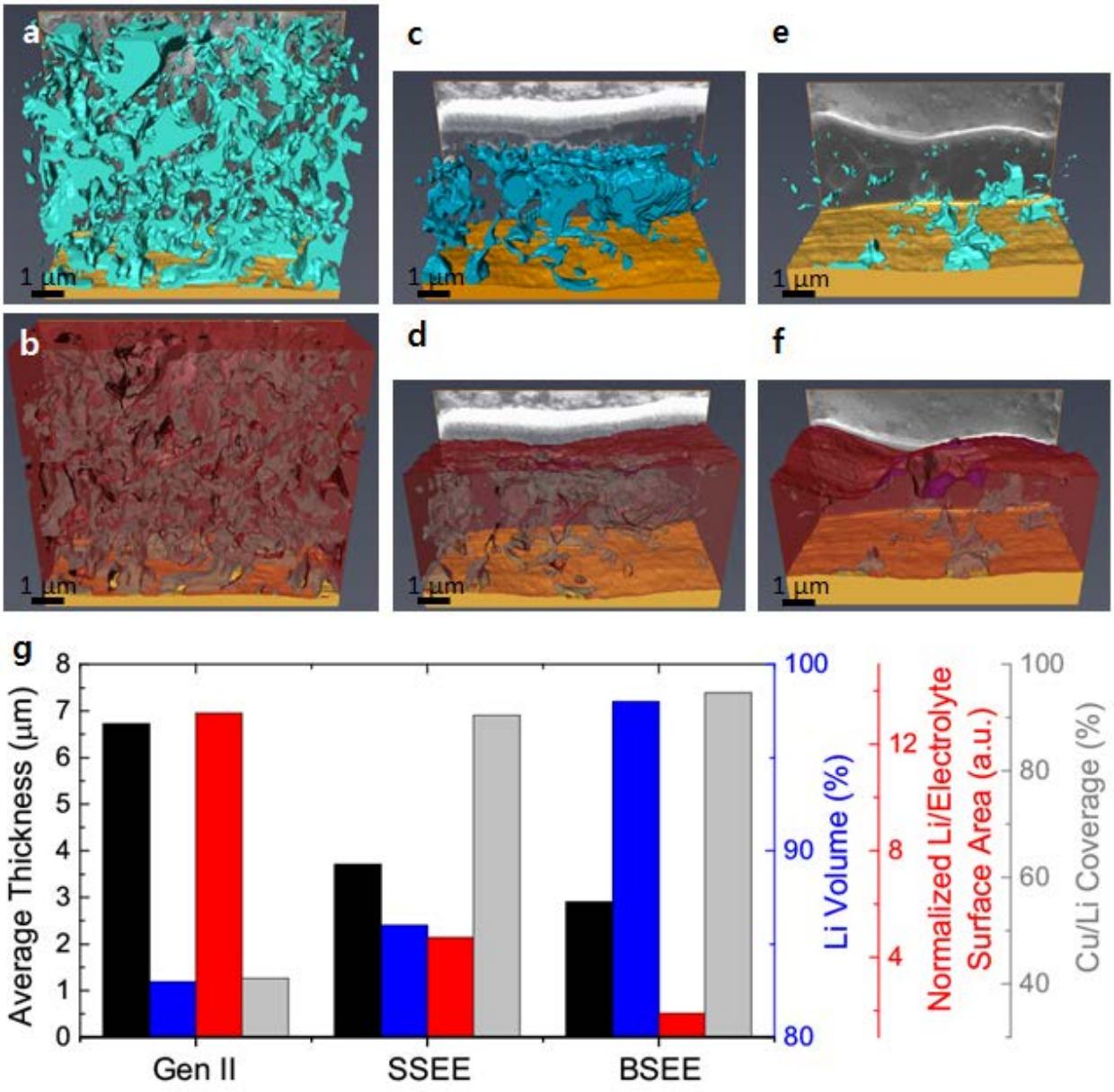

Figure 7.11. 3D morphology reconstruction of voids (blue) and bulk Li metal (red) of 1st cycle electrochemically deposited Li in (a-b) 1.0M LiPF6 EC: EMC (Gen II), (c-d) 4.6m LiFSI-DME (SSEE), and (e-f) 4.6m LiFSI + 2.3m LiTFSI in DME (BSEE) along with (g) statistical analysis.

7.3.4 TEM Sample Preparation

With the goal of enabling cryo-TEM analysis of Li metal anodes and the Li/solid-state electrolyte interface, drawing on our expertise we developed a process to use cryo-FIB to prepare TEM lamellae of Li metal and Li metal batteries. Li metal is very sensitive, but with careful control of beam conditions, chamber vacuum, and sample temperature we process a TEM lamella from a commercial Li foil. Our key challenge is that traditional lift-out and sample mounting is done with a Pt gas injection system (GIS), which is not compatible with cryo-FIB. Therefore, during the mounting step, the sample must be brought to room temperature, and then cooled down again for thinning. While the sample is at room temperature, any electron or ion beam/sample interactions must be minimized to reduce damage. **Figure 7.12.b** is an example of an improperly processed Li foil damaged regions. If there is excess energy (i.e. beam dwell time, beam current, etc.) there will be visible defects in the Li metal, such as voids or recrystallized droplets. If properly process, the lamella can be thinned to <100 nm (**Figure 7.12.c**). All milling was performed at an ion beam voltage of 30 kV. Trenches to form the initial lamella were milled with a beam current of 5 mA, followed by cleaning and lift out at 1 nA. Thinning of the lamella was first conducted with a beam current of 500 pA, decreasing with lamella thickness to a final thinning with tens of pA. Once the lamella has been prepared, the sample is brought back to room temperature, removed from the FIB under vacuum using an air-free quick loader (FEI), and stored in an Ar purged glovebox. Transfer into the TEM and cooling of the lamella was carried out using techniques described previously.[214] TEM analysis confirms that the Li foil maintains its polycrystalline structure during the cryo-FIB sample preparation process, but there is significant surface oxidation. This is likely due to the room temperature sample transfer process, as even low vacuum and glovebox environments have trace amounts of oxygen, and the lamella has an

increased surface area to volume ratio. Going forward, it is best to maintain the sample at cryogenic temperatures during transfer to minimize these reactions.[223]

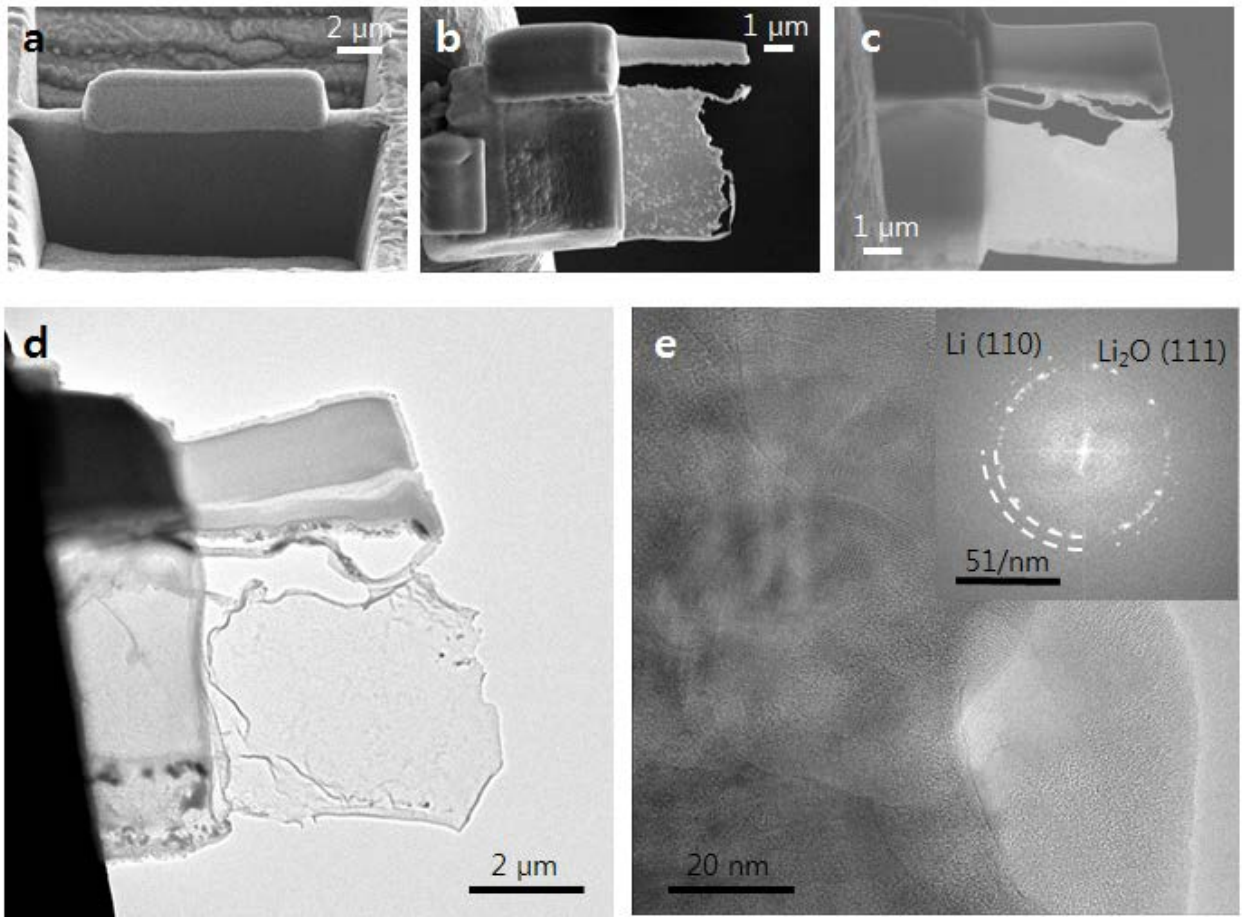

Figure 7.12. SEM image of Li foil after (a) trench milling, (b) damaged during lift-out, and (b) properly processing to creating a TEM lamella. (d-e) Cryo-TEM image with corresponding FFT analysis.

Further, cryo-FIB can enable analysis of commercial LCO/LiPON/Li metal thin-film batteries supplied by STM Microelectronics. Using cryo-FIB we can initially cross-section the battery to clearly identify the dense layers of 6.5 µm LCO cathode, 2.0 µm LiPON electrolyte, and 5-10 µm Li anode with smooth and conformal interfaces (**Figure 7.13.a**). After cryo-FIB cleaning, the respective battery layers are still intact and identifiable with EDS elemental

mapping. After a catastrophic event such as crushing or rupture causing the battery to short, there is significant porosity at the Li/electrolyte interface and growth of the disordered LCO layer, both indicative of increased interfacial resistance and poor cell performance (**Figure 7.13.b**).[103, 208] Lamellae were prepared via a modified lift-out technique to protect the Li metal during mounting. These lamellae can them be thinned until the desirable components are electron transparent (**Figure 7.13.c**). The key challenge is to consider and balance the chemical, thermal, electrical, and mechanical properties of all the components, which will influence their interaction with and behavior under the ion and electron beams. Afterwards, these samples can be transferred to a TEM for structural and chemical analysis.

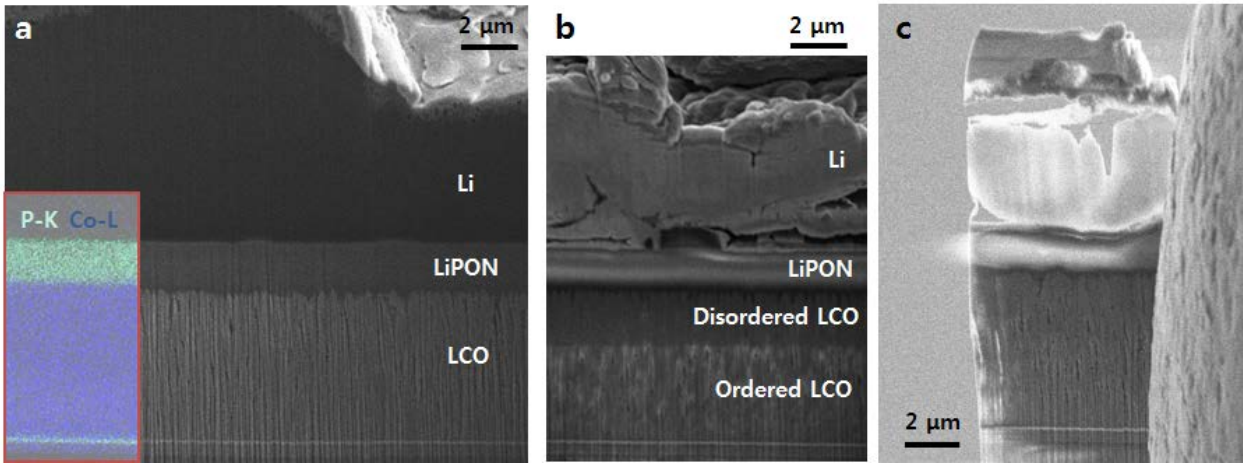

Figure 7.13. (a) SEM image and EDS elemental map of cross-section of pristine Li metal thin film battery. (b) SEM image of sample after shorting. (d) TEM lamella of commercial Li metal thin film battery to enable future studies of Li metal/electrolyte interfaces.

7.4 Conclusion

In this work, we demonstrate the importance of cryo-FIB for processing and characterizing sensitive battery materials. Using standard processing conditions at room

temperature, lithium metal is prone to damage from Ga implantation and local heating. 3D reconstructions enable statistical analysis to characterize the impact of electrolyte and additive selection in the density and morphology of plated lithium, which directly impacts long term cycling performance. Further, we extend cryo-FIB to process and analyze TEM lamella of lithium metal and lithium metal solid-state batteries, which when coupled with cryo-TEM have the potential to elucidate the complex structural and chemical phenomena at Li metal/electrolyte interfaces.

This chapter in full, is currently being prepared for submission for publication "Cryogenic Focused Ion Beam Characterization of Lithium Metal Anodes for Li-Ion Batteries," J.Z. Lee, T.A. Wynn, J. M.A. Schroeder, J. Alvarado, X. Wang, K. Xu, and Y.S. Meng. The dissertation author was the primary investigator and first author of this paper. All the experiments and writing were done by the author expect for the electrochemical sample preparation and transmission electron microscopy data collection.

Chapter 8. Summary and Outlook

The future of electrochemical energy storage depends on the concurrent advancement of constituent component materials and their satisfactory interaction with one another. We primarily look to (1) increase the energy and power density of electrochemical cells through increasing electrode capacity, and (2) remove the chemical energy available for release during device failure, as present in modern flammable organic liquid electrolytes used in lithium-ion batteries.[224] Solid-state electrolytes (SSEs) may satisfy both these requirements, serving as a safe replacement for their organic liquid counterparts, while potentially enabling alkali metal anodes. However, there are still significant scientific and engineering hurdles before the full potential of SSEs can be realized: primarily performance degradation from chemical and mechanical instability at grain boundaries and electrode/electrolyte interfaces. Despite the importance of these interfaces in the functionality of next-generation solid-state devices, there are surprisingly few studies focused on characterization of their interfaces.

The focus of this thesis was to use solid-state thin film battery materials and devices as a model system for fundamental studies of bulk and interface properties because of their well-defined geometry and controlled chemical composition, eliminating any effects from polymeric binder or conductive agents. To date, the only successfully commercialized solid state battery chemistry is thin film devices based on and lithium phosphorous oxynitride (LiPON) electrolyte, which has demonstrated up to 10,000 cycles when paired with both a high voltage cathode and lithium metal anode.[113] This is often attributed to the thermodynamic stability of the LiPON/Li interface and its mechanical stiffness. We using nanoindentation in controlled physical environments that reflect the minimized exposure to ambient humidity for solid electrolyte use in

solid state batteries, and we show that this material exhibits mechanical stiffness that is surprisingly lower than reported previously by two orders of magnitude. This challenges the concept that high material stiffness is a key parameter required of LIPON solid electrolytes to block lithium (Li) dendrite growth.

LiPON, although the most popular thin film electrolyte, suffers from low ionic conductivity (~10^{-6} S/cm) and is susceptible to electron beam damage in the TEM.[207] Further, with many crystalline solid oxide electrolytes susceptible to lithium dendrite penetration at grain boundaries, mechanical homogeneity is looked to as one form of dendrite growth prevention. Amorphous lithium lanthanum titanate (a-LLTO) was explored using pulsed laser deposition (PLD). Optimization showed that both oxygen partial pressure and film thickness played a critical role in the performance of the thin film electrolyte. DC polarization measurements suggest that below a critical film thickness electronic leakage is prevalent. The a-LLTO was characterized via STEM-EELS, showing the expected composition and structure, and temperature controlled EIS, showing conductivity on the order of 10^{-4} S/cm. Interestingly, the film cross-section appeared to be largely unaffected by the electron beam, showing no signs of mechanical or chemical degradation—such a material would be an ideal candidate for future exploration of electrode and interface dynamics via STEM/EELS.

While there have been significant research efforts to improve the ionic conductivity of solid-state electrolytes and the electrochemical performance of all-solid-state batteries, however, the root causes of their poor performance—interfacial reaction and subsequent impedance growth—are poorly understood. This is due to the dearth of effective characterization techniques for probing these buried interfaces. Electrochemical *in situ* experiments involve the design and fabrication of electrochemically active devices, with an ultimate goal of elucidating links

between state of charge and the nature of the interface, yet very few techniques have been successfully developed with this capability. Therefore, we explore focused ion beam (FIB) as a tool to enable morphological, structural, and chemical analysis of solid-state thin film batteries. With careful control of ion beam power we can minimize damage to an LCO/LiPON/a-Si thin film battery and fabricate an electrochemically active nanobattery. With proper circuit design, we can minimize the electrical noise inside of a vacuum FIB system down to tens of picoamps for *in situ* cycling. Non-optimized systems will be rich with leakage pathways for electrons, preventing the necessarily low current from passing solely through the nanobattery.

Despite the importance Li metal anodes play in increasing energy densities of next-generation electrochemical cells, methods for structural characterization have been limited until recently. There are many reasons for this, including Li metal's high reactivity, forming native oxides under environments controlled to below ppm of oxygen and moisture**,** and its susceptibility to melting/sublimation under exposure to high-energy probes. Inspired by recent work using cryogenic transition electron microscopy (cryo-TEM) to image electrochemically deposited nanoscale lithium, we demonstrate cryogenic focused ion beam (cryo-FIB) as a potentially powerful tool for keeping sensitive samples at temperatures low enough to counteract local heating and deleterious side effects during exposure to electron and ion beams. Room-temperature melting has been shown to drastically alter lithium morphology, obscuring the nature of lithium stripping and plating, and rendering the Li-metal/SSE interface unstable. With cryo-FIB we can create site specific high-quality TEM lamella, which can then be analyzed with cryo-TEM. The next step would be to apply such cryo-TEM analyses to the Li/SSE interfaces, but we highlight the importance of complete environmental isolation of the FIB-prepared sample from milling to insertion into the TEM—a markedly difficult task.

Having developed a robust *in situ* testing configuration utilizing thin film batteries, FIB, and TEM, we look to increase exploration of a range of materials systems and interfaces to elucidate the dynamic behavior and guiding principles to reduce interfacial resistance at the buried electrode/electrolyte solid-solid interface, with the goal of enabling simultaneous structural and chemical characterization as a function of state of charge. The most striking aspect of the development of solid-state electrolytes is the limited number of studies devoted to explaining poor materials compatibility. Understandably, the degree of incompatibility was only recently called into question in a host of DFT studies, and similarly due to the complexity of analysis of these systems. These materials are inherently reactive under ambient conditions, often shrouding the true electrochemical modifications present. While thermodynamic stability is in question in many compounds, kinetics of decomposition serves as a further variable, likely resulting in discrepancies between theory and experiment. Only through the application of *in situ* methodologies can we capture the dynamic and heterogeneous nature of interfaces, preventing environmental effects from taking hold, and further preventing electrochemical relaxation when the device is removed from biasing.

Electron microscopy at the present time is the only method capable of collecting structural and chemical information under electrochemical stimulus for solid state interfaces. Advancement of *in situ* and *operando* electron microscopy methodologies requires further development in the current state of the art, reducing beam-material interaction induced damage while improving spatial and temporal resolution during data acquisition. Use of high-energy probes is accompanied by many practical considerations, primarily beam damage effects. High-energy electrons damage materials through radiolysis (decomposition due to ionizing radiation), primary knock-on damage, and local heating effects.[225]

Solid electrolytes are out of necessity and are often amorphous, and as such are generally susceptible to thermally degradation. Traditional methods of combating heating effects, such as carbon coating, are incompatible with *in situ* biasing (i.e., device shorting), but rather require fine control of the experimental design by limiting electron dose and selecting more robust electrolytes. It is noted in works of Santhanagopalan[207] and Wang,[208] and similarly by the community of electron microscopists,[226] that the electron dose is of critical importance both for the stability of the materials being probed and in the interpretation of electronic probe outputs, and should be recorded and reported carefully. Selection of electrolytes that are more robust to beam exposure, such as oxides LLTO or LLZO, will enable quantitative observation of dynamic cathodic/anodic behaviors.

Beyond damaging effects, electron probes also have the potential to alter the total current injected into the battery. Revisiting the length scale of nanobatteries, the necessarily small cross section required for TEM analysis demands similarly low currents to promote reasonable electrochemical behavior. For example, a dense $LiCoO_2$ nanobattery with a cross section of 10 μm^2 and cathode thickness of 2 μm demands a current on the order of 10 pA to achieve a cycling rate of 1 C, though lower charge rates are required for systems with sluggish kinetics or large interfacial transfer impedance. While this current may be on the order of magnitude of STEM probe currents, the likelihood of the electron probe interacting with the electrochemical probe is minimal due to the low degree of internal scattering; however, the degree of scattering is dependent on the material density and the sample geometry. Currents below the pA range may be impacted by electromagnetic noise within instruments, and reduced current testing within a TEM is currently being evaluated.

Improved detector acquisition rates have the potential to capture reconstruction in solid-state interphases, as in the case of atomically resolved grain-boundary dynamics reconstructions.[227] Direct-detection cameras have further enabled reduced-dose image acquisition, as effectively demonstrated in biological sciences,[228] and will likely be useful in capturing dynamic phenomena in sensitive battery materials. However, such high-speed comes with the downside of yielding overwhelmingly large data sets. Direct detection cameras capable of capturing 24 megapixel images at a rate of 1500 frames per s, producing datasets on the order of terabytes, are nearing the limit of modern hard drive technology. Efficient storage protocol and automated large-data set analysis methods are areas of great interest to the field.

When characterizing nanoscale devices, it behooves the researcher to keep a realistic picture of the nature of the modifications to their device. For example, the reduced in-plane length scale of a nanobattery used in the *in situ* TEM methodologies is notably different from that of its parent device. Fabrication of the nanobattery increases the edge/interface ratio otherwise negligible in a thin-film device. Arguments as to field distribution should incorporate models with geometric considerations, as free surfaces likely alter the equilibrium field distribution through the bulk of the nanobattery.[224] Similarly, kinetic limitations of the electrodes place an upper bound on the applied current densities. Analogous to alkali metal ions' propensity to form dendrites in liquid cells, the presence of an exposed interface may provide a low energy site for nucleation should the conditions present themselves, ultimately resulting in "dead" metal extruding outside of the device; such "dead" material would be rendered largely inactive due to its position outside of the electric field potential. Attempts to bypass the complexities associated with full cell devices include an FIB-assembled nanobattery, with an FIB-thinned $LiCoO_2$ particle as the cathode, FIB lamella of LLZO as electrolyte, and Au anode, all affixed together

using FIB-deposited Pt.[229] While such fabrication methods may provide insight into the dynamic nature of cathode materials under extreme conditions, such construction requires careful evaluation of the input current to make any link between the electrochemical state of a device and the phenomena being observed. In such work, with a cross section required to achieve atomic-scale resolution via conventional TEM, structural change was observed with the application of current on the order of 1 mA;[229] considering the size of the cross section for imaging, this translates to a current density on the order of 10^8 mA/cm^2—in excess of current densities present in conventional devices. Such approximations are necessary, and as long as they are addressed appropriately, they do not limit the impact of the results presented.

Further, studying electrochemical evolution of alkali-metal anodes will in itself require a host of engineering accommodations. Environmental isolation is paramount in the case of alkali metal anode-based batteries, as the reduced dimensions greatly increase the surface-to-volume ratio. Even if environmental isolation can be accomplished, there is the question of stability under the electron beam, which has been demonstrated to be mitigated by cryo-EM techniques. Finally, to apply electrochemical methods requires the *in situ* biasing capabilities demonstrated in past work. However, one may note an inherent incompatibility between cryogenic temperatures and the reduced kinetics of interfacial decomposition at reduced temperatures. While cryo-EM has proven to be very useful, further work is needed to study variability in holder temperature with respect to lithium stability under the electron beam. A researcher could imagine tuning temperatures for (1) lithium/interface stability, (2) interface kinetics, and (3) lithium transport within the device. Conversely, *in situ* heating holders, coupled with *in situ* biasing holders, would promote thermodynamic decomposition, emulating the effect of cycling batteries at elevated temperatures.

References

1. D. Miller, http://clients1.ibisworld.com/reports/us/industry/currentperformance.aspx?indid=4499, 2017.

2. J. Aguilar, https://www.greenoptimistic.com/lithium-market-growth-ev-20171118/#.WlK4fKinFjU, 2017.

3. C. Pillot, http://www.avicenne.com/articles_energy.php, 2017.

4. M. D. Radin, S. Hy, M. Sina, C. C. Fang, H. D. Liu, J. Vinckeviciute, M. H. Zhang, M. S. Whittingham, Y. S. Meng, and A. Van der Ven, *Adv Energy Mater*, **7** (20), (2017).

5. R. Huggins, *Advanced Batteries*, Springer, New York (2009).

6. A. O. Raji, R. Villegas Salvatierra, N. D. Kim, X. Fan, Y. Li, G. A. L. Silva, J. Sha, and J. M. Tour, *ACS nano*, **11** (6), 6362-6369 (2017).

7. G. Zheng, S. W. Lee, Z. Liang, H. W. Lee, K. Yan, H. Yao, H. Wang, W. Li, S. Chu, and Y. Cui, *Nature nanotechnology*, **9** (8), 618-623 (2014).

8. D. Lin, Y. Liu, Z. Liang, H. W. Lee, J. Sun, H. Wang, K. Yan, J. Xie, and Y. Cui, *Nature nanotechnology*, **11** (7), 626-632 (2016).

9. R. Younesi, G. M. Veith, P. Johansson, K. Edström, and T. Vegge, *Energy Environ. Sci.*, **8** (7), 1905-1922 (2015).

10. S.-K. Jeong, H.-Y. Seo, D.-H. Kim, H.-K. Han, J.-G. Kim, Y. B. Lee, Y. Iriyama, T. Abe, and Z. Ogumi, *Electrochemistry Communications*, **10** (4), 635-638 (2008).

11. T. Thompson, A. Sharafi, M. D. Johannes, A. Huq, J. L. Allen, J. Wolfenstine, and J. Sakamoto, *Adv Energy Mater*, **5** (11), 1500096 (2015).

12. J. Z. Lee, Z. Wang, H. L. Xin, T. A. Wynn, and Y. S. Meng, *Journal of the Electrochemical Society*, **164** (1), A6268-A6273 (2016).

13. N. J. Dudney, *Journal of Power Sources*, **89** 176-179 (2000).

14. A. Sharafi, E. Kazyak, A. L. Davis, S. Yu, T. Thompson, D. J. Siegel, N. P. Dasgupta, and J. Sakamoto, *Chemistry of Materials*, **29** (18), 7961-7968 (2017).

15. A. C. Kozen, C. F. Lin, A. J. Pearse, M. A. Schroeder, X. G. Han, L. B. Hu, S. B. Lee, G. W. Rubloff, and M. Noked, *ACS nano*, **9** (6), 5884-5892 (2015).

16. Y. Wang, W. D. Richards, S. P. Ong, L. J. Miara, J. C. Kim, Y. F. Mo, and G. Ceder, *Nat Mater*, **14** (10), 1026-+ (2015).

17. N. Kamaya, K. Homma, Y. Yamakawa, M. Hirayama, R. Kanno, M. Yonemura, T. Kamiyama, Y. Kato, S. Hama, K. Kawamoto, and A. Mitsui, *Nat Mater,* **10** (9), 682-686 (2011).

18. K. Kerman, A. Luntz, V. Viswanathan, Y. M. Chiang, and Z. B. Chen, *Journal of the Electrochemical Society,* **164** (7), A1731-A1744 (2017).

19. J. Z. Lee, Z. Y. Wang, H. L. L. Xin, T. A. Wynn, and Y. S. Meng, *Journal of the Electrochemical Society,* **164** (1), A6268-A6273 (2017).

20. A. Varzi, R. Raccichini, S. Passerini, and B. Scrosati, *J Mater Chem A,* **4** (44), 17251-17259 (2016).

21. J. Maier, *Ber Bunsen Phys Chem,* **93** (12), 1468-1473 (1989).

22. W. D. Richards, L. J. Miara, Y. Wang, J. C. Kim, and G. Ceder, *Chemistry of Materials,* **28** (1), 266-273 (2016).

23. Y. Z. Zhu, X. F. He, and Y. F. Mo, *Acs Appl Mater Inter,* **7** (42), 23685-23693 (2015).

24. K. Kanehori, K. Matsumoto, K. Miyauchi, and T. Kudo, *Solid State Ionics,* **9-10** (Dec), 1445-1448 (1983).

25. K. Miyauchi, K. Matsumoto, K. Kanehori, and T. Kudo, *Solid State Ionics,* **9-10** (Dec), 1469-1472 (1983).

26. J. B. Bates, N. J. Dudney, D. C. Lubben, G. R. Gruzalski, B. S. Kwak, X. H. Yu, and R. A. Zuhr, *Journal of Power Sources,* **54** (1), 58-62 (1995).

27. B. Wang, J. B. Bates, F. X. Hart, B. C. Sales, R. A. Zuhr, and J. D. Robertson, *Journal of the Electrochemical Society,* **143** (10), 3203-3213 (1996).

28. M. Ohring, *Materials Science of Thin Films, 2nd Edition,* Academic Press (2001).

29. C. H. P. Lupis, *Chemical thermodynamics of materials,* North-Holland, Amsterdam (1983).

30. R. Glang, *Handbook of Thin Film Technology,* McGraw-Hill, New York (1970).

31. D. M. Mattox, *J Vac Sci Technol A,* **7** (3), 1105-1114 (1989).

32. P. P. Pronko, S. K. Dutta, D. Du, and R. K. Singh, *J Appl Phys,* **78** (10), 6233-6240 (1995).

33. D. P. Norton, C. Park, J. D. Budai, S. J. Pennycook, and C. Prouteau, *Appl Phys Lett,* **74** (15), 2134-2136 (1999).

34. Y. E. Lee, D. P. Norton, and J. D. Budai, *Appl Phys Lett,* **74** (21), 3155-3157 (1999).

35. H. Xia, Y. S. Meng, M. O. Lai, and L. Lu, *Journal of the Electrochemical Society,* **157** (3), A348-A354 (2010).

36. J. N. Reimers and J. R. Dahn, *Journal of the Electrochemical Society*, **139** (8), 2091-2097 (1992).

37. K. Mizushima, P. C. Jones, P. J. Wiseman, and J. B. Goodenough, *Mater Res Bull,* **15** (6), 783-789 (1980).

38. J. R. Dahn, E. W. Fuller, M. Obrovac, and U. Vonsacken, *Solid State Ionics,* **69** (3-4), 265-270 (1994).

39. A. Van der Ven, M. K. Aydinol, G. Ceder, G. Kresse, and J. Hafner, *Phys Rev B,* **58** (6), 2975-2987 (1998).

40. G. G. Amatucci, J. M. Tarascon, and L. C. Klein, *Journal of the Electrochemical Society,* **143** (3), 1114-1123 (1996).

41. Y. Iriyama, M. Inaba, T. Abe, and Z. Ogumi, *Journal of Power Sources,* **94** (2), 175-182 (2001).

42. R. Huang, T. Hitosugi, C. A. J. Fisher, Y. H. Ikuhara, H. Moriwake, H. Oki, and Y. Ikuhara, *Mater Chem Phys,* **133** (2-3), 1101-1107 (2012).

43. S. I. Cho and S. G. Yoon, *Journal of the Electrochemical Society,* **149** (12), A1584-A1588 (2002).

44. W. G. Choi and S. G. Yoon, *Journal of Vacuum Science & Technology A,* **22** (6), 2356-2360 (2004).

45. M. E. Donders, W. M. Arnoldbik, H. C. M. Knoops, W. M. M. Kessels, and P. H. L. Notten, *Journal of the Electrochemical Society,* **160** (5), A3066-A3071 (2013).

46. V. Patil, A. Patil, J. W. Choi, Y. P. Lee, Y. S. Yoon, H. J. Kim, and S. J. Yoon, *J Electroceram,* **23** (2-4), 214-218 (2009).

47. Y. H. Rho and K. Kanamura, *Journal of the Electrochemical Society,* **151** (9), A1406-A1411 (2004).

48. K. F. Chiu, *Thin Solid Films,* **515** (11), 4614-4618 (2007).

49. S. W. Jeon, J. K. Lim, S. H. Lim, and S. M. Lee, *Electrochim Acta,* **51** (2), 268-273 (2005).

50. C. L. Liao, Y. H. Lee, and K. Z. Fung, *J Alloy Compd,* **436** (1-2), 303-308 (2007).

51. M. M. Thackeray, W. I. F. David, P. G. Bruce, and J. B. Goodenough, *Mater Res Bull,* **18** (4), 461-472 (1983).

52. S. B. Tang, M. O. Lai, and L. Lu, *Electrochim Acta,* **52** (3), 1161-1168 (2006).

53. N. J. Dudney, J. B. Bates, R. A. Zuhr, S. Young, J. D. Robertson, H. P. Jun, and S. A. Hackney, *Journal of the Electrochemical Society,* **146** (7), 2455-2464 (1999).

54. K. F. Chiu, H. H. Hsiao, G. S. Chen, H. L. Liu, J. L. Her, and H. C. Lin, *Journal of the Electrochemical Society*, **151** (3), A452-A455 (2004).

55. P. Liu, J. G. Zhang, J. A. Turner, C. E. Tracy, and D. K. Benson, *Journal of the Electrochemical Society*, **146** (6), 2001-2005 (1999).

56. Y. J. Park, J. G. Kim, M. K. Kim, H. T. Chung, and H. G. Kim, *Solid State Ionics*, **130** (3-4), 203-214 (2000).

57. D. Aurbach, M. D. Levi, K. Gamulski, B. Markovsky, G. Salitra, E. Levi, U. Heider, L. Heider, and R. Oesten, *Journal of Power Sources*, **81** 472-479 (1999).

58. Y. Y. Xia, Y. H. Zhou, and M. Yoshio, *Journal of the Electrochemical Society*, **144** (8), 2593-2600 (1997).

59. R. Benedek, M. M. Thackeray, J. Low, and T. Bucko, *J Phys Chem C*, **116** (6), 4050-4059 (2012).

60. M. Y. Song, D. S. Ahn, and H. R. Park, *Journal of Power Sources*, **83** (1-2), 57-60 (1999).

61. Q. M. Zhong, A. Bonakdarpour, M. J. Zhang, Y. Gao, and J. R. Dahn, *Journal of the Electrochemical Society*, **144** (1), 205-213 (1997).

62. K. Amine, H. Tukamoto, H. Yasuda, and Y. Fujita, *Journal of Power Sources*, **68** (2), 604-608 (1997).

63. J. Alvarado, M. A. Schroeder, M. H. Zhang, O. Borodin, E. Gobrogge, M. Olguin, M. S. Ding, M. Gobet, S. Greenbaum, Y. S. Meng, and K. Xu, *Mater Today*, **21** (4), 341-353 (2018).

64. H. Kim, F. X. Wu, J. T. Lee, N. Nitta, H. T. Lin, M. Oschatz, W. I. Cho, S. Kaskel, O. Borodin, and G. Yushin, *Adv Energy Mater*, **5** (6), (2015).

65. J. H. Wang, Y. Yamada, K. Sodeyama, C. H. Chiang, Y. Tateyama, and A. Yamada, *Nature Communications*, **7** (2016).

66. T. Noguchi, I. Yamazaki, T. Numata, and M. Shirakata, *Journal of Power Sources*, **174** (2), 359-365 (2007).

67. B. Huang, X. H. Li, Z. X. Wang, H. J. Guo, X. H. Xiong, and J. X. Wang, *J Alloy Compd*, **583** 313-319 (2014).

68. X. W. Gao, Y. F. Deng, D. Wexler, G. H. Chen, S. L. Chou, H. K. Liu, Z. C. Shi, and J. Z. Wang, *J Mater Chem A*, **3** (1), 404-411 (2015).

69. H. Xia, Y. S. Meng, L. Lu, and G. Ceder, *Journal of the Electrochemical Society*, **154** (8), A737-A743 (2007).

70. H. Xia, S. B. Tang, L. Lu, Y. S. Meng, and G. Ceder, *Electrochim Acta*, **52** (8), 2822-2828 (2007).

71. L. Baggetto, R. R. Unocic, N. J. Dudney, and G. M. Veith, *Journal of Power Sources*, **211** 108-118 (2012).

72. J. C. Li, C. Ma, M. F. Chi, C. D. Liang, and N. J. Dudney, *Adv Energy Mater*, **5** (4), (2015).

73. K. Hoshina, K. Yoshima, M. Kotobuki, and K. Kanamura, *Solid State Ionics*, **209** 30-35 (2012).

74. C. K. Chan, H. L. Peng, G. Liu, K. McIlwrath, X. F. Zhang, R. A. Huggins, and Y. Cui, *Nature nanotechnology*, **3** (1), 31-35 (2008).

75. W. Xu, S. S. S. Vegunta, and J. C. Flake, *Ecs Transactions*, **33** (23), 55-61 (2011).

76. Y. C. Yen, S. C. Chao, H. C. Wu, and N. L. Wu, *Journal of the Electrochemical Society*, **156** (2), A95-A102 (2009).

77. I. Kovalenko, B. Zdyrko, A. Magasinski, B. Hertzberg, Z. Milicev, R. Burtovyy, I. Luzinov, and G. Yushin, *Science*, **334** (6052), 75-79 (2011).

78. A. Magasinski, P. Dixon, B. Hertzberg, A. Kvit, J. Ayala, and G. Yushin, *Nat Mater*, **9** (4), 353-358 (2010).

79. W. J. Zhang, *Journal of Power Sources*, **196** (3), 877-885 (2011).

80. R. A. Huggins and W. D. Nix, *Ionics*, **6** (1-2), 57-63 (2000).

81. M. H. Park, M. G. Kim, J. Joo, K. Kim, J. Kim, S. Ahn, Y. Cui, and J. Cho, *Nano Lett*, **9** (11), 3844-3847 (2009).

82. B. Hertzberg, A. Alexeev, and G. Yushin, *J Am Chem Soc*, **132** (25), 8548-+ (2010).

83. H. Wu, G. Chan, J. W. Choi, I. Ryu, Y. Yao, M. T. McDowell, S. W. Lee, A. Jackson, Y. Yang, L. B. Hu, and Y. Cui, *Nature nanotechnology*, **7** (5), 309-314 (2012).

84. T. Takamura, S. Ohara, M. Uehara, J. Suzuki, and K. Sekine, *Journal of Power Sources*, **129** (1), 96-100 (2004).

85. J. C. Li, A. K. Dozier, Y. C. Li, F. Q. Yang, and Y. T. Cheng, *Journal of the Electrochemical Society*, **158** (6), A689-A694 (2011).

86. H. Xia, S. B. Tang, and L. Lu, *Mater Res Bull*, **42** (7), 1301-1309 (2007).

87. M. S. Park, G. X. Wang, H. K. Liu, and S. X. Dou, *Electrochim Acta*, **51** (25), 5246-5249 (2006).

88. S. L. Zhao, Z. W. Fu, and Q. Z. Qin, *Thin Solid Films*, **415** (1-2), 108-113 (2002).

89. A. C. Kozen, A. J. Pearse, C. F. Lin, M. Noked, and G. W. Rubloff, *Chem Mater*, **27** (15), 5324-5331 (2015).

90. Y. Hamon, A. Douard, F. Sabary, C. Marcel, P. Vinatier, B. Pecquenard, and A. Levasseur, *Solid State Ionics,* **177** (3-4), 257-261 (2006).

91. X. H. Yu, J. B. Bates, G. E. Jellison, and F. X. Hart, *Journal of the Electrochemical Society,* **144** (2), 524-532 (1997).

92. N. Dudney, *Interface,* **17** (3), 44-48 (2008).

93. N. J. Dudney, *Mat Sci Eng B-Solid,* **116** (3), 245-249 (2005).

94. Y. Iriyama, T. Kako, C. Yada, T. Abe, and Z. Ogumi, *Solid State Ionics,* **176** (31-34), 2371-2376 (2005).

95. Y. Amiki, F. Sagane, K. Yamamoto, T. Hirayama, M. Sudoh, M. Motoyama, and Y. Iriyama, *Journal of Power Sources,* **241** 583-588 (2013).

96. Y. Iriyama, T. Kako, C. Yada, T. Abe, and Z. Ogumi, *Journal of Power Sources,* **146** (1-2), 745-748 (2005).

97. T. Kato, T. Hamanaka, K. Yamamoto, T. Hirayama, F. Sagane, M. Motoyama, and Y. Iriyama, *Journal of Power Sources,* **260** 292-298 (2014).

98. J. Maier, *Prog Solid State Ch,* **23** (3), 171-263 (1995).

99. N. Sata, K. Eberman, K. Eberl, and J. Maier, *Nature,* **408** (6815), 946-949 (2000).

100. J. Haruyama, K. Sodeyama, L. Y. Han, K. Takada, and Y. Tateyama, *Chemistry of Materials,* **26** (14), 4248-4255 (2014).

101. F. S. Gittleson and F. El Gabaly, *Nano Lett,* **17** (11), 6974-6982 (2017).

102. Y. Z. Zhu, X. F. He, and Y. F. Mo, *J Mater Chem A,* **4** (9), 3253-3266 (2016).

103. Z. Y. Wang, J. Z. Lee, H. L. L. Xin, L. L. Han, N. Grillon, D. Guy-Bouyssou, E. Bouyssou, M. Proust, and Y. S. Meng, *Journal of Power Sources,* **324** 342-348 (2016).

104. N. C. Lindquist, P. Nagpal, K. M. McPeak, D. J. Norris, and S. H. Oh, *Rep Prog Phys,* **75** (3), (2012).

105. L. A. Giannuzzi and F. A. Stevie, *Introduction to Focused Ion Beams Instrumentation, Theory, Techniques and Practice* p. 357, Springer (2005).

106. C. A. Volkert and A. M. Minor, *Mrs Bull,* **32** (5), 389-395 (2007).

107. D. N. Qian, C. Ma, K. L. More, Y. S. Meng, and M. F. Chi, *Npg Asia Mater,* **7** (2015).

108. Y. P. Peng, P. D. Nellist, and S. J. Pennycook, *J Electron Microsc,* **53** (3), 257-266 (2004).

109. S. D. Findlay, N. R. Lugg, N. Shibata, L. J. Allen, and Y. Ikuhara, *Ultramicroscopy,* **111** (8), 1144-1154 (2011).

110. R. F. Egerton, *Rep Prog Phys*, **72** (1), (2009).

111. A. C. Luntz, J. Voss, and K. Reuter, *J Phys Chem Lett*, **6** (22), 4599-4604 (2015).

112. V. P. Phan, B. Pecquenard, and F. Le Cras, *Adv Funct Mater*, **22** (12), 2580-2584 (2012).

113. J. Li, C. Ma, M. Chi, C. Liang, and N. J. Dudney, *Adv Energy Mater*, 1401408 (2014).

114. F. Xu, N. J. Dudney, G. M. Veith, Y. Kim, C. Erdonmez, W. Lai, and Y. M. Chiang, *J Mater Res*, **25** (8), 1507-1515 (2010).

115. C. Cao, Z.-B. Li, X.-L. Wang, X.-B. Zhao, and W.-Q. Han, *Frontiers in Energy Research*, **2** (2014).

116. O. Bohnke, *Solid State Ionics*, **179** (1-6), 9-15 (2008).

117. Z. F. Zheng, H. Z. Fang, Z. K. Liu, and Y. Wang, *Journal of the Electrochemical Society*, **162** (1), A244-A248 (2015).

118. A. G. Belous, G. N. Novitskaya, S. V. Polyanetskaya, and Y. I. Gornikov, *Inorg Mater+*, **23** (3), 412-415 (1987).

119. Y. Inaguma, L. Q. Chen, M. Itoh, T. Nakamura, T. Uchida, H. Ikuta, and M. Wakihara, *Solid State Commun*, **86** (10), 689-693 (1993).

120. X. Gao, C. A. J. Fisher, T. Kimura, Y. H. Ikuhara, H. Moriwake, A. Kuwabara, H. Oki, T. Tojigamori, R. Huang, and Y. Ikuhara, *Chemistry of Materials*, **25** (9), 1607-1614 (2013).

121. S. Stramare, V. Thangadurai, and W. Weppner, *Chemistry of Materials*, **15** (21), 3974-3990 (2003).

122. K. Y. Yang, I. C. Leu, K. Z. Fung, M. H. Hon, M. C. Hsu, Y. J. Hsiao, and M. C. Wang, *J Mater Res*, **23** (7), 1813-1825 (2007).

123. C. H. Chen and K. Amine, *Solid State Ionics*, **144** (1-2), 51-57 (2001).

124. S. Furusawa, H. Tabuchi, T. Sugiyama, S. W. Tao, and J. T. S. Irvine, *Solid State Ionics*, **176** (5-6), 553-558 (2005).

125. Z. F. Zheng, H. Z. Fang, F. Yang, Z. K. Liu, and Y. Wang, *Journal of the Electrochemical Society*, **161** (4), A473-A479 (2014).

126. Y. L. Xiong, H. Z. Tao, J. A. Zhao, H. Cheng, and X. J. Zhao, *J Alloy Compd*, **509** (5), 1910-1914 (2011).

127. C. L. Li, B. Zhang, and Z. W. Fu, *Thin Solid Films*, **515** (4), 1886-1892 (2006).

128. J. K. Ahn and S. G. Yoon, *Electrochem Solid St*, **8** (2), A75-A78 (2005).

129. J. K. Ahn and S. G. Yoon, *Electrochim Acta*, **50** (2-3), 371-374 (2004).

130. M. Morales, P. Laffez, D. Chateigner, and I. Vickridge, *Thin Solid Films,* **418** (2), 119-128 (2002).

131. T. Aaltonen, M. Alnes, O. Nilsen, L. Costelle, and H. Fjellvag, *J Mater Chem,* **20** (14), 2877-2881 (2010).

132. K. Kitaoka, H. Kozuka, T. Hashimoto, and T. Yoko, *J Mater Sci,* **32** (8), 2063-2070 (1997).

133. E. J. van den Ham, N. Peys, C. De Dobbelaere, J. D'Haen, F. Mattelaer, C. Detavernier, P. H. L. Notten, A. Hardy, and M. K. Van Bael, *J Sol-Gel Sci Techn,* **73** (3), 536-543 (2015).

134. A. Manthiram, K. Chemelewski, and E. S. Lee, *Energ Environ Sci,* **7** (4), 1339-1350 (2014).

135. A. C. Sutorik, M. D. Green, C. Cooper, J. Wolfenstine, and G. Gilde, *J Mater Sci,* **47** (19), 6992-7002 (2012).

136. H. T. K. Kamala Bharathi, S. Takeuchi, L. Meshi, H. Shen, J. Shin, I. Takeuchib and L. A. Bendersky, *RSC Advances,* **6** 9 (2016).

137. J. C. Li, N. J. Dudney, J. Nanda, and C. D. Liang, *Acs Appl Mater Inter,* **6** (13), 10083-10088 (2014).

138. D. N. Qian, B. Xu, H. M. Cho, T. Hatsukade, K. J. Carroll, and Y. S. Meng, *Chemistry of Materials,* **24** (14), 2744-2751 (2012).

139. H. Xia and L. Lu, *Phys Scripta,* **T129** 43-48 (2007).

140. J. B. Bates, N. J. Dudney, G. R. Gruzalski, R. A. Zuhr, A. Choudhury, C. F. Luck, and J. D. Robertson, *Journal of Power Sources,* **43** (1-3), 103-110 (1993).

141. F. Xu, L. Belliard, D. Fournier, E. Charron, J. Y. Duquesne, S. Martin, C. Secouard, and B. Perrin, *Thin Solid Films,* **548** 366-370 (2013).

142. E. G. Herbert, W. E. Tenhaeff, N. J. Dudney, and G. M. Pharr, *Thin Solid Films,* **520** (1), 413-418 (2011).

143. C. S. Nimisha, G. M. Rao, N. Munichandraiah, G. Natarajan, and D. C. Cameron, *Solid State Ionics,* **185** (1), 47-51 (2011).

144. F. P. McGrogan, T. Swamy, S. R. Bishop, E. Eggleton, L. Porz, X. W. Chen, Y. M. Chiang, and K. J. Van Vliet, *Adv Energy Mater,* **7** (12), (2017).

145. L. L. Baranowski, C. M. Heveran, V. L. Ferguson, and C. R. Stoldt, *Acs Appl Mater Inter,* **8** (43), 29573-29579 (2016).

146. J. B. Bates, N. J. Dudney, B. Neudecker, A. Ueda, and C. D. Evans, *Solid State Ionics,* **135** (1-4), 33-45 (2000).

147. C. Monroe and J. Newman, *Journal of the Electrochemical Society*, **152** (2), A396-A404 (2005).

148. J. M. Tarascon and M. Armand, *Nature*, **414** (6861), 359-367 (2001).

149. L. G. Lu, X. B. Han, J. Q. Li, J. F. Hua, and M. G. Ouyang, *Journal of Power Sources*, **226** 272-288 (2013).

150. H. Lee, M. Yanilmaz, O. Toprakci, K. Fu, and X. W. Zhang, *Energ Environ Sci*, **7** (12), 3857-3886 (2014).

151. M. Agostini, S. Brutti, M. A. Navarra, S. Panero, P. Reale, A. Matic, and B. Scrosati, *Sci Rep-Uk*, **7** (2017).

152. J. F. M. Oudenhoven, L. Baggetto, and P. H. L. Notten, *Adv Energy Mater*, **1** (1), 10-33 (2011).

153. P. H. L. Notten, F. Roozeboom, R. A. H. Niessen, and L. Baggetto, *Adv Mater*, **19** (24), 4564-4567 (2007).

154. M. Hu, X. L. Pang, and Z. Zhou, *Journal of Power Sources*, **237** 229-242 (2013).

155. A. Manthiram, X. W. Yu, and S. F. Wang, *Nat Rev Mater*, **2** (4), (2017).

156. G. Bucci, T. Swamy, S. Bishop, B. W. Sheldon, Y. M. Chiang, and W. C. Carter, *Journal of the Electrochemical Society*, **164** (4), A645-A654 (2017).

157. G. Bucci, T. Swamy, Y. M. Chiang, and W. C. Carter, *J Mater Chem A*, **5** (36), 19422-19430 (2017).

158. Y. H. Cho, J. Wolfenstine, E. Rangasamy, H. Kim, H. Choe, and J. Sakamoto, *J Mater Sci*, **47** (16), 5970-5977 (2012).

159. J. Wolfenstine, H. Jo, Y. H. Cho, I. N. David, P. Askeland, E. D. Case, H. Kim, H. Choe, and J. Sakamoto, *Mater Lett*, **96** 117-120 (2013).

160. L. Porz, T. Swamy, B. W. Sheldon, D. Rettenwander, T. Fromling, H. L. Thaman, S. Berendts, R. Uecker, W. C. Carter, and Y. M. Chiang, *Adv Energy Mater*, **7** (20), (2017).

161. A. Al-Obeidi, D. Kramer, S. T. Boles, R. Monig, and C. V. Thompson, *Appl Phys Lett*, **109** (7), (2016).

162. A. Al-Obeidi, D. Kramer, R. Monig, and C. V. Thompson, *Journal of Power Sources*, **306** 817-825 (2016).

163. N. Tachikawa, R. Furuya, K. Yoshii, M. Watanabe, and Y. Katayama, *Electrochemistry*, **83** (10), 846-848 (2015).

164. R. P. Schultz, 2002.

165. M. A. C. Solano, M. Dussauze, P. Vinatier, L. Croguennec, E. I. Kamitsos, R. Hausbrand, and W. Jaegermann, *Ionics,* **22** (4), 471-481 (2016).

166. B. Kim, Y. S. Cho, J. G. Lee, K. H. Joo, K. O. Jung, J. Oh, B. Park, H. J. Sohn, T. Kang, J. Cho, Y. S. Park, and J. Y. Oh, *Journal of Power Sources,* **109** (1), 214-219 (2002).

167. J. Song, X. Yang, S. S. Zeng, M. Z. Cai, L. T. Zhang, Q. F. Dong, M. S. Zheng, S. T. Wu, and Q. H. Wu, *J Micromech Microeng,* **19** (4), (2009).

168. W. Y. Liu, Z. W. Fu, and Q. Z. Qin, *Thin Solid Films,* **515** (7-8), 4045-4048 (2007).

169. P. Birke and W. Weppner, *Ionics,* **2** (1), 75-79 (1996).

170. G. Constantinides, Z. I. Kalcioglu, M. McFarland, J. F. Smith, and K. J. Van Vliet, *J Biomech,* **41** (15), 3285-3289 (2008).

171. B. Qing and K. J. Van Vliet, *Mol Syst Des Eng,* **1** (3), 290-300 (2016).

172. M. de Jong, W. Chen, T. Angsten, A. Jain, R. Notestine, A. Gamst, M. Sluiter, C. K. Ande, S. van der Zwaag, J. J. Plata, C. Toher, S. Curtarolo, G. Ceder, K. A. Persson, and M. Asta, *Sci Data,* **2** (2015).

173. W. C. Oliver and G. M. Pharr, *J Mater Res,* **7** (6), 1564-1583 (1992).

174. W. C. Oliver and G. M. Pharr, *J Mater Res,* **19** (1), 3-20 (2004).

175. A. C. Fischer-Cripps, *Nanoindentation,* Springer, New York (2004).

176. L. A. Berla, S. W. Lee, Y. Cui, and W. D. Nix, *Journal of Power Sources,* **273** 41-51 (2015).

177. J. B. Ratchford, B. A. Crawford, J. Wolfenstine, J. L. Allen, and C. A. Lundgren, *Journal of Power Sources,* **211** 1-3 (2012).

178. C. S. Nimisha, K. Y. Rao, G. Venkatesh, G. M. Rao, and N. Munichandraiah, *Thin Solid Films,* **519** (10), 3401-3406 (2011).

179. A. Sharafi, S. H. Yu, M. Naguib, M. Lee, C. Ma, H. M. Meyer, J. Nanda, M. F. Chi, D. J. Siegel, and J. Sakamoto, *J Mater Chem A,* **5** (26), 13475-13487 (2017).

180. F. Lin, I. M. Markus, M. M. Doeff, and H. L. L. Xin, *Sci Rep-Uk,* **4** (2014).

181. Z. L. Wang, J. S. Yin, and Y. D. Jiang, *Micron,* **31** (5), 571-580 (2000).

182. N. Jiang and J. C. H. Spence, *Ultramicroscopy,* **111** (7), 860-864 (2011).

183. G. Larraz, A. Orera, and M. L. Sanjuan, *J Mater Chem A,* **1** (37), 11419-11428 (2013).

184. A. J. Pearse, T. E. Schmitt, E. J. Fuller, F. El-Gabaly, C. F. Lin, K. Gerasopoulos, A. C. Kozen, A. A. Talin, G. Rubloff, and K. E. Gregorczyk, *Chemistry of Materials,* **29** (8), 3740-3753 (2017).

185. B. Fleutot, B. Pecquenard, H. Martinez, and A. Levasseur, *Solid State Ionics,* **206** 72-77 (2012).

186. A. C. Kozen, A. J. Pearse, C. F. Lin, M. A. Schroeder, M. Noked, S. B. Lee, and G. W. Rubloff, *J Phys Chem C,* **118** (48), 27749-27753 (2014).

187. J. P. Contour, A. Salesse, M. Froment, M. Garreau, J. Thevenin, and D. Warin, *J Microsc Spect Elec,* **4** (4), 483-491 (1979).

188. Rosolovs.Vy, V. I. Nefedov, and Sinelnik.Sm, *B Acad Sci Ussr Ch+,* (7), 1445-1448 (1973).

189. A. Galtayries, E. Laksono, J. M. Siffre, C. Argile, and P. Marcus, *Surf Interface Anal,* **30** (1), 140-144 (2000).

190. S. Yu, R. D. Schmidt, R. Garcia-Mendez, E. Herbert, N. J. Dudney, J. B. Wolfenstine, J. Sakamoto, and D. J. Siegel, *Chemistry of Materials,* **28** (1), 197-206 (2016).

191. A. Sakuda, A. Hayashi, Y. Takigawa, K. Higashi, and M. Tatsumisago, *J Ceram Soc Jpn,* **121** (1419), 946-949 (2013).

192. M. Ohashi, S. Kanzaki, and H. Tabata, *J Am Ceram Soc,* **74** (1), 109-114 (1991).

193. T. Kasuga, Y. Ota, K. Tsuji, and Y. Abe, *J Am Ceram Soc,* **79** (7), 1821-1824 (1996).

194. M. P. Brassington, A. J. Miller, J. Pelzl, and G. A. Saunders, *J Non-Cryst Solids,* **44** (1), 157-169 (1981).

195. T. Y. Wei, Y. Hu, and L. G. Hwa, *J Non-Cryst Solids,* **288** (1-3), 140-147 (2001).

196. T. Rouxel, *J Am Ceram Soc,* **90** (10), 3019-3039 (2007).

197. J. Mayer, L. A. Giannuzzi, T. Kamino, and J. Michael, *Mrs Bull,* **32** (5), 400-407 (2007).

198. J. G. Pellerin, D. P. Griffis, and P. E. Russell, *J Vac Sci Technol B,* **8** (6), 1945-1950 (1990).

199. S. Rubanov and P. R. Munroe, *J Mater Sci Lett,* **20** (13), 1181-1183 (2001).

200. A. Lugstein, B. Basnar, and E. Bertagnolli, *J Vac Sci Technol B,* **20** (6), 2238-2242 (2002).

201. N. I. Kato, *J Electron Microsc,* **53** (5), 451-458 (2004).

202. S. Bals, W. Tirry, R. Geurts, Z. Q. Yang, and D. Schryvers, *Microsc Microanal,* **13** (2), 80-86 (2007).

203. N. Miyajima, C. Holzapfel, Y. Asahara, L. Dubrovinsky, D. J. Frost, D. C. Rubie, M. Drechsler, K. Niwa, M. Ichihara, and T. Yagi, *J Microsc-Oxford,* **238** (3), 200-209 (2010).

204. M. Schaffer, B. Schaffer, and Q. Ramasse, *Ultramicroscopy,* **114** 62-71 (2012).

205. A. Brazier, L. Dupont, L. Dantras-Laffont, N. Kuwata, J. Kawamura, and J. M. Tarascon, *Chemistry of Materials*, **20** (6), 2352-2359 (2008).

206. K. Yamamoto, Y. Iriyama, T. Asaka, T. Hirayama, H. Fujita, C. A. J. Fisher, K. Nonaka, Y. Sugita, and Z. Ogumi, *Angew Chem Int Edit*, **49** (26), 4414-4417 (2010).

207. D. Santhanagopalan, D. Qian, T. McGilvray, Z. Y. Wang, F. Wang, F. Camino, J. Graetz, N. Dudney, and Y. S. Meng, *J Phys Chem Lett*, **5** (2), 298-303 (2014).

208. Z. Y. Wang, D. Santhanagopalan, W. Zhang, F. Wang, H. L. L. Xin, K. He, J. C. Li, N. Dudney, and Y. S. Meng, *Nano Lett*, **16** (6), 3760-3767 (2016).

209. Y. I. Jang, N. J. Dudney, D. A. Blom, and L. F. Allard, *Journal of the Electrochemical Society*, **149** (11), A1442-A1447 (2002).

210. B. J. Neudecker, R. A. Zuhr, and J. B. Bates, *Journal of Power Sources*, **81** 27-32 (1999).

211. J. F. Ziegler, *Nucl Instrum Meth B*, **219** 1027-1036 (2004).

212. D. C. Lin, Y. Y. Liu, and Y. Cui, *Nature nanotechnology*, **12** (3), 194-206 (2017).

213. K. Murata and M. Wolf, *Bba-Gen Subjects*, **1862** (2), 324-334 (2018).

214. X. F. Wang, M. H. Zhang, J. Alvarado, S. Wang, M. Sina, B. Y. Lu, J. Bouwer, W. Xu, J. Xiao, J. G. Zhang, J. Liu, and Y. S. Meng, *Nano Lett*, **17** (12), 7606-7612 (2017).

215. Y. Z. Li, Y. B. Li, A. L. Pei, K. Yan, Y. M. Sun, C. L. Wu, L. M. Joubert, R. Chin, A. L. Koh, Y. Yu, J. Perrino, B. Butz, S. Chu, and Y. Cui, *Science*, **358** (6362), 506-510 (2017).

216. J. F. Ziegler, M. D. Ziegler, and J. P. Biersack, *Nucl Instrum Meth B*, **268** (11-12), 1818-1823 (2010).

217. T. Ishitani and H. Kaga, *J Electron Microsc*, **44** (5), 331-336 (1995).

218. A. Rigort and J. M. Plitzko, *Arch Biochem Biophys*, **581** 122-130 (2015).

219. J. Alvarado, M. Schroeder, T. O. Pollard, X. Wang, J. Z. Lee, M. Zhang, T. A. Wynn, M. Ding, O. Borodin, Y. S. Meng, and K. Xu, (in preparation).

220. P. Albertus, S. Babinec, S. Litzelman, and A. Newman, *Nature Energy*, **3** (1), 16-21 (2018).

221. Y. Zhang, J. Qian, W. Xu, S. M. Russell, X. Chen, E. Nasybulin, P. Bhattacharya, M. H. Engelhard, D. Mei, R. Cao, F. Ding, A. V. Cresce, K. Xu, and J. G. Zhang, *Nano Lett*, **14** (12), 6889-6896 (2014).

222. F. Ding, W. Xu, X. Chen, J. Zhang, M. H. Engelhard, Y. Zhang, B. R. Johnson, J. V. Crum, T. A. Blake, X. Liu, and J. G. Zhang, *Journal of the Electrochemical Society*, **160** (10), A1894-A1901 (2013).

223. M. J. Zachman, E. Asenath-Smith, L. A. Estroff, and L. F. Kourkoutis, *Microsc Microanal*, **22** (6), 1338-1349 (2016).

224. N. Dudney, W. C. West, and J. Nanda, *Handbook of Solid State Batteries*, World Scientific, Singapore (2016).

225. D. B. Williams and C. B. Carter, *Transmission Electron Microscopy: A Textbook for Materials Science*, Springer, New York (2009).

226. M. L. Taheri, E. A. Stach, I. Arslan, P. A. Crozier, B. C. Kabius, T. LaGrange, A. M. Minor, S. Takeda, M. Tanase, J. B. Wagner, and R. Sharma, *Ultramicroscopy*, **170** 86-95 (2016).

227. T. Radetic, A. Gautam, C. Ophus, and C. Czarnik, *Microsc Microanal*, **20** (S3), 1594 (2014).

228. A. C. Milazzo, A. C. Cheng, A. Moeller, D. Lyumkis, E. Jacovetty, J. Polukas, M. H. Ellisman, N. H. Xuong, B. Carragher, and C. S. Potter, *J Struct Biol*, **176** (3), 404-408 (2011).

229. Y. Gong, J. N. Zhang, L. W. Jiang, J. A. Shi, Q. H. Zhang, Z. Z. Yang, D. L. Zou, J. Y. Wang, X. Q. Yu, R. J. Xiao, Y. S. Hu, L. Gu, H. Li, and L. Q. Chen, *J Am Chem Soc*, **139** (12), 4274-4277 (2017).